# ADVANCES IN MATERIALS STRATEGIES, CIRCUIT DESIGNS, AND INFORMATICS FOR WEARABLE, FLEXIBLE AND STRETCHABLE ELECTRONICS WITH MEDICAL AND ROBOTIC APPLICATIONS

BY

YU HAO LIU

DISSERTATION

Submitted in partial fulfillment of the requirements
for the degree of Doctor of Philosophy in Materials Science and Engineering
in the Graduate College of the
University of Illinois at Urbana-Champaign, 2016

Urbana, Illinois

Doctoral Committee:

Professor John A. Rogers, Chair, Director of Research
Professor Naresh R. Shanbhag
Professor Paul V. Braun
Assistant Professor Kristopher Kilian

## ABSTRACT

The future of medical electronics should be flexible, stretchable and skin-integrated. While modern electronics become increasing smaller, faster and energy efficient, the designs remain bulky and rigid due to materials and processing limitations. The miniaturization of health monitoring devices in wearable form resembles a significant progress towards the next-generation medical electronics. However, there are still key challenges in these wearable electronics associated with medical-grade sensing precision, reliable wireless powering, and materials strategy for skin-integration.

Here, I present a series of systematic studies from materials strategies, circuit design to signal processing on skin-mounted electronic wearable devices. Several types of Epidermal Electronic Systems (EES) develop applications in dermatology, cardiology, rehabilitation, and wireless powering. For skin hydration measurement, fundamental studies of electrode configurations and skin-electrode impedance reveal the optimal sensor design. Furthermore, wireless operation of hydration sensor was made possible with direct integration on skin, and on porous substrates that collect and analyze sweats.

Additionally, I present an epidermal multi-functional sensing platform that could provide a control-feedback loop through electromyogram and current stimulation; and a mechano-acoustic device that could capture vibrations from muscle, heart, and throat as diagnostic tools or human-machine interface. I developed a modularized epidermal radio-frequency energy transfer epidermal device to eliminate batteries and power cables for wearable electronics.

Finally, I present a clinical study that validates a commercialized ESS on patients with nerve disorders for electromyography monitoring during peripheral nerve and spinal cord surgeries.

## ACKNOWLEDGEMENTS

First of all, I would like to give my deepest appreciation to my advisor, Professor John Rogers, who has motivated, supported and guided me through my five years of doctoral study at University of Illinois, Urbana-Champaign. He continues to inspire me with his ingenious research insights, tireless dedication to work, and superior leadership of the group. The guidance and resources John provided me are invaluable and has changed the way I approach scientific and engineering problems.

In addition, I would like to express my sincere gratitude to several mentors, Professor Xian Huang, Professor Jae-Woong Jeong, and Professor Baoxing Xu, who have guided me on a daily basis, and provided a valuable learning experience for me. I am very thankful for their mentorship and supports. I would also like to thank my committee members, Professor Paul Braun, Professor Naresh Shanbhag, Professor Kristopher Kilian, and Professor Jian-Min Zuo, for their insightful comments and constructive criticism.

I am very lucky to have interacted with a diverse team of talents in my research group. I would like specifically to thank Yan Zheng, Lizhi Xu, Lan Yin, KyungIn Jang, Xu Xie, Xing Sheng, Giovanni Salvatore, Jeonghyun Kim, Jungwoo Lee, Sheng Xu, Matt Pharr, Jonathan Fan, and Limei Tian for their research collaboration and friendship. I am also very thankful to those undergraduate researchers who have helped me along my five years of study; they are Gil Woo Kong, Sang Heon Lee, Hyunjin Kim, Lingqing Yan, Hank Liu, Max Lai, Daizhen Li, and Chuxuan Wang. Gil, Lingqing, Hank, and Max have contributed significantly to the published projects.

Furthermore, I would like to thank all my collaborators that worked with me in the clinical experiment, specifically Dr. Aadeel Akhtar, Dr. Marvin Slepian, Dr. Michel Kliot, Dr.

Douglas Zhang, Kaitlyn Ammann, and Dr. Phat Tran. I would also like to thank Professor Yonggang Huang, Professor Jianliang Xiao, and their groups for providing mechanical simulation supports in all studies.

Besides the great researchers I worked with, I am grateful to have worked in the Materials Research Laboratory, Micro-and-Nano Technology Laboratory, and Beckman Institute at the University of Illinois, Urbana-Champaign. I would like to thank all the staffs in these facilities for their technical training on the research instruments. I would also like to thank SONIC (Systems on Nanoscale Information Fabrics) Center, National Science Foundation, and Materials Science and Engineering Department for funding my graduate study.

Moreover, I would like to express my sincere appreciation to my family and especially my parents, Woody Liu and Joyce Chen, as well as my aunt, Caroline Renken, for their continued support and encouragement.

Lastly, I would like to thank my fiancée, Iris Zhang, who was always there to support, encourage and comfort me in the last five years. Her patience and support are my biggest motivation in the toughest moments. I was very fortunate to have her with me along my doctoral study.

I am proud and grateful to complete my doctoral study in such an outstanding research group, with this many great people.

# TABLE OF CONTENTS

# CHAPTER 1

# INTRODUCTION

The doctoral research presented here is to develop methodologies for sensors building on the concept of wearable, flexible, and stretchable electronics with functionalities suitable for advanced medical and robotic applications. The approach is to utilize advanced microfabrication and transfer-printing techniques with selective metallic, polymeric, and semiconducting materials engineered for the targeted purposes. The scope of this work ranges from fundamental studies of underlying mechanisms for skin-electrode interfacial physics to application-specific sensors design and clinical studies for device validation. Each sensors presented here involve design at the system, circuit and materials level; fabrication using microelectronics cleanroom facilities; and a combination of the bench, animal, or clinical tests. Developing application-specific sensors with competing properties to the industry's golden standards are key challenges in the field. This introduction will examine the foundation of skin-mounted electronics, and discuss opportunities and approaches to develop application-specific sensors on human skin.

## 1.1 Development of Next-generation Medical Electronics

Since the beginning of Moore's law in 1975, modern electronics benefits from the doubling of transistors number in integrated circuits to develop faster, smaller, and more energy-efficient devices. Along with the miniaturization trend in consumer electronics, medical devices with advanced functionalities have become portable, or even wearable in the last decade. The first thermometer developed to measure the body temperature of a human being dates back to AC 1625, and digital thermometer not until late 1970s[1]. Since then, the infra-red thermometer and the temporal artery thermometer were invented with smaller form-factor, higher sensing

precision, and faster reading time. The natural follow-up question for doctors, scientists, and engineers is – how should we design the next generation thermometer?

Antoni Gaudi, a Spanish architect in the beginning of 20th century, believes that there are no straight lines in nature, and therefore buildings should be made out of curved lines. The same concept applies to electronics, especially medical devices that require flexible and stretchable mechanics to interface with the human body. In particular, bio-integrated electronics (the technology of integrating electronic devices on biological tissues) that exploits new materials synthesis, design, and application create new opportunities for the next-generation of electronics[2]. Potential studies can range from the electronic skin to artificial organ and cellular level robotics. In practice, non-invasive technology that involves the development of wearable electronics interfacing with skin is the most promising approach. The research presented here base on such technology platform which enables thin, stretchable "tissue like" inorganic electronic devices could be the pioneer for the next-generation electronics[3].

### 1.2 Epidermal Electronic System (EES)

Biology is curvilinear, soft, and elastic; but conventional semiconductors and silicon wafer are not. Semiconductors are mostly rigid, flat, and brittle, and they make all existing high-performing electronics in one form or another. There is a gap of mechanical mismatch between Biology and current existing electronics, hinging the development of wearable technologies that provides intimate, conformal contact with human body. Earlier forms of wearable electronics exist in the shape of bulky circuit enclosures strapped on the body[4], or antenna cables sewed in the fabrics[5], mostly for radio and entertainment applications. The awareness of health and wellness foster the development of personal monitoring electronics that could measure

physiological status and exercise routines. However, despite the advance in miniaturized design and software, the hardware design remains conceptually old, which uses straps and adhesive tapes to mount the electronics on skin. The same situation applies to physiological measurement and stimulation techniques, which have been the dominant method to capture vital signals from skin non-invasively since 1929 with measuring electroencephalography from the scalp[3]. The interface between medical electrodes and electronics and human skin mainly involves adhesives, clamps, straps, needles with conductive gels and rigid system components. The existing physiological measurement systems provide robust and reliable functionalities for clinical applications[6, 7], but the extended wiring, bulky design, and poor skin integration creates limitations for mobility, comfort, and robust skin contact required for long-term precision monitoring.

A research group led by Professor John Rogers at the University of Illinois introduced a different approach[3] in 2010. Inspired by the idea of a temporary tattoo, the researchers create a "skin-like", "tissue-like" electronics tattoo that sits on an ultrathin membrane which conformally laminates onto the skin surface by soft contact and van der Waal's force. The mechanically invisible electronic tattoo, the epidermal electronic system (EES), could be a combination of electrodes, sensors, power supply, and communication components. It is as thin and light as a human hair. It is flexible and stretchable. It is wearable and bio-integrated. It opens a full spectrum of possibilities in integrating electronics with biology.

In the following sections, we will discuss the development of this technology from the perspective of materials, mechanics, fabrication, and integration strategies.

### 1.3 Materials of EES

All high-performing electronics exploit single crystal inorganic semiconductors (i.e. Si,

GaAs) that are fundamentally rigid and fragile in a wafer form. Organs and skin of the human body are, in contrast, soft and wavy. This mismatch in mechanical properties challenges the development of electronics technologies that are capable of intimate, conformal integration, for applications ranging from healthcare monitoring and diagnostics via physiological signals, therapeutic drug deliveries, human machine interface and others[8]. Organic electronic materials are a potential solution as alternatives to inorganics in materials selection. The intrinsic flexible properties of organics can facilitate skin integration, but they are not stretchable or capable of wrapping surfaces with arbitrary complex shapes. Also, known organic semiconductors until today have low electron mobilities, uncertain operating reliability and limited ability for commercial integration into inorganic-based integrated circuits[2]. Although many state-of-the-art one-dimensional and two-dimensional inorganic materials show promising electrical and mechanical properties[9], they remain in early stage development, with few examples of practical devices, even at the level of application demonstration. Doped single crystalline silicon nanomembrane is the most common active materials in EES for building high-performance transistors and diodes[10, 11, 12, 13, 14]. Gold is suitable for electrodes that interfacing the skin due to its inert chemical properties and low contact impedance[3, 15]. Copper is the best for interconnects and antenna due to its low electrical resistivity[16].

EES exploits design strategies with novel fabrication techniques on conventional high-performing semiconductor and metallic materials to build thin, stretchable, skin-mounted electronics devices for practical, clinical purposes. Figure 1.1 shows established strategies includes the integration of nanostructures (e.g. membranes, ribbons) of single crystalline semiconductor materials[14], serpentine-shaped metal mesh structures[17], and encapsulating electronic devices on the neutral mechanical plane between low modulus polymers[18]. Other

strategies, including the use of extremely thin polyester substrate[19], high ultimate fractural strength[20], connected rigid islands[21], pre-strained elastomers[22], and tailing techniques[23], were developed to build flexible and stretchable devices.

### 1.4 Mechanics of EES

The elastic modulus and thickness of a material determine its flexibility. As the modulus decreases, the resistance of an object to a non-permanent elastic deformation decreases, making it is easier to bend and stretch under the same applied force. As an electronic tattoo, EES requires materials that provide mechanics necessary to wrap complex shapes in biology, typically with the ability to bend to small (<1 mm) radii of the curvature[8]. Since the functional materials (i.e. semiconductors and metals) usually bond to thin polymer substrates for skin integration, this requires the substrate layer to have small (<1 MPa) or similar (~ 130 kPa) elastic modulus to skin[24]. Figure 1.1 summarized the elastic moduli of common and potential materials to be used in EES with reference to the skin tissue value. Details on the mechanics concepts that guided practical EES design via finite element analysis and simulation techniques can be found in the work by Wang *et. al.*[24]. The stretchability of EES mostly depends on the geometrical design of device layout[17], the fracture strain of used materials[17], and the effective strain transferred from the carrying substrate. The adhesion between the EES and the skin is determined by the bending stiffness, thickness of the materials, and the area of contact of EES[24].

### 1.5 Fabrications of EES

The fabrication of EES happens in the cleanroom facility, in which the particle level in the atmosphere is low to ensure yield and performance of micro size electronic components. There are two types of EES from the perspective of making it, one with active components (e.g.

semiconductor devices), and one with only passive materials (e.g. metals, polymers). Figure 1.2 illustrate the process for fabricating the former EES devices, while passive EES starts with a different substrate material and begin the process in step 5. For active EES, the fabrication starts on a wafer with desired semiconductors, and the most common one is silicon-on-insulator wafers (SOITEC, France). The buried oxide provides route to pick up and transfer only the top Si layer to a foreign substrate. Solid state diffusion doping is used to p-type and n-type doping of top silicon nanomembrane (SINM), hydrofluoric acid then removed the buried oxide, and the top silicon is transferred to receiver substrate with polyimide as supporting layer, PMMA below as sacrificial layer, and silicon wafer as a handle substrate. The transfer-printing techniques use PDMS as a stamp to temporarily pick up the weakly bonded materials through rapid retraction and printing through slow lamination. Metallic interconnect are then deposited on top using e-beam evaporator or sputtering tools. Photolithography tools are used to pattern the layouts of interconnects or electrical contacts. Wet etching or plasma dry etching tools (i.e. reactive ion etching) are used in the following step. If capacitor or encapsulation or needed, there will be additional deposition, patterning and etching steps, followed by second metallization and final encapsulation. The final device layout is then picked up by a water soluble temporary tape and integrates with flexible and stretchable substrate. For passive EES device, it begins with metal deposition on the same receiver substrate with PMMA sacrificial layer. The PMMA layer is used at the final step to detach the entire device from the handle wafer and allow water soluble tape to transfer print the device again. Skin integration occurs after dissolving the water soluble tapes away.

## 1.6 Skin-integration of EES

Three types of skin-integration strategies are feasible in EES: temporary epidermal tattoo,

hard-soft integration, and functional integration. Started with the concept of temporary tattoo, the very first EES uses silicone materials (i.e. PDMS, Ecoflex, Solaris) with similar elastic modulus as the skin for a substrate to achieve optimal conformal contact and adhesion[3]. Thin film electronics are fabricated on silicon wafers and transfer printed on the top side of thin silicone film using $SiO_2$ as a bonding agent. This electronic tattoo is then laminated directly on the skin (figure 1.3a) with the electronics side in contact with skin for electrophysiological measurement. Other materials such as polyvinyl alcohol (PVA) film[25], water soluble tape[26], medical adhesives[15], silbione[27], acrylic tape[28], and polyester[19] was used as a substrate to fulfill the requirement to specific applications. These materials have different thickness, elastic modulus, adhesion force with skin, and other physical properties. However, the complexity of fabricating high-performance thin-film electronics limits its ability to form integrity circuit for advanced digital functions, such as wireless communication, signal processing, and power transfer. The idea of hard-soft integration[16] appears to combine commercially available off-the-shelf chips and stretchable metal interconnects on a soft, flexible patch on the skin (figure 1.3b). This platform enables a new route to build integrated circuits on skin with performance comparable to commercially available devices in rigid forms. A previous study[28] also combine both first and second integration strategies to create near-field communication (NFC) tattoo, which uses epidermal tattoo for inductive coupling antenna and stretchable interconnects for mounting bare die, unpackaged NFC microcontroller chip (figure 1.3c). In addition, researchers have combined thin film electronics with various functional substrates in application-specific sensors. For example, a blood oximetry sensor on strain limiting fabric to enable long-term reusability (figure 1.3d[27]), a hydration sensor on porous sponge substrates that collect sweats (figure 1.3e[26]), or a UV sensor on silicone materials mixed with photosensitive dye and NFC platform (figure 1.3f).

Successful integration of EES is indicated by the conformal contact and long-lasting adhesion between EES and the skin. The electronic layout design and substrate thickness are the two most important engineering factors. The Previous study[15] found that EES structure with linewidth smaller the skin surface relief amplitudes (15 – 100 um) and a lateral dimension (40 – 1000 um) ensure the conformal contact (figure 1.3g). In addition, another study[29] found that the critical substrate thickness (~25 um) to provide conformal contact with excellent adhesion.

## 1.7 Lab-on-skin

There are plenty of rooms on the skin. Human skin is a diagnostic platform with vital biological signals from organs, muscle, dermis and epidermis. Soft, flexible and stretchable devices emerge as wearable interfaces between soft tissues and rigid electronics for biomedical sensing, robotic feedback and control, advanced therapies, non-invasive continuous monitoring and diagnostic tools. Here, I introduce the “Lab on Skin” term to describe a set of devices which provide diagnostic and integration capabilities on skin for healthcare applications. These sensors could range from impedance based hydration detection to resistance based temperature measurement. The underlying concept is that most of the biometrics needed for health monitoring and disease states diagnosis should be done non-invasively and comfortably on the human skin. It also provides an easy-to-use platform for telemedicine, home-care, and elder-care. Features, such as wireless communication, continuous monitoring, and wearability, are the most important factors in Lab-on-skin devices.

## 1.8 Skin Anatomy

Skin is a signal source. It can either generate or transmit a biological signal that could serve as important metrics for our body. To\ measure signals from the skin, we need first to

understand the structure of skin and their origin. Human skin has two principal structural layers, the epidermis and the dermis[30]. The epidermis is the outer layer of the skin, serving as the physical, chemical, and biological barrier to the external environment. The dermis is the deeper layer that provides structural support for the skin and physical sensations. Below the cutaneous tissues, there are mainly the hypodermis, the muscle, the major nerves and blood vessels. Figure 1.4 shows the primary signal sources on the skin and the typical physiological information that could be available from these sources.

Starting from the very bottom, major nerves such as median nerve in the upper limbs from brachial plexus (central nervous system) innervates biceps and triceps muscle to stimulate contraction. The stimulation is amplified by muscle fibers to produce a summation of the action potential that can be picked up by electrodes placing near the stimulated muscle group in terms of voltage signal. This bio-potential signal could also come from the cardiac systole-diastole cycle (Electrocardiogram, ECG), brain activity (Electroencephalogram, EEG), and eye movement (Electrooculogram, EOG)[31]. The major arteries could provide useful information such as blood temperature, heart rate, pressure, oxygen level, and pulse wave velocity non-invasively via the skin, while veins measurements are not a common practice. In the epidermis, stratum corneum serves as the direct interface between skin and measuring electronics. It consists of stacked layers of cells in the maturing process from basal cells (live, reproducible) to corneocytes (dead cells); these cells make the major water retention layer in skin[32]. Hydration measurement could be performed using impedance techniques. There is also a direct correlation between age and the elastic modulus of skin. Epidermis is also an exhaust for sweat, which serves as an analyte for pH, mineral ion, glucose, water, lactic acid, and urea concentrations. In addition, when there is a wound present, several physical and chemical metrics could be

measured on the stratum corneum near wound site. All of these signals measurable from skin could be used for either health monitoring or diagnosis.

## 1.9 Epidermis Monitoring and Diagnostics

Medical devices are designed to diagnose, monitor, prevent, and treat diseases. The skin provides an ideal platform, and vital signals measured from the skin are often used to assess the body's essential functions and physical state. Figure 1.5 shows several examples of EES developed for both monitoring and diagnostic functions. For healthcare monitoring, EES provides tools to measure the basic body functions; this includes temperature[33, 34, 35], hydration[25, 26, 36, 37], blood pressure[38], heart rate[15, 39], and sweat[26]. For diagnostic purposes, applications could range from diseases in dermatology, cardiology, neurology, and hematology to rehabilitation and urgent care. For example, electrophysiology like ECG provides detail information on the ventricles and atriums for cardiac disease[39]; EEG shows electrical activities of brain for studies of sleep apnea, epilepsy, and other neural disorders[40]; and EMG indicates nerve and muscle health[29]. EES offers either both standalone sensor[29] and multi-functional sensing platforms[41].

Beyond medical applications, EES could serve as the interface between human and computers in robotics and prosthetic controls. The seamless, wearable body tattoo can collect body signals and classify them in command states[29], or it can provide feedback in forms of electrotactile stimulation[41]. Demonstration of this technology was first shown with controlling drones using EMG signals from ESS mounted at the flexor muscle on both left and right forearms[29]. When the user performs 4 distinguished hand motions, specific EMG patterns are generated. The machine learning and classification codes could then transform the EMG signal into commands that launch, rotate, move, and land the drone. Other demonstration could be seen on robots and prosthesis[41].

## 1.10 Dissertation Overview

Wearable, flexible, and stretchable electronics is an emerging technology for consumer and medical devices. In a step further, EES provides a unique platform to improve functionality, wearing comfort, and long-term usage. Three main challenges hinder the practical integration of EES: short of diverse sensing mechanism, wireless powering and communication, and lack of clinical validation. This dissertation presents novel materials strategies, circuit design, and signal processing techniques to address these concerns and discuss the advantages and disadvantages of each approach.

Chapter 1 provides a general overview of epidermal electronic system with focus on the materials, mechanics, fabrication, and integration strategies of such system on human skin. In addition, it introduces a "Lab-on-skin" idea to summarize the practical applications of EES.

Chapter 2 introduces an impedance-based electrical technique to measure skin hydration. The development of hydration sensors begins with studies in electrode configuration, and extends to circuit design that enables wireless hydration measurement and materials design that allows sweat sensing. The chapter also describes a fundamental study that focuses on the skin-electrode interface impedance study that provides robust guidance for the design of electrode configuration and materials.

Chapter 3 describes a multi-functional sensing and stimulation platform that enable not only passively capture signal from human body, but also provides feedback in the form of electrical stimulation. Three demonstration of this platform presents in this chapter are the sensorimotor robotic control, low-back exertion management, and electrical muscle activation.

Chapter 4 presents an epidermal mechano-acoustic sensor capable of detecting small

amplitude vibrations from the surface of skin. It describes a detailed systematic study of the effect of aerial mass in vibration sensing and the unique performance of core-shell encapsulation strategies. Theoretical models and finite element analysis confirm the measurement results and the stretchability of the device. The sensor demonstrates specific applications in diagnosing heart murmurs in patients with cardiovascular diseases, analyzing acoustic signature changes in ventricular assist device, and capturing vocal vibrations as control commands for computer game.

Chapter 5 describes systematic studies on modularization and soft contact lamination approaches that lead to the first radio-frequency wireless power transfer EES. It presents unique materials, circuit, and fabrication strategies. The circuit components are individually studies and characterized, as well as the safety and effectiveness of the wireless power transfer system.

Chapter 6 presents a commercialized version of EES and a clinical study in the surgery room for monitoring surface EMG signal during peripheral and spinal nerve surgeries. A comparison between commercial EES and industry's golden technique is discussed through the stimulation current threshold.

Chapter 7 provides a general summary of the results presented in this dissertation and discuss the future direction of skin-mounted, flexible, and stretchable electronics research and development.

This dissertation completes a medical technology development cycle from invention, design, fabrication, testing to clinical validation.

## 1.11 References

1. Nokes L, Jennings D, Flint T, *et al. Introduction to medical electronics applications*. Butterworth-Heinemann (1995).

2. Kim D-H, Ghaffari R, Lu N, *et al.* Flexible and stretchable electronics for biointegrated

devices. *Annual review of biomedical engineering* **14**, 113-128 (2012).

3. Kim D-H, Lu N, Ma R, *et al.* Epidermal electronics. *science* **333**, 838-843 (2011).

4. How To Make The World's Smallest 3-Tube Radio Set. Radio-Craft. 1936. December.

5. The Radio Hat. Radio-Craft. 1949. June.

6. Khan Y, Ostfeld AE, Lochner CM, *et al.* Monitoring of Vital Signs with Flexible and Wearable Medical Devices. *Advanced Materials*, (2015).

7. Pang C, Lee C, Suh KY. Recent advances in flexible sensors for wearable and implantable devices. *Journal of Applied Polymer Science* **130**, 1429-1441 (2013).

8. Rogers J. Bio-integrated electronics. In: *Electron Devices Meeting (IEDM), 2012 IEEE International*. IEEE (2012).

9. Hammock ML, Chortos A, Tee BCK, *et al.* 25th Anniversary Article: The Evolution of Electronic Skin (E-Skin): A Brief History, Design Considerations, and Recent Progress. *Advanced Materials* **25**, 5997-6038 (2013).

10. Viventi J, Kim D-H, Moss JD, *et al.* A conformal, bio-interfaced class of silicon electronics for mapping cardiac electrophysiology. *Science translational medicine* **2**, 24ra22-24ra22 (2010).

11. Kim D-H, Lu N, Ghaffari R, *et al.* Materials for multifunctional balloon catheters with capabilities in cardiac electrophysiological mapping and ablation therapy. *Nature materials* **10**, 316-323 (2011).

12. Viventi J, Kim D-H, Vigeland L, *et al.* Flexible, foldable, actively multiplexed, high-density electrode array for mapping brain activity in vivo. *Nature neuroscience* **14**, 1599-1605 (2011).

13. Kim RH, Kim S, Song YM, *et al.* Flexible vertical light emitting diodes. *small* **8**, 3123-3128 (2012).

14. Ko HC, Shin G, Wang S, *et al.* Curvilinear electronics formed using silicon membrane circuits and elastomeric transfer elements. *small* **5**, 2703-2709 (2009).

15. Yeo WH, Kim YS, Lee J, *et al.* Multifunctional epidermal electronics printed directly onto the skin. *Advanced Materials* **25**, 2773-2778 (2013).

16. Xu S, Zhang Y, Jia L, *et al.* Soft microfluidic assemblies of sensors, circuits, and radios for the skin. *science* **344**, 70-74 (2014).

17. Fan JA, Yeo W-H, Su Y, *et al.* Fractal design concepts for stretchable electronics. *Nature*

*communications* **5**, (2014).

18. Sekitani T, Zschieschang U, Klauk H, *et al.* Flexible organic transistors and circuits with extreme bending stability. *Nature materials* **9**, 1015-1022 (2010).

19. Kaltenbrunner M, Sekitani T, Reeder J, *et al.* An ultra-lightweight design for imperceptible plastic electronics. *Nature* **499**, 458-463 (2013).

20. Kim BJ, Jang H, Lee S-K, *et al.* High-performance flexible graphene field effect transistors with ion gel gate dielectrics. *Nano letters* **10**, 3464-3466 (2010).

21. Libanori R, Erb RM, Reiser A, *et al.* Stretchable heterogeneous composites with extreme mechanical gradients. *Nature communications* **3**, 1265 (2012).

22. Münzenrieder N, Cantarella G, Vogt C, *et al.* Stretchable and Conformable Oxide Thin-Film Electronics. *Advanced Electronic Materials* **1**, (2015).

23. Fratzl P. Applied physics: The virtues of tiling. *Nature* **516**, 178-179 (2014).

24. Wang S, Li M, Wu J, *et al.* Mechanics of epidermal electronics. *Journal of Applied Mechanics* **79**, 031022 (2012).

25. Huang X, Yeo W-H, Liu Y, *et al.* Epidermal differential impedance sensor for conformal skin hydration monitoring. *Biointerphases* **7**, 52 (2012).

26. Huang X, Liu Y, Chen K, *et al.* Stretchable, wireless sensors and functional substrates for epidermal characterization of sweat. *small* **10**, 3083-3090 (2014).

27. Jang K-I, Han SY, Xu S, *et al.* Rugged and breathable forms of stretchable electronics with adherent composite substrates for transcutaneous monitoring. *Nature communications* **5**, (2014).

28. Kim J, Banks A, Cheng H, *et al.* Epidermal Electronics with Advanced Capabilities in Near-Field Communication. *small* **11**, 906-912 (2015).

29. Jeong JW, Yeo WH, Akhtar A, *et al.* Materials and Optimized Designs for Human-Machine Interfaces Via Epidermal Electronics. *Advanced Materials* **25**, 6839-6846 (2013).

30. Marino C. *Skin physiology, irritants, dry skin and moisturizers*. Washington State Department of Labor and Industries, Safety and Health Assessment and Research for Prevention Program (2006).

31. Webster JG. Medical Instrumentation-Application and Design. *Journal of Clinical Engineering* **3**, 306 (1978).

32. Kligman A. The biology of the stratum corneum. *The epidermis* **1**, 387-430 (1964).

33. Webb RC, Bonifas AP, Behnaz A, *et al.* Ultrathin conformal devices for precise and continuous thermal characterization of human skin. *Nature materials* **12**, 938-944 (2013).

34. Webb RC, Ma Y, Krishnan S, *et al.* Epidermal devices for noninvasive, precise, and continuous mapping of macrovascular and microvascular blood flow. *Science advances* **1**, e1500701 (2015).

35. Webb RC, Pielak RM, Bastien P, *et al.* Thermal transport characteristics of human skin measured in vivo using ultrathin conformal arrays of thermal sensors and actuators. *PloS one* **10**, e0118131 (2015).

36. Huang X, Cheng H, Chen K, *et al.* Epidermal impedance sensing sheets for precision hydration assessment and spatial mapping. *IEEE Transactions on Biomedical Engineering* **60**, 2848-2857 (2013).

37. Huang X, Liu Y, Cheng H, *et al.* Materials and designs for wireless epidermal sensors of hydration and strain. *Advanced Functional Materials* **24**, 3846-3854 (2014).

38. Dagdeviren C, Su Y, Joe P, *et al.* Conformable amplified lead zirconate titanate sensors with enhanced piezoelectric response for cutaneous pressure monitoring. *Nature communications* **5**, (2014).

39. Jeong JW, Kim MK, Cheng H, *et al.* Capacitive Epidermal Electronics for Electrically Safe, Long-Term Electrophysiological Measurements. *Advanced healthcare materials* **3**, 642-648 (2014).

40. Norton JJ, Lee DS, Lee JW, *et al.* Soft, curved electrode systems capable of integration on the auricle as a persistent brain–computer interface. *Proceedings of the National Academy of Sciences* **112**, 3920-3925 (2015).

41. Xu B, Akhtar A, Liu Y, *et al.* An Epidermal Stimulation and Sensing Platform for Sensorimotor Prosthetic Control, Management of Lower Back Exertion, and Electrical Muscle Activation. *Advanced Materials*, (2015).

## 1.12 Figures

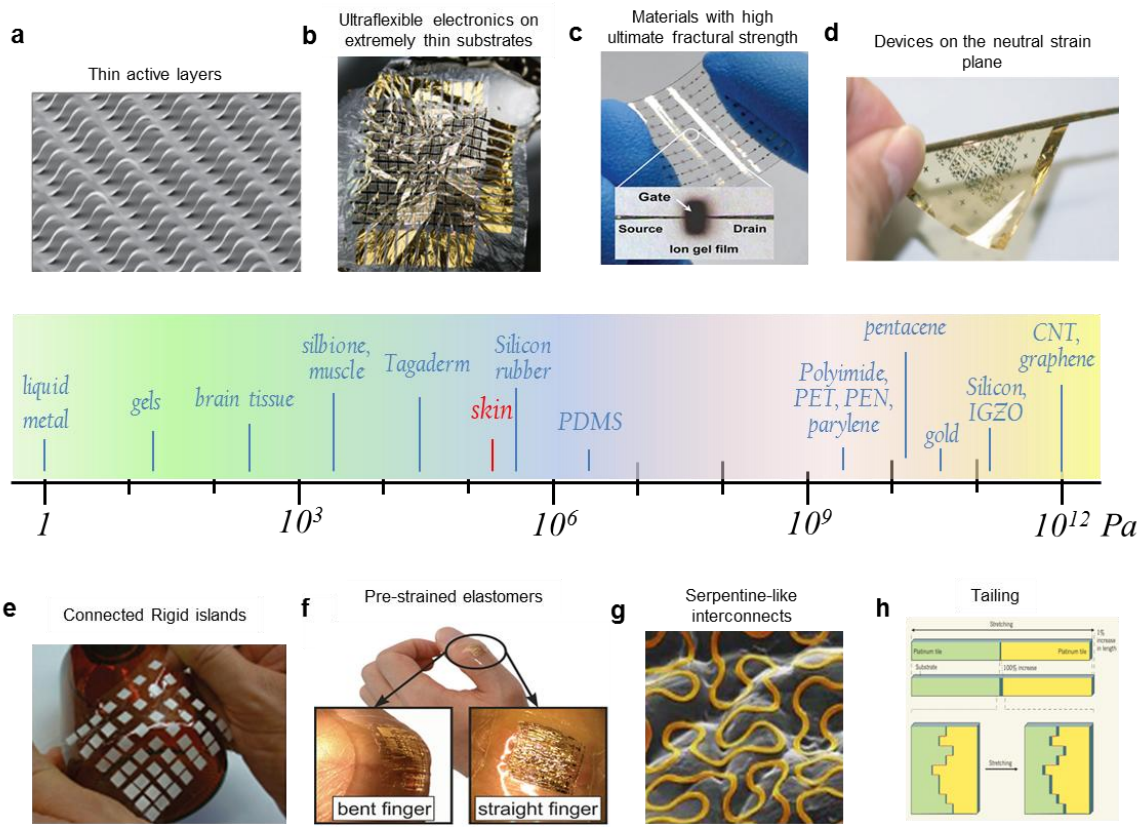


**Figure 1.1 Materials and techniques to achieve stretchable and flexible devices.** The plot in the center compares the Young Modulus of various electronic and biological materials (a) The picture shows silicon nanomenbranes (200nm in thickness) while bending; (b) Utraflexible and imperceptible electroncis can be achieved by using few micron thick substrates; (c) Carbon nanotubes, graphene, can also be used to form highly bendable transistors; (d) Proper encapsulation to place the device on the neutral strain plane is a tricky usually used; (e) Stretchable optoelectronics can be achieved by patterning stiff islands on elastomers; (f) Electronic devices can accommodate up to 200% strain; (g) serpentine-like or/and fractal geometries can be used as layout for interconnections; (h) Tailing at micro or nano scale is another technique usually used to accommodate the stress arising from deformation. Reproduced from references 14, 17-23.

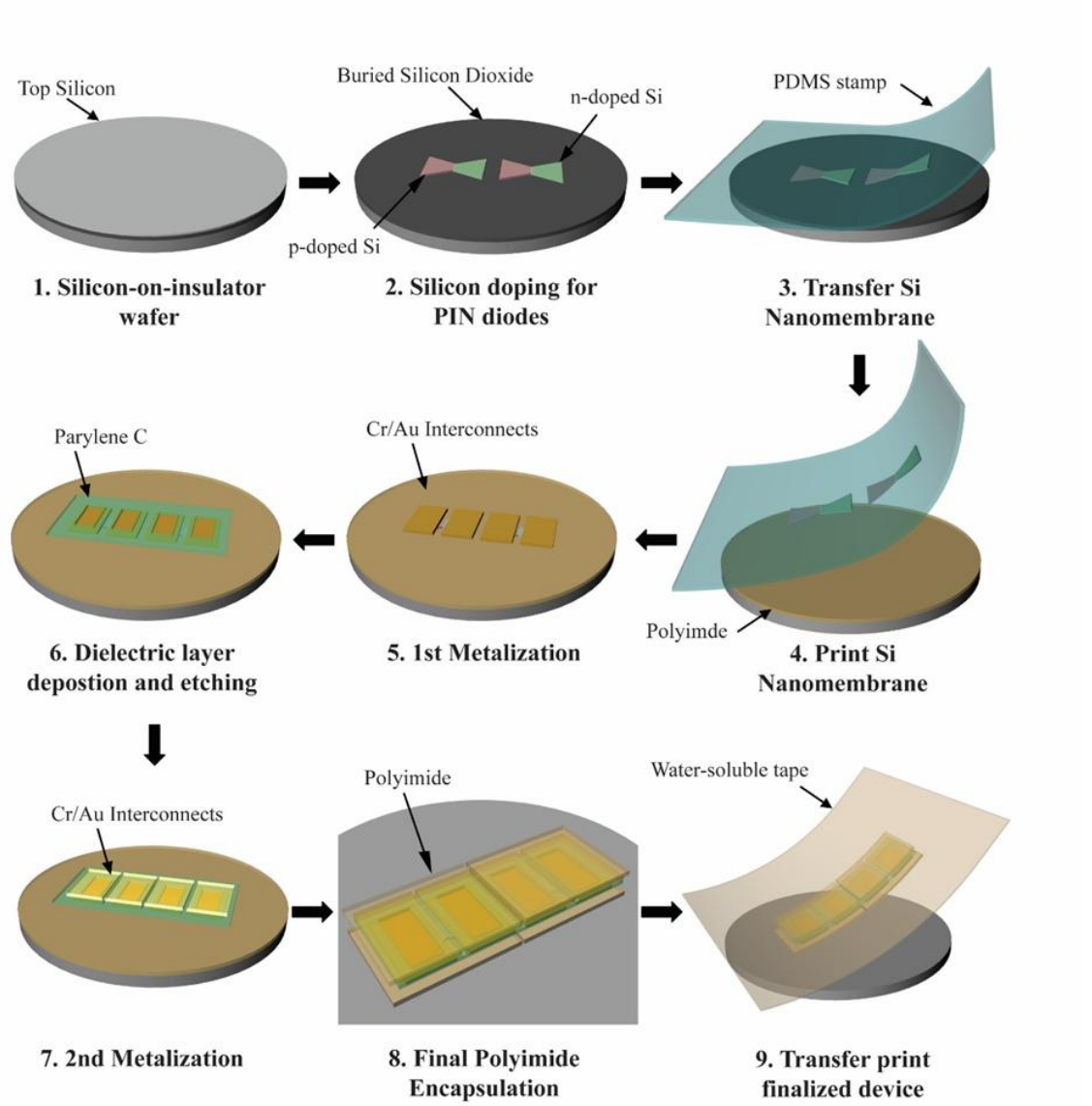


**Figure 1.2 Strategies and steps to fabricate soft electronics on skin.** An example of processing steps of building EES on silicon-on-insulator wafer. The process includes doping, transfer printing, metallization, encapsulation and integration.

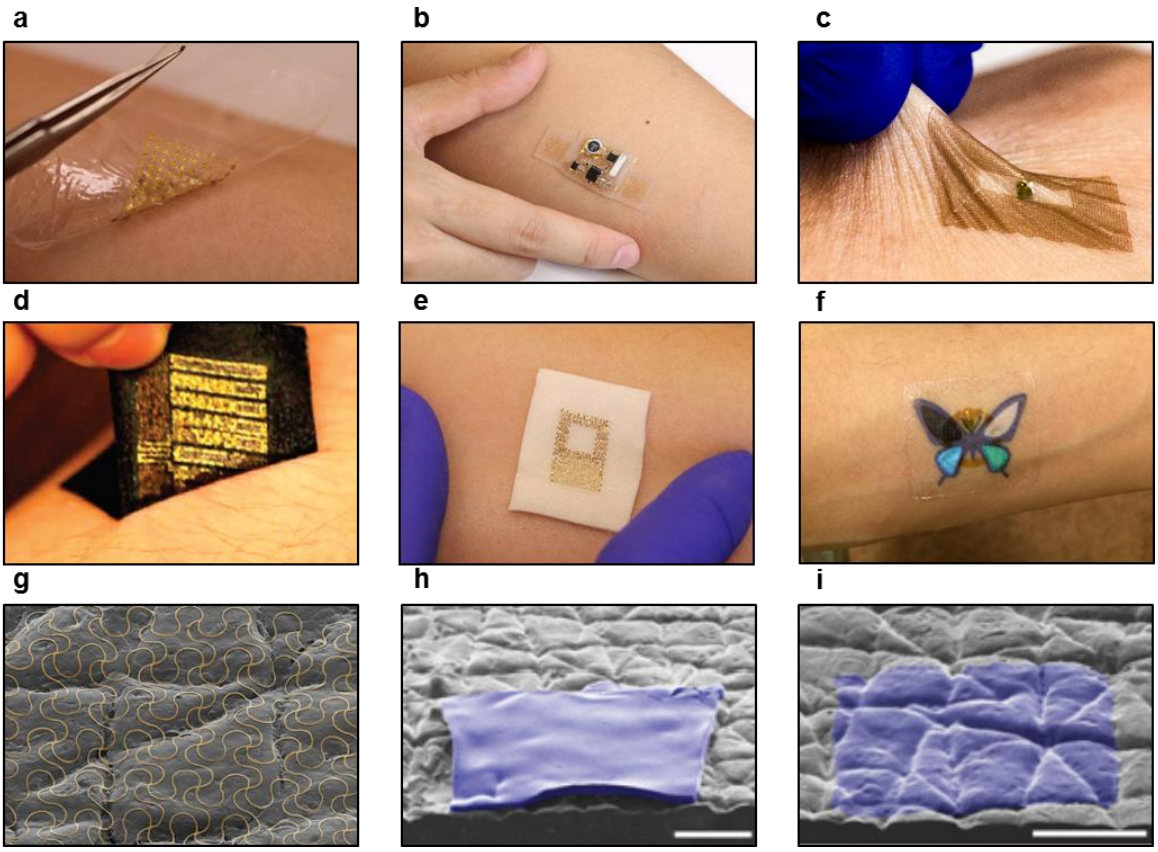


**Figure 1.3 Strategies to intergrate thin and soft electronics on skin.** (a) Hydration sensor on polyvinyl alcohol based PDMS film; (b) Soft radio sensor with commercial chips encapsulated in fluid ecoflex package; (c) NFC tattoo with bare die chip mounted on arcylic adhesive film; (d) Reusable blood oxymetric sensor on strain-limiting fabric with silbione; (e) Sweat sensor on silicone foam; (f) UV sensor with NFC tattoo; (g) Colorized SEM image of 10um Au mesh traces printed on phantom skin; (h) Colorized SEM image of 100 um ecoflex membrane substrate ; (i) Colorized SEM image of 5 um ecoflex membrane substrate. Reoriduced from references 15, 19, 25-28, .

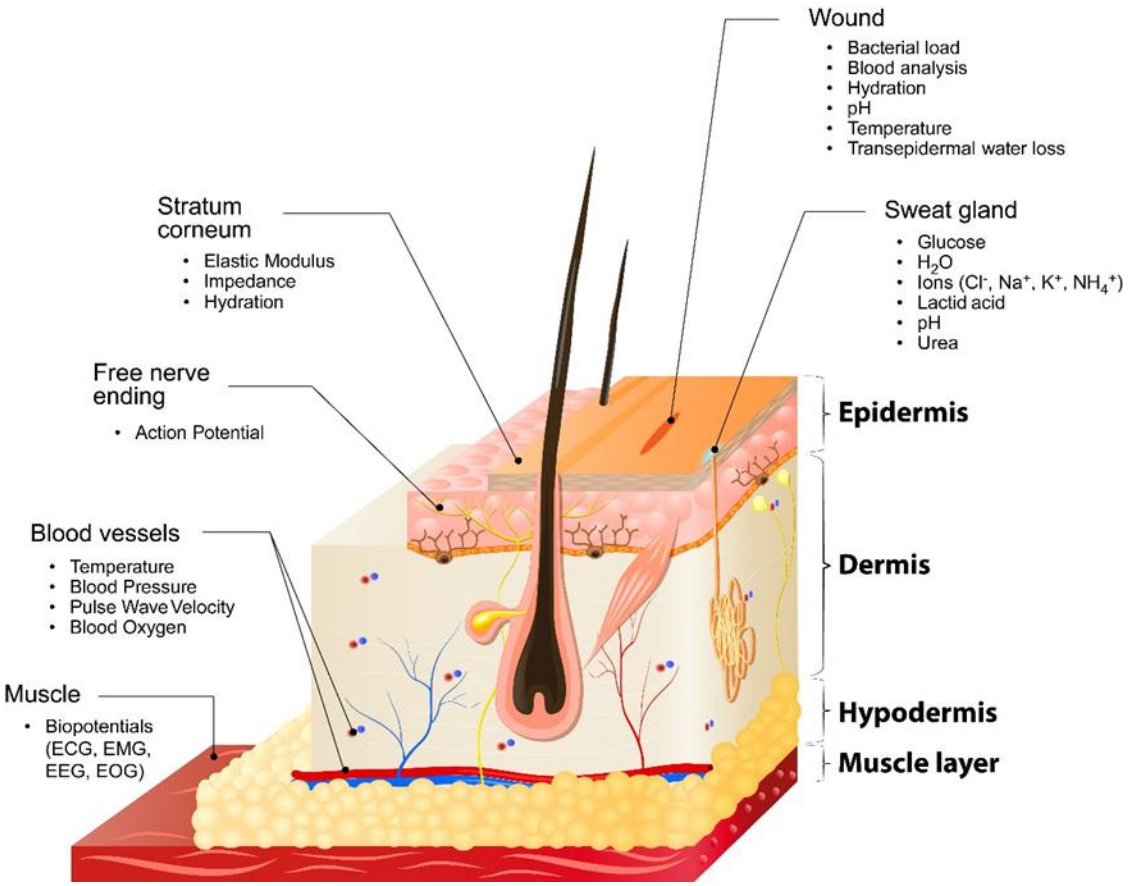


**Figure 1.4 Skin as a diagnostic platform.** Diagnostic signals from muscle, blood vessels, free nerve ending, stratum corneum, woud and sweat gland.

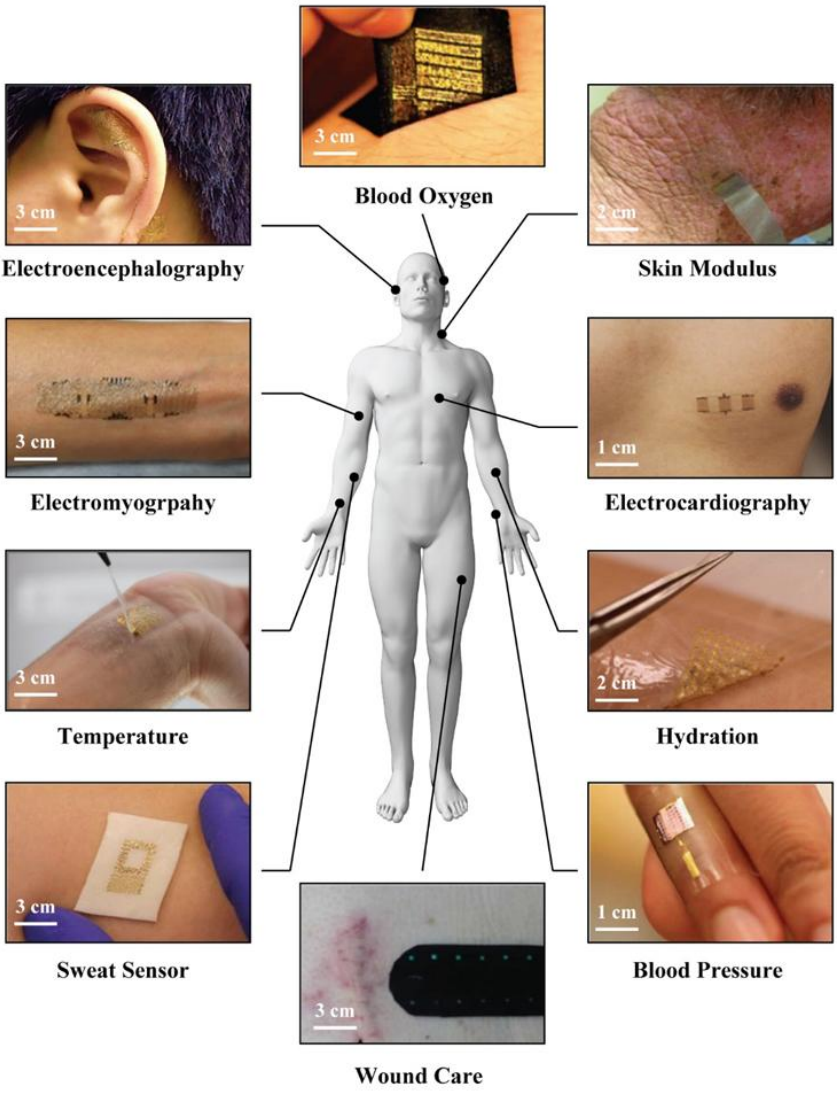


**Figure 1.5 Lab on skin.** Epidermal electronics as biosensors for blood oxygen, skin modulus, electrocardiology, hydration, blood pressure, wound healing rate, sweat content, skin surface temperature, electromyography and electroencephalography measurements. Reproduced from references 15, 25-26, 33-38.

# CHAPTER 2

# EPIDERMAL HYDRATION SENSORS AND SKIN IMPEDANCE STUDIES

Significant portions of this chapter were published as "Epidermal Differential Impedance Sensor for Conformal Skin Hydration Monitoring," Xian Huang, Woon-Hong Yeo, Yuhao Liu, John A. Rogers, *Biointerphases*, 7:52 (2012); "Materials and Designs for Wireless Epidermal Sensors of Hydration and Strain," Xian Huang, Yuhao Liu, *et al.*, *Advanced Functional Materials,* 24.25 (2014); and "Stretchable, wireless sensors and functional substrates for epidermal characterization of sweat," Xian Huang, Yuhao Liu, *et al.*, *Small* 10.15 (2014). Reproduced with permission from the journal.

## 2.1 Introduction

Skin hydration monitoring is a well-established and important technique in dermatology, for analyzing various diseases and determining the effectiveness of medical therapies[1, 2, 3, 4]. Hydration measurement is also useful in cosmetology, for assessing the function of anti-aging and moisturization treatments[5, 6, 7, 8]. Skin hydration levels are typically characterized by measurements of skin electrical impedance[9, 10, 11, 12] or thermal conductivity[13], or by optical spectroscopic techniques[9, 14, 15] including reflectivity[16]. Indirect methods include evaluation of mechanical properties of the skin[17, 18, 19] or its surface geometry[20, 21]. Among these methods, electrical impedance provides the most reliable and established assessment, due to its instrumental simplicity and minimized cost. Several commercial systems that perform this measurement are available[22, 23, 24, 25]. Such technologies generally rely on physical contact between the soft, curved surface of the skin, and rigid, planar electrodes[22]. Here, the accuracy and repeatability both depend critically on the contact force between the electrodes and the skin. As a result, most devices incorporate pressure-sensing components that help the user to apply,

with precision, the appropriate force during measurement. Such devices are not well suited for spatial mapping, for evaluating sensitive areas of the skin, or for continuous monitoring, thereby greatly limiting their utility[26].

Sensors with "epidermal" construction, in which the mechanical properties, thermal loads ($\approx 150\ \mu J\ cm^{-2}K^{-1}$)[27], area mass densities ($< 3.8\ mg\ cm^{-2}$ )[28] and thicknesses (<10 μm) are in the range of the epidermis, can provide intimate skin contact based on Van der Waals forces, likely due to London-dispersion effects between molecules of the skin and the elastomer substrate (e.g., PDMS), thereby eliminating the need of pins, straps, tapes or adhesives[29]. This type of contact offers opportunities in highly repeatable and precise determination not only of properties of the skin itself, but of overall health status in which the skin provides an interface for measurement of internal body processes.

This chapter presents the development of a series of skin hydration sensor with different operating principles and their systematic characterizations. The differential impedance sensor offers compensation for common-mode disturbance during contact measurements with excellent prevision and accuracy. The wireless hydration sensor utilizes inductively coupled magnetic coils and LC resonators to detect variations in resonance frequency induced by changes in skin dielectric properties. The sweat sensor studies the effect of functional substrates for biofluid analysis through LC resonators with capacitive electrodes and colorimetry. At the end, a systematic study on the skin-electrode interface impedances concludes the fundamental studies on impedance-based sensor.

## 2.2 Development of Differential Impedance Sensor

The epidermal hydration measurements reported here[30] use impedance measurements performed directly on the skin, to exploit known correlations between electrical parameters of

biological tissues and their water content[31]. In particular, both the conductivity and permittivity of human skin change with the skin hydration levels[23, 31]. As a result, the hydration levels can be determined through impedance measurements, through appropriate calibration.

Figure 2.1 shows images and schematic illustrations of an epidermal skin hydration sensor platform that consists of pairs of electrodes designed to quantify skin impedance. These electrodes form eight separate measurement channels (figure 2.1a, labels 1 through 8), all with a common electrical ground. Channels 1 through 4 directly contact the skin, while 5 through 8 are insulated from it by thin layers of dielectric with embedded electrodes as floating grounds. We refer to the former (i.e. channels 1–4) and latter (i.e. channels 5–8) as measuring and reference electrodes, respectively. Figure 2.1e provides a cross sectional illustration of a representative pair. Electrodes on common rows have identical geometries and designs: meander (figure 2.1a; top row), interdigitated (figure 2.1a; middle row), and circular (figure 2.1a; bottom row) electrodes. Figure 2.1b shows a magnified view of the last case, with reference and measuring electrodes on the left and right, respectively. The electrodes terminate at bonding pads near the edge of the overall system, joined through interconnect with serpentine geometries in mesh layouts that incorporate square pads at the nodes. Differential detection enabled by combined use of measuring and reference electrodes allows rejection of common mode disturbances in the measurement system as well as impedance changes caused by deformations in the serpentine interconnections.

The accuracy and repeatability of the measurement are both comparable to conventional devices that rely on rigid electrodes and controlled pressures during contact with the skin. The ability to perform internally referenced detection, in a differential mode, and the straightforward scaling to arrays of sensors for spatial mapping applications represent two additional, valuable

features. Development of silicone substrates with enhanced ability to accommodate skin transpiration, and incorporation of wireless data transmission capabilities represent important directions for future work.

## 2.3 Wireless Hydration and Sweat Sensing

### Wireless Hydration Sensing

One appealing approach to epidermal wireless sensing relies on passive inductive coupling, in which changes in the sensing components alter the frequencies of resonant circuits made of inductors and capacitors. This method, usually referred to as wireless passive sensing[32], provides a convenient scheme that does not require active components or power supplies, thereby making it well suited for epidermal integration. Previously reported passive wireless sensors, in conventional, non-epidermal formats, offer capabilities for measurement of intraocular pressure[33], gas flow[34], cerebrospinal fluid shunt function[35], blood pressure[36], and cardiovascular pressure[37].

Realizing these types of systems in epidermal constructs, and optimizing their use in sensors that have simultaneous capabilities of measuring the dielectric and mechanical strain properties of the skin represents the topic of the present report. Skin dielectric measurements serve as effective monitors of various physiological processes[38, 39, 40], and can be conducted at different frequencies for information related to different skin depths[26, 41] and conditions[42]. At frequencies of hundreds of MHz, the effects of relaxation of water molecules dominate. Here, skin dielectric measurements can reveal dermatological and cosmetological effects related to water content in the skin, such as wound healing[42], thermal injury[43], therapeutic effects[44, 45], and abnormal skin conditions, including edema[46, 47] and lymphedema[48]. Strain sensors provide

additional information in such contexts. The following content provides systematic experiments of essential aspects of such classes of epidermal wireless passive sensors, including dielectric assessment of skin properties, hydration measurement, and skin strain induced by lymphedema due to subcutaneous fluid accumulation. Similar techniques, when combined with other sensing mechanisms, such as responses of ligand/receptor binding pairs[49], dielectric changes in humidity or pH sensitive polymers[50, 51], and alignment changes within liquid crystals[52] can yield highly specific, stable, and repeatable, multimodal detection. External sensor readout systems can be adapted to wearable or portable configurations[53, 54], enabling compact and fully functional systems for convenient health and wellness monitoring.

Figure 2.2 shows images and schematic illustrations of a multimodal wireless epidermal device that is 11.4 ×24.2 $mm^2$ in overall dimension and consists of a dielectric sensor and a pair of strain sensors oriented perpendicular to each other. All three sensors are designed to have distinct resonance frequencies, to enable separate readout without crosstalk. The dielectric sensor contains a pair of electrodes in the form of an inner circular disk (500 μm in radius) and an outer circular annulus (800 μm in inner radius and 1.2 mm in outer radius), both in direct contact with the skin, and connected to a coil encapsulated above and below by thin layers of polyimide. The coil consists of 4 turns of copper wire in a serpentine shape, to afford both flexibility and stretchability. The width of the wire is 150 μm, and the lengths of the inner and outer turns are 4.8 and 9.5 mm, respectively. The two strain sensors use serpentine interdigitated electrodes as deformable capacitors, oriented perpendicular to each other to allow sensing of strain in orthogonal directions. The coils for the strain sensors have 2 turns and 1.75 turns, respectively. The interdigitated electrodes formed by serpentine wire (40 μm in width) are approximately 3.2 mm in length with 13 digits and a uniform spacing of 300 μm between adjacent wires. The strain

sensors are entirely encapsulated by polymer to prevent direct skin contact and, thereby, to reduce the influence of the skin dielectric properties on their response. The three sensors are separated to minimize the influence from mutual inductances generated by the nearby or enclosed coils, and thus improve the accuracy of the wireless measurement

As a first example, the wireless sensor is used to define the dielectric properties of the skin at various positions across the body for two male and two female volunteers, at 12 regions (figure 2.3a). For measurement frequencies between 1 MHz and 1 GHz, the dielectric properties of the skin show clear variations with frequency and position, for all four volunteers. A typical spectrum, as in Figure 2.3b, measured with the coaxial cable exhibits a rapidly decreasing dielectric constant at low frequencies (from 1 to 90 MHz), followed by more modest frequency dependence at higher frequencies. This dependence is the smallest in a range of frequencies between 160 to 200 MHz, where the capacitance varies by only ~0.6 % (figure 2.3b). The observed stability of the skin dielectric properties between 160 to 200 MHz may be due to the dominant effect of δ dispersion of bonded and free dipolar water molecules[55, 56], while other frequency-dependent polarization effects are not significant. These trends are similar to those reported elsewhere[56, 57]. The epidermal dielectric sensor is designed with a resonance frequency that lies within this region of minimal frequency dependence.

Measurements collected with the wireless sensor exhibit changes in resonance frequency with position across the body, due to variations in water and fat content of the skin (figure 2.3a). The capacitance of the sensor can be obtained from Eq. (1) (see methods) using its resonance frequency and separate measurements of the inductance of the sensor. This inductance, which is determined using the impedance analyzer (figure 2.3c), is assumed to be less sensitive[32] to changes of skin dielectric properties due to its lack of direct contact with the skin. Electrical

simulation using HFSS (Ansys Inc.) further confirms that the S11 parameter, which is directly related to the impedance of the coil, involves little change when the skin changes from a dry to a wet state. The capacitance determined in this way can be compared to that measured using the coaxial cable probe, at the same frequencies. Trends of capacitance variation with position (figure 2.3d) as measured by the coaxial cable and the epidermal sensor are consistent, as expected. However, symmetry in measurement locations does not lead to symmetrical responses due to strong location dependent properties of skin tissues.

To demonstrate an important mode of measurement, the wireless sensor is used to evaluate the level of hydration of the skin at a position 2 (figure 2.3a) on the forearm. Application of lotion induces variations in hydration levels, which can then be evaluated as a mean to illustrate the measurement capability[30, 58]. The hydration levels are recorded using both a wireless epidermal sensor and a commercial hydration meter. As the hydration level changes from 103 to 31 (arbitrary unit given by the hydration meter), f0 of the device shifts from 163 to 176 MHz (figure 2.4a and b), indicating a decrease in the capacitance and, therefore, the skin dielectric constant, consistent with a decrease in the water content (i.e. hydration). $f_0$ shows little variation, even in the relatively uncontrolled environment of the lab, where mechanical vibrations and temperature fluctuations are present. $f_0$ of the dielectric sensor changes only by approximately 1 MHz for a temperature change of 10 ℃. The measured f0 can be determined easily with a precision of 0.2 MHz, which corresponds to a precision in hydration measurement that is equivalent to 1.1 (arbitrary unit) on the scale of the commercial hydration meter. The hydration measurement result is conducted under lab environment where the humidity is relatively stable. Thus, large variations in environmental humidity have not been considered. However, the influence of the air conditions on the measurement results has been investigated.

The surface of the device that is exposed to air is passivated by polyimide and covered with a perforated silicone layer. This prevents the direct contact between electrodes and air, and thus reduces the response of the sensor to the air humidity. Assessment with air humidity levels drastically varied from 22% to 88% indicated a change in $f_0$ of ~5.8 MHz. This change can be compensated by adding or subtracting a bias value in the hydration measurement result with known humidity levels. In addition, the air humidity will also influence the hydration of the skin. As a result, the influence of air humidity is indirectly reflected by the results from skin hydration detection.

According to resonance frequency equations, the measurement depends critically on the coupling coefficient between the epidermal sensor and the primary coil. The relative position between the coils is, therefore, important. *In-vitro* characterization of the effects is possible through measurements conducted with the wireless sensor on a flat glass substrate, while systematically varying the position of the primary coil. To examine the influence of rotation, the sensor is placed underneath the primary coil at a fixed distance of 8 mm. The rotation of the primary coil is then adjusted using a precision stage. Figure 2.4c shows that the quality factor of the phase curve decreases with counter clockwise rotation around an axis that passes through the center of the primary coil and aligns parallel with the x direction. The measured $f_0$ remains at 238 MHz for rotations between 0 to 80°, but then changes rapidly for larger angles (figure 2.4d). Uniaxial displacements along the z (vertical displacement) (figure 2.4e) and y (horizontal displacement) (figure 2.4f) directions of the primary coil that is originally placed 2 mm above the epidermal sensor are achieved with the xyz mechanical stage. Little change in $f_0$ is observed for a horizontal displacement of up to 1.4 cm and a vertical displacement of up to 0.4 cm, followed with a significant decrease in $f_0$ and Q factor beyond these limits. This measurement

demonstrates a robust range of displacements and angles over which reliable wireless detection can be achieved, with changes of $f_0$ less than 0.4%.

**Epidermal Characterization of Sweat with functional substrates**

An important measurement mode in epidermal electronic devices may involve the analysis of body fluids (blood, interstitial fluid, sweat, saliva, and tear), to gain insights into various aspects of physiological health[59, 60, 61, 62]. Such function in wearable sensors, generally, and epidermal electronics in particular, is relatively unexplored. Existing devices either use complex microfluidic systems for sample handling[63, 64, 65, 66] or involve purely concentration-based measurement without sample collection and storage, without access to parameters related to quanity and rate[67, 68, 69]. In addition, mechanical fixtures, straps and/or tapes that are typically required to maintain contact of these devices with the skin do not lend themselves well to continuous, long term monitoring without discomfort [70]. In the following, we report a set of materials and device architectures that provide advanced capabilities in this area. The key concept involves the use of functional soft substrates to serve as a means for microfluidic collection, analysis and presentation to co-integrated electronic sensors and/or external camera systems. The pores of these substrates spontaneously fill with body fluids that emerge from the skin, where they simultaneously induce colorimetric changes in the substrate and alter the radio frequency characteristics of integrated electrical antenna structures. The results offer valuable insights into properties and volume of sweat, and their relationships to fluctuations in body temperature[71], fluid and electrolyte balance[72], and disease state[73]. The devices also eliminate the need for direct skin-electrode contacts, thereby minimizing irritation that can be caused by contact between the skin and certain metals[74], while at the same time enabling repeated use of a

single device and minimal noise induced by motion artifacts. The sensors exploit inductive coupling schemes, without on-chip detection circuits but with some potential for compatibility with near-field communication systems that are found increasingly in portable consumer electronic devices. The entire sensing system offers flexible and stretchable mechanics, with form factors that approach those of epidermal electronics.

Figure 2.5a shows images and schematic illustrations of a typical device (22×28 $mm^2$ in the surface area of the substrate, and 10×15 $mm^2$ for the dimension of the sensor) that includes an inductive coil and a planar capacitor formed with interdigitated electrodes. The coil consists of four turns of thin copper traces in a filamentary serpentine design that affords both flexibility and stretchability. The width of the trace is 140 μm, and the lengths of the inner and outer turns are 4.8 and 9.5 mm, respectively. The electrodes consist of serpentine wires (50 μm in width) that have lengths between 6.5 to 8.4 mm, to form 9 digits with a digit-to-digit spacing of 600 μm. The dielectric properties of the microporous supporting substrate strongly influence the capacitance of the structure.

In this way, the sweat sensor enables capacitive detection of the change of the dielectric properties of the substrate as its pores fill with biofluids (e.g. sweat). An external primary coil generates a time varying electromagnetic field that induces a current flow within the sensor. The impedance of the sensor is then determined by the amount of sweat within the substrate; this impedance influences that of the primary coil placed in proximity to the device. The resonance frequency ($f_0$) of the sensor can be determined from the frequency of a phase dip (or a peak in the phase difference, $\Delta\theta$, obtained from the subtraction of the phase of the primary coil with and without the sensor underneath) in the phase-frequency spectrum of the primary coil [75, 76, 77, 78]. At measurement frequencies examined here (100~200 MHz), free water molecules are under the

influence of δ relaxation [79]. The response of the functional polymer substrates only involve contributions from induced charges. The movement of the water molecules and dynamics of the induced charges are sufficiently fast to respond to the external electromagnetic field. As a result, the combined dielectric properties of substrate and the sweat exhibit an invariant dielectric response over a wide range of frequencies.

The sensor offers mechanical properties (elastic modulus≈80 kPa) similar to those of the skin [80]. The thickness of the substrate (1 mm), along with its lateral dimensions and porosity define the amount of fluid that it can capture. The devices exhibit robust, elastic behavior under axial stretching (figure 2.5b and 2.5c) and other more complex modes of deformation (figure 2.5d). Attachment of the sensor onto the skin (figure 2.5e) using a thin layer of commercial spray-on bandage as adhesive leads to reversible skin/sensor bonding that can withstand significant extension and compression of the skin with sufficient mechanical strength to prevent delamination (figure 2.5f and 2.5g).

*In-vitro* experiments involve slow introduction of 0.6 mL of buffer solution (phosphate buffered saline, Sigma-Aldrich Corporation, St. Louis, Mo, USA) onto the substrates with a syringe pump, over the course of ~40 minutes (figure 2.6d). The resonance frequency of the sensor ($f_0$), as measured by the shift of the phase peak of a primary coil placed in proximity to the device (figure 2.6c), decreases with increasing buffer solution content in the substrate. This response reflects increases in both the capacitance of the sensor and the permittivity of the substrate, due to replacement of air with the buffer solution in the pores of the substrate. For a typical porous polyurethane (PUR) substrate (figure 2.6a), $f_0$ shifts from 195.3 to 143.3 MHz in this experiment (figure 2.6d). Drying of the sensor in air at room temperature leads to the

recovery of $f_0$, eventually to the original value (195.3 MHz) over a period of ~6 hours, indicating a reversible response with relative insensitivity to residual salt that might remain in the substrate.

Assessment of performance on human subjects involves use of sensors on cellulose paper (CP) and silicone substrates attached to the arms of two volunteers. Reference substrates made of the same materials with silimiar sizes placed in close proximity to the sensors provide means for determining the accuracy and establishing a calibrated response (figure 2.6b). The monitoring includes measuring the value of $f_0$ of the sensors and the weight of the reference substrates every 5 mins for a period of 2 hours. The results indicate that $f_0$ is inversely proportional to the weight of the reference sensor, such that the response can be calibrated with any two measured weights. The calibrated results closely follow weight changes of 0.4 (figure 2.6e) and 0.2 g (figure 2.6f) in the reference substrates, corresponding to 0.4 and 0.2 mL of sweat over the sensing areas.

The coil structures can be mounted onto various types of functional substrates. Demonstrated examples include recycled cellulose sponge (RCS), polyurethane sponge (PUR), polyvinyl alcohol sponge (PVAS), cellulose paper (CP), and silicone sponge (figure 2.7a). Cutting with a hot-wire device (PUR, silicone) or with a razor blade (other) yields the appropriate lateral dimensions and thicknesses. Spin-coated silicone films with accurately controlled thickness (~10 μm; figure 2.7b) enable strong bonding between each of these functional substrates and the sensors through surface chemical functionalization, while preventing direct contact between the sensors and the sweat. Relative characteristics in water absorption are also important to consider, as described in the following.

The percentage gain in weight of the various porous materials after immersion in water defines their ability to hold fluids; the results are ~2300% (RCS), ~1200% (PUR), ~750% (PVAS), ~350% (CP), and ~1500% (silicone) (figure 2.7c). These data, together with measured

volume changes yield the porosity levels: 0.97 (RCS), 0.93 (PUR), 0.90 (PVAS), 0.83 (CP) and 0.95 (silicone) (figure 2.7d). The water permeability can be determined from the capillary water absorption rate by combining Darcy's law [81] and the Hgaen-Poiseuille equation[82]. Strips of the substrates (3mm in width and 28 mm in length) are partially immersed into water with red dye (3 mm under the water). A camera enables measurements of changes in height of the absorbed water as a function of time (figure 2.7e). The CP material exhibits the fastest absorption rate (complete filling in ~6 s), followed by the RCS (~25 s). The PUR shows the smallest rate, with an increase in height of 8.3 mm over 130 s. These rates depend strongly on the pore size and degree of interconnectedness and on the contact angle. The latter can be determined optically; the former can be obtained by scanning electron microscopy or by calculation and measurement of the height of absorbed water at long time (details in supporting information). The permeability of the five substrates are 2.4 (RCS), 0.3 (PUR), 0.4 (PVAS), 8.7 (CP), and 8.6 (silicone) $\mu m^2$ (figure 2.7f).

## 2.4 Skin-electrode Interface Impedance

The electrical properties of skin-electrode interface determine the performance of EES. The higher impedance from incomplete contact and materials defects cause smaller signal-to-noise ratio in sensing, and discomfort in current stimulation. However, the effects of materials selection, layout design and degree of contact to the interfacial impedance were not yet well understood. Here, a systematic study of equivalent circuit models presents a set of optimal design rules to achieve lower skin-electrode interface impedance by tuning the fill factor, line-width and coating materials.

Using current stimulation as an example (figure 2.8a), when both anode and cathode are placed on skin surface, a current delivers the stimulation profile by depolarizing both sides of

electrodes simultaneously. As the charges stored at the interface, a double-layer capacitance developed as well. The continuing accumulation of charges eventually dissipates to the skin tissues, causing a charge-transfer across the double-layer and injects currents. This comes to equilibrium when all charges stored are dissipated and net electroneutrality is established. If there are gaps between the electrodes and the skin tissues, it will first (1) increase the path resistance for charge dissipation, (2) distort the charge storage at the interface and cause non-uniform current density during charge dissipation.

Epidermal mesh electrodes made of gold (300 nm, 22 x 22 mm) with 50, 100, 150 μm line-width and 10%, 30%, 50%, 70% fill factor were used to study the skin-electrode interface. As a baseline measurement, impedance spectroscopy test in phosphate buffer solution (PBS) was first performed in 3 electrode configuration as shown in figure 2.8b. While only working electrode is the testing electrode, it ensures a direct comparison of one electrode interface. The Reference electrode is Ag/AgCl and the counter electrode is platinum, both placed at the same distance to each other in a glass beaker. The result (figure 2.8c) shows an expected trend of decreasing impedance with increasing fill factor, showing an area-dependence. While the area of the mesh electrode with different line-widths but same fill factor should be identical, the impedance values have small random variations possibly due to fabrication defects. Further characterization of these electrodes require curve fitting using Randell cell model of the skin-electrode interface (figure 2.8d). The extracted values of the electrolyte resistance remain constant across all line-widths and fill factors, as expected since the PBS solution resistance should be a constant (figure 2.8e). The extracted charge-transfer resistance and double-layer capacitance, however, shows opposite trends. The charge-transfer resistance decreases with increasing fill factor as expectation (figure 2.8f), but the 100 μm mesh electrode has the lowest

values than 150 μm one, indicating there is either a defect in the 150 μm samples, or there are other unknown parameters limiting charge-transfer in electrodes with wider line-width. The differences between line-widths diminish significantly after 50% fill factor, showing a plateau for interfacial resistance. The double-layer capacitance again, steadily increases with electrode surface area, which follows the ideal capacitor law (figure 2.8g).

The impedance spectroscopy measurement on skin (figure 2.9) shows slightly different behaviors. Similar to previous experimental setup, only epidermal mesh metal electrodes are used as working electrode; both counter and reference electrode are hydrogel commercial electrodes at 22 mm x 22 mm. The epidermal electrodes were transfer-printed on thin Tagederm medical tape (~50 μm) with strong adhesive that ensure comfort contact with skin. Measured impedance decrease with increasing fill factor from 10% to 50%, however, 70% electrodes show either higher or similar impedance than 50% in all three electrode line-widths at most of the frequency range. We hypothesize the cause of this behavior to an optimal contact between skin and electrode at around 50%, increasing the fill factor could reduce the contact area due to local buckling and delamination of mesh materials. Further investigation using scanning electron microscope is needed to verify this hypothesis. In addition, the 100 μm electrodes exhibits lower impedance results than 50 μm electrodes, contradicting the previous observation in PBS solution. This is due to dielectric property changes of skin over time, as measurements of 50, 150 μm electrodes were done at a different time than 100 μm electrodes, causing the variation in skin condition. It is important to note that the absolute values of skin impedance values may not be useful to make comparisons between different subjects or measurement done at different times. The range of skin impedance varies to 100 kΩ to 5 MΩ in this study on the same subject.

## 2.5 Conclusions

This chapter presents a systematic study of epidermal hydration sensor that illustrate a soft, “skin-like” technology, capable of intimately and non-invasively integrating with the skin for the purpose of quantitative assessment of hydration levels. Several electrode designs, materials selection, and sensing mechanisms were carefully studied and compared with commercial available tools.

The wireless passive sensor technology introduced here provides a soft, ‘skin-like’ device that enables intimate integration with the skin and non-invasive, wireless quantification of skin dielectric properties related to water contents and mechanical strains induced by excessive subcutaneous fluid accumulation (lymphedema). The sensors exhibit some tolerance to misalignment with the primary coil, as required for practical use in wearable applications. With a maximum voltage level of 1V output from the impedance analyzer, the measurement distance between the primary coil and the epidermal sensor is limited to 1.4 cm. One attractive possibility for use outside of a laboratory setup might involve near field communication (NFC) techniques that are available in many portable consumer electronic devices. In addition, when combined with other bio-molecule recognition and chemical sensing techniques, this type of epidermal wireless sensor can be constructed as a multifunctional sensing patch, with potentially important uses in continuous health monitoring.

The sweat sensor study presented here provide materials and design strategies for integrating flexible and stretchable wireless sensors on functional substrates. Demonstrated devices intimately integrate with the skin to provide non-invasive, wireless quantification of sweat loss as well as colorimetric detection for sweat composition. Similar strategies can be used to develop sensors for monitoring a range of key parameters associated not only with sweat but with other body fluids.

## 2.6 Methods

**Epidermal Differential Hydration Sensor.** The sensors exploit three different designs. The circular electrodes involve a concentric design (Fig. 1b), consisting of inner disks (150 or 125 μm in radius) surrounding by open-ended rings (inner radius: 200 μm, outer radius: 300 μm). The interdigitated electrodes incorporate 8 (upper digit) or 7 (bottom digit) fingers each with dimensions of 20 x 50 $\mu m^2$ and spacing of 20 μm. The meander electrodes involve two sets of four semicircular lines (radii: 30, 90, 150, and 210 μm, width: 20 μm) and two 60˚ and 150˚ arc lines (radii: 310 and 270 μm, width: 20 μm) interconnected into spiral shapes. In each of these three cases, the electrodes connect to corresponding bonding pads (width: 500 lm, spacing: 500 μm) and a common ground pad through serpentine traces (width 50 μm; ~ 225 μm radii of curvature). The floating ground plates consists of 600 x 600 $\mu m^2$ pads situated above the reference electrodes and connected with serpentine traces through vias in the PI (230 x 230 $\mu m^2$ in dimension). The use of different electrode designs in a single device allows us to assess various hydration sensing methods and sensor parameters under the same experimental conditions. The meander electrodes perform as resistors, which can be used for assessment of skin hydration through purely resistivity measurement. The other electrodes measure both resistance and capacitance changes. The circular electrodes offer symmetries that facilitate theoretical analysis; these geometries are also found in macroscale electrodes used in Commercial Moisture Meter (CMM), to enable direct comparison.

**Fabrication of wireless hydration sensor.** The fabrication starts with spin-coating a layer of polydimethylsiloxane (PDMS, 20 μm thick) onto a glass slide. Curing the PDMS and treating its surface with reactive ion etching (RIE) enables spin casting of a layer of polyimide (PI; 1 μm

thick) on top. Serpentine interdigitated electrodes and circular electrodes consist of photolithographically patterned layers of copper (500 nm) deposited by electron beam evaporation. An additional coating of PI (1 μm) electrically insulates the surfaces of the electrode patterns; RIE removes selected regions of the PI to define points of electrical contact with the skin. Another patterned layer of copper (5 μm) forms serpentine coils, which are encapsulated by another PI coating. Etching of the entire system into an open mesh layout completes the main part of the fabrication. A water-soluble tape of cellulose (Aquasol ASWT-2) allows retrieval of the sensor from the PDMS substrate. Deposition of Ti/SiO2 (5/60 nm) onto the exposed backside of the sensor by electron beam evaporation facilitates chemical bonding to an ultrathin perforated silicone substrate (5 μm in thickness) (Solaris, Smooth-On, Inc.) after UV ozone activation. Dissolving the cellulose tape with water yields an integrated device with excellent levels of mechanical stretchability and flexibility, to facilitate intimate contact with the skin.

**Wireless hydration detection.** The sensors are evaluated using an impedance analyzer (HP 4291a RF Impedance / Material Analyzer) with a frequency range from 1 MHz to 1.8 GHz. The analyzer connects to a hand-wound copper primary coil whose resonance frequency is significantly different from the epidermal wireless sensor. The impedance analyzer sweeps across 801 frequencies distributed linearly in the designated measurement frequency range. The signal amplitude (~1 V) is sufficiently small to avoid any significant heating on the skin as verified by thermal images collected with an infrared camera (FLIR SC600). A xyz mechanical stage and a rotational platform allow manual adjustments of the position and orientation of the primary coil relative to the epidermal sensors. The primary coil can be either positioned on this stage, for systematic studies, or it can be an accessory to clothing, for more practical applications.

The primary coil provides time varying electromagnetic fields that induce alternating voltages in the epidermal coils. Changes of the dielectric properties of the skin and/or mechanical strains lead to changes in the capacitances of the different sensing components and, therefore, their resonance frequencies. The operation should be carried out in ranges of frequencies where the dielectric properties are relatively frequency independent. In such ranges, the permittivity of the skin is determined primarily by water content, fat, hydration levels and other properties of interest[83, 84]. A conventional sensor based on an open-ended coaxial cable equipped with a pair of electrodes with sizes matched to those of the epidermal dielectric sensor enables acquisition of comparative data.

The resonance frequency of the epidermal sensor is determined by the min-phase method[77, 85], in which a frequency ($f_{min}$) where the phase of the impedance of the primary coil reaches its minimum serves as an approximate measure of the resonance frequency of the epidermal sensor ($f_0$), given by

$$f_0 = 1/(2\pi\sqrt{L_E C_E}) \quad (1)$$

where $L_E$ and $C_E$ are the inductance and capacitance of the epidermal sensor, respectively. The impedance of the primary coil ($Z_P$) measured by the impedance analyzer can be expressed as

$$Z_P(\omega) = R_P + j\omega L_P + \omega^2 M^2 / Z_E(\omega) \quad (2)$$

The impedance of the epidermal sensor ($Z_E$), the resistance ($R_P$), and inductance ($L_P$) of the primary coil all influence $Z_P$. The impedance of the epidermal sensor can be further expressed as:

$$Z_E(\omega) = R_E + j\omega L_E - j1/(\omega C_E) \quad (3)$$

The coupling coefficient ($k$) and the quality factor ($Q$) of the epidermal sensor can be expressed as

$$k = M/\sqrt{L_P L_E}$$
$$Q = \sqrt{L_E}/(R_E\sqrt{C_E}) \quad (4)$$

where $M$ is the mutual inductance of the primary and epidermal coils. Terms in Eq. (3) can then be written

$$L_E C_E = 1/\omega_0^2$$
$$R_E = \omega_0 L_E/Q \quad (5)$$

The impedance of the primary coil is

$$Z_P(\omega) = R_P + j\omega L_P\left[1 + k^2\omega^2/\omega_0^2(1 - \omega^2/\omega_0^2 + j\,\omega/\omega_0 Q)\right] \quad (6)$$

With a phase of $\angle Z_P$ be expressed as

$$\angle Z_P(\omega) = \arctan(\mathrm{Im}(Z_P(\omega)/\mathrm{Re}(Z_P(\omega)) \quad (7)$$

Setting the derivative of $\angle Z_E(\omega)$ to zero yields an expression for $f_{\min}$. A Taylor series expansion provides a simple approximate relationship between $f_{\min}$ and $f_0$

$$f_{\min} = f_0(1 + k^2/4 + 1/8Q^2) \quad (8)$$

Because the $Q$ of the epidermal sensor is typically >20, the term $1/8Q^2$ can be neglected. The coupling coefficient $k$ represents the efficiency of the interaction between two coils, and is thus $0<k<1$[78]. As a result, we can assume that $f_{\min} \approx f_0$ for the rest of analysis[78]. Variations in the phase of the impedance of the primary coil itself can be subtracted from measured data by using a reference curve obtained from the primary coil evaluated without the presence of the epidermal sensors, in the same measurement location. This process eliminates the large background signal associated with the primary coil, thereby highlighting changes in phase caused by the epidermal sensor. In the following, shifts in phase relative to the reference phase of the primary coil are used, rather than the direct phase curve from the primary coil.

**Fabrication of sweat sensing patch.** The fabrication starts with spin casting a layer of polydimethylsiloxane (PDMS, 20 μm thick) onto a glass slide. Curing the PDMS and treating its surface with reactive ion etching (RIE) allows conformal coating of a layer of polyimide (PI; 1 μm thick) on top. Serpentine interdigitated electrodes consist of photolithographically patterned layers of gold (200 nm) deposited by electron beam evaporation. An additional coating of PI (1 μm) electrically insulates the surfaces of the electrode patterns. Selective RIE exposes regions for electrical contact with serpentine coils formed by a patterned layer of copper (6 μm). The entire patterns are encapsulated by another PI coating. Patterned RIE of the entire system yields an open mesh layout, capable to release onto the surface of a target substrate by use of water-soluble tape (Aquasol ASWT-2, Aquasol Corporation, North Tonawanda, NY, USA ). To prepare the functional substrates, a layer of uncured silicone (10 μm thick) is spin-cast onto a water soluble tape fixed on its edges to a glass slide by Scotch tape. Pre-curing the silicone at 150 $^{o}$C for 1 min transforms the liquid precursor into a tacky, soft solid. Placing the substrates on the silicone film with gentle pressure allows the partially cured film to crosslink with porous structures on the surface of the substrates. The silicone and the substrates are then fully cured at 120 $^{o}$C to achieve robust bonding. The resulting structure is removed from the glass substrate, and rinsed with water to remove the water soluble tape. Deposition of Ti/$SiO_2$ (5/60 nm) onto the exposed backside of the sensor facilitates chemical bonding to the PDMS film on the functional substrates after UV ozone activation. Dissolving the water soluble tape yields an integrated device with excellent levels of mechanical stretchability and flexibility. The functional substrates can be immersed into colorimetric indicators, followed by baking at 100 ℃ on a hotplate to dry the devices.

Five hydrophilic porous substrates serve as the sweat absorption materials, including Whatman GB003 cellulose paper (GE Healthcare Life Sciences, Pittsburgh, PA, USA), Scotch-Brite recycle cellulose sponge (3M Cooperation, St. Paul, MN, USA), polyvinyl alcohol sponge (Perfect & Glory Enterprise Co., Ltd., Taipei), Kendall hydrophilic polyurethane foam dressing (Covidien Inc., Mansfeld, MA, USA), and Mepilex silicone foam dressing (Mölnlycke Health Care AB, Sweden). For colorimetric detection, a universal pH indicator (pH 2-10) (Ricca Chemical, Arlington, TX, USA) yields responses to buffer solutions with well-defined pH (Sigma-Aldrich Corporation, St. Louis, Mo, USA). Colorimetric copper and iron ion detection is enabled by a copper color disc test kit (CU-6, Hach Company, Loveland, Colorado, USA ) and an iron color disc test kit (IR-8, Hach Company, Loveland, Colorado, USA), while standard stock solutions of copper and iron (Hach Company, Loveland, Colorado, USA) are diluted to achieve different ion concentrations.

The sensors can be integrated onto the skin using a process as shown in the movie in the supporting information. Briefly, spray bandage (Nexcare No Sting Liquid Bandage Spray, 3M Cooperation, St. Paul, MN, USA) is first applied onto the corresponding skin region. Evaporation of the solvent results in a tacky, water-permeable film that does not significantly influence the transdermal water loss from the skin and provides sufficient adhesion to fix the sweat sensors onto the skin. The sensor is then applied to the skin with continuous pressure over several seconds. The bonding is reversible, but is sufficiently strong to accommodate heavy sweating and shear forces.

## 2.7 References

1. Blichmann C, Serup J. Hydration studies on scaly hand eczema. *Contact Dermatitis* **16**, 155-159 (1987).

2. Boguniewicz M, Nicol N, Kelsay K, *et al.* A multidisciplinary approach to evaluation and treatment of atopic dermatitis. Frontline Medical Communications (2008).

3. Kleiner SM. Water: an essential but overlooked nutrient. *Journal of the American Dietetic Association* **99**, 200-206 (1999).

4. Sharma V, Sridharan K, Pichan G, *et al.* Influence of heat-stress induced dehydration on mental functions. *Ergonomics* **29**, 791-799 (1986).

5. Choi JW, Kwon SH, Huh CH, *et al.* The influences of skin visco-elasticity, hydration level and aging on the formation of wrinkles: a comprehensive and objective approach. *Skin Research and Technology* **19**, e349-e355 (2013).

6. Gerhardt L-C, Strässle V, Lenz A, *et al.* Influence of epidermal hydration on the friction of human skin against textiles. *Journal of The Royal Society Interface* **5**, 1317-1328 (2008).

7. Verdier-Sévrain S, Bonte F. Skin hydration: a review on its molecular mechanisms. *Journal of cosmetic dermatology* **6**, 75-82 (2007).

8. Zhang M, Mak A. In vivo friction properties of human skin. *Prosthetics and orthotics international* **23**, 135-141 (1999).

9. Frödin T, Helander P, Molin L, *et al.* Hydration of human stratum corneum studied in vivo by optothermal infrared spectrometry, electrical capacitance measurement, and evaporimetry. *Acta dermato-venereologica* **68**, 461-467 (1987).

10. Paye M, Gaer D, Morrison B. Corneometiy measurements to evaluate skin dryness in the modified soap chamber test. *Skin Research and Technology* **1**, 123-127 (1995).

11. Sasai S, Zhen YX, Tagami H. High-frequency conductance measurement of the skin surface hydration state of dry skin using a new probe studded with needle-form electrodes (MT-8C). *Skin Research and Technology* **2**, 173-176 (1996).

12. Tagami H, Ohi M, Iwatsuki K, *et al.* Evaluation of the skin surface hydration in vivo by electrical measurement. *Journal of Investigative Dermatology* **75**, 500-507 (1980).

13. Xiao P, Ciortea L, Singh H, *et al.* Opto-thermal in-vivo skin hydration measurements–a comparison study of different measurement techniques. IOP Publishing (2010).

14. Attas EM, Sowa MG, Posthumus TB, *et al.* Near-IR spectroscopic imaging for skin hydration: The long and the short of it. *Biopolymers* **67**, 96-106 (2002).

15. Kadlec F, Berta M, Kužel P, *et al.* Assessing skin hydration status in haemodialysis patients using terahertz spectroscopy: a pilot/feasibility study. *Physics in medicine and biology* **53**, 7063 (2008).

16. Alekseev S, Szabo I, Ziskin M. Millimeter wave reflectivity used for measurement of skin hydration with different moisturizers. *Skin Research and Technology* **14**, 390-396 (2008).

17. Dobrev H. Use of Cutometer to assess epidermal hydration. *Skin Research and Technology* **6**, 239-244 (2000).

18. Hendriks F, Brokken D, Oomens C, *et al.* Influence of hydration and experimental length scale on the mechanical response of human skin in vivo, using optical coherence tomography. *Skin Research and Technology* **10**, 231-241 (2004).

19. Liang X, Boppart SA. Biomechanical properties of in vivo human skin from dynamic optical coherence elastography. *IEEE Transactions on Biomedical Engineering* **57**, 953-959 (2010).

20. Hendriks FM. Mechanical behaviour of human epidermal and dermal layers in vivo. (2005).

21. Tan G, Xu P, Lawson LB, *et al.* Hydration effects on skin microstructure as probed by high-resolution cryo-scanning electron microscopy and mechanistic implications to enhanced transcutaneous delivery of biomacromolecules. *Journal of pharmaceutical sciences* **99**, 730-740 (2010).

22. Barel AO, Clarys P. In vitro calibration of the capacitance method (Corneometer CM 825) and conductance method (Skicon-200) for the evaluation of the hydration state of the skin. *Skin Research and Technology* **3**, 107-113 (1997).

23. Clarys P, Barel AO, Gabard B. Non-invasive electrical measurements for the evaluation of the hydration state of the skin: comparison between three conventional instruments-the Comeometer® , the Skicon® and the Nova DPM® . *Skin Research and Technology* **5**, 14-20 (1999).

24. Fluhr JW, Gloor M, Lazzerini S, *et al.* Comparative study of five instruments measuring stratum corneum hydration (Corneometer CM 820 and CM 825, Skicon 200, Nova DPM 9003, DermaLab). Part I. In vitro. *Skin Research and Technology* **5**, 161-170 (1999).

25. Alanen E, Nuutinen J, Nicklén K, *et al.* Measurement of hydration in the stratum corneum with the MoistureMeter and comparison with the Corneometer. *Skin Research and Technology* **10**, 32-37 (2004).

26. Martinsen Ø G, Grimnes S, Haug E. Measuring depth depends on frequency in electrical skin impedance measurements. *Skin Research and Technology* **5**, 179-181 (1999).

27. Webb RC, Bonifas AP, Behnaz A, *et al.* Ultrathin conformal devices for precise and continuous thermal characterization of human skin. *Nature materials* **12**, 938-944 (2013).

28. Kim D-H, Lu N, Ma R, *et al.* Epidermal electronics. *science* **333**, 838-843 (2011).

29. Tadros T. Colloids in Cosmetics and Personal Care, Vol. 4. Wiley-VCH GmbH and Co. KGaA (2008).

30. Huang X, Yeo W-H, Liu Y, *et al.* Epidermal differential impedance sensor for conformal skin hydration monitoring. *Biointerphases* **7**, 52 (2012).

31. Yamamoto T, Yamamoto Y. Electrical properties of the epidermal stratum corneum. *Medical and biological engineering* **14**, 151-158 (1976).

32. Tan EL, Ng WN, Shao R, *et al.* A wireless, passive sensor for quantifying packaged food quality. *Sensors* **7**, 1747-1756 (2007).

33. Chen P-J, Rodger DC, Saati S, *et al.* Microfabricated implantable parylene-based wireless passive intraocular pressure sensors. *Journal of Microelectromechanical Systems* **17**, 1342-1351 (2008).

34. Ong KG, Zeng K, Grimes CA. A wireless, passive carbon nanotube-based gas sensor. *IEEE Sensors Journal* **2**, 82-88 (2002).

35. Song S-H, Gillies G, Begley M, *et al.* Inductively coupled microfluidic pressure meter for in vivo monitoring of cerebrospinal fluid shunt function. *Journal of medical engineering & technology* **36**, 156-162 (2012).

36. Shin K-H, Moon C-R, Lee T-H, *et al.* Flexible wireless pressure sensor module. *Sensors and Actuators A: Physical* **123**, 30-35 (2005).

37. Najafi N, Ludomirsky A. Initial animal studies of a wireless, batteryless, MEMS implant for cardiovascular applications. *Biomedical microdevices* **6**, 61-65 (2004).

38. Patterson R. Fundamentals of impedance cardiography. *IEEE Engineering in Medicine and Biology magazine* **8**, 35-38 (1989).

39. Nguyen D, Jin C, Thiagalingam A, *et al.* A review on electrical impedance tomography for pulmonary perfusion imaging. *Physiological measurement* **33**, 695 (2012).

40. Pak D, Rozhkova N, Kireeva M, *et al.* Diagnosis of breast cancer using electrical impedance tomography. *Biomedical Engineering* **46**, 154-157 (2012).

41. Akay M. *Wiley encyclopedia of biomedical engineering*. Wiley-Interscience (2006).

42. Guihan M, Bates-Jenson BM, Chun S, *et al.* Assessing the feasibility of subepidermal moisture to predict erythema and stage 1 pressure ulcers in persons with spinal cord injury: a pilot study. *The journal of spinal cord medicine* **35**, 46-52 (2012).

43. Papp A, Lahtinen T, Härmä M, *et al.* Dielectric measurement in experimental burns: a new tool for burn depth determination? *Plastic and reconstructive surgery* **117**, 889-898 (2006).

44. Pearson S, Colbert AP, McNames J, *et al.* Electrical skin impedance at acupuncture points. *The Journal of Alternative and Complementary Medicine* **13**, 409-418 (2007).

45. Colbert AP, Yun J, Larsen A, *et al.* Skin impedance measurements for acupuncture research: development of a continuous recording system. *Evidence-Based Complementary and Alternative Medicine* **5**, 443-450 (2008).

46. Mayrovitz HN, Davey S, Shapiro E. Local tissue water assessed by tissue dielectric constant: anatomical site and depth dependence in women prior to breast cancer treatment-related surgery. *Clinical physiology and functional imaging* **28**, 337-342 (2008).

47. Mayrovitz HN, Bernal M, Brlit F, *et al.* Biophysical measures of skin tissue water: variations within and among anatomical sites and correlations between measures. *Skin Research and Technology* **19**, 47-54 (2013).

48. Mayrovitz HN, Davey S, Shapiro E. Suitability of single tissue dielectric constant measurements to assess local tissue water in normal and lymphedematous skin. *Clinical physiology and functional imaging* **29**, 123-127 (2009).

49. Huang X, Li S, Schultz JS, *et al.* A dielectric affinity microbiosensor. *Applied Physics Letters* **96**, 033701 (2010).

50. Chen Z, Lu C. Humidity sensors: a review of materials and mechanisms. *Sensor letters* **3**, 274-295 (2005).

51. Bhadra S, Bridges GE, Thomson DJ, *et al.* Wireless Passive Sensor for Remote pH Monitoring. *Journal of Nanotechnology in Engineering and Medicine* **2**, 011011 (2011).

52. Abu-Abed A, Lindquist RG, Choi W-H. Capacitive transduction for liquid crystal-based sensors, Part I: ordered system. *IEEE Sensors Journal* **7**, 1617-1624 (2007).

53. Nopper R, Has R, Reindl L. A wireless sensor readout system—Circuit concept, simulation, and accuracy. *IEEE Transactions on instrumentation and measurement* **60**, 2976-2983 (2011).

54. Sardini E, Serpelloni M. Wireless measurement electronics for passive temperature sensor. *IEEE Transactions on instrumentation and measurement* **61**, 2354-2361 (2012).

55. Grant E. The dielectric method of investigating bound water in biological material: An appraisal of the technique. *Bioelectromagnetics* **3**, 17-24 (1982).

56. Cametti C, Marchetti S, Gambi C, *et al.* Dielectric relaxation spectroscopy of lysozyme aqueous solutions: analysis of the δ-dispersion and the contribution of the hydration water. *The Journal of Physical Chemistry B* **115**, 7144-7153 (2011).

57. Gabriel S, Lau R, Gabriel C. The dielectric properties of biological tissues: II. Measurements in the frequency range 10 Hz to 20 GHz. *Physics in medicine and biology* **41**, 2251 (1996).

58. Huang X, Cheng H, Chen K, *et al.* Epidermal impedance sensing sheets for precision hydration assessment and spatial mapping. *IEEE Transactions on Biomedical Engineering* **60**, 2848-2857 (2013).

59. Virkler K, Lednev IK. Analysis of body fluids for forensic purposes: From laboratory testing to non-destructive rapid confirmatory identification at a crime scene. *Forensci Sci Int* **188**, 1-17 (2009).

60. Guidotti TL, McNamara J, Moses MS. The interpretation of trace element analysis in body fluids. *Indian J Med Res* **128**, 524-532 (2008).

61. Sikirzhytski V, Virkler K, Lednev IK. Discriminant Analysis of Raman Spectra for Body Fluid Identification for Forensic Purposes. *Sensors* **10**, 2869-2884 (2010).

62. Hu S, Loo JA, Wong DT. Human body fluid proteome analysis. *Proteomics* **6**, 6326-6353 (2006).

63. Salvo P, Di Francesco F, Costanzo D, *et al.* A Wearable Sensor for Measuring Sweat Rate. *IEEE Sensors J* **10**, 1557-1558 (2010).

64. Haixia Y, Dachao L, Roberts RC, *et al.* An Interstitial Fluid Transdermal Extraction System for Continuous Glucose Monitoring. *J Microelectromech Syst* **21**, 917-925.

65. Lay-Ekuakille A, Mukhopadhyay S, Coyle S, *et al.* On-Body Chemical Sensors for Monitoring Sweat. In: *Wearable and Autonomous Biomedical Devices and Systems for Smart Environment* (ed^(eds). Springer Berlin Heidelberg.

66. Coyle S, Lau KT, Moyna N, *et al.* BIOTEX—Biosensing Textiles for Personalised Healthcare Management. *IEEE Trans Inf Technol Biomed* **14**, 364-370 (2010).

67. Badugu R, Lakowicz J, Geddes C. A Glucose Sensing Contact Lens: A Non-Invasive Technique for Continuous Physiological Glucose Monitoring. *J Fluoresc* **13**, 371-374 (2003).

68. Badugu R, Lakowicz JR, Geddes CD. Noninvasive Continuous Monitoring of Physiological Glucose Using a Monosaccharide-Sensing Contact Lens. *Anal Chim* **76**, 610-618 (2003).

69. Yu-Te L, Huanfen Y, Lingley A, *et al.* A 3-u CMOS Glucose Sensor for Wireless Contact-Lens Tear Glucose Monitoring. *IEEE J Solid-State Circuits* **47**, 335-344 (2012).

70. Caduff A, Talary MS, Mueller M, *et al.* Non-invasive glucose monitoring in patients with Type 1 diabetes: A Multisensor system combining sensors for dielectric and optical characterisation of skin. *Biosens Bioelectron* **24**, 2778-2784 (2009).

71. Larrañaga MD, Wang Q. Heat Stress. In: *Patty's Toxicology* (ed^(eds). John Wiley & Sons, Inc. (2001).

72. Benelam B, Wyness L. Hydration and health: a review. *Nutrition Bulletin* **35**, 3-25.

73. Mangos JA, McSherry NR. Sodium Transport: Inhibitory Factor in Sweat of Patients with Cystic Fibrosis. *Science* **158**, 135-136 (1967).

74. Suzuki H. Nickel and gold in skin lesions of pierced earlobes with contact dermatitis. A study using scanning electron microscopy and x-ray microanalysis. *Arch Dermatol Res* **290**, 523-527 (1998).

75. Bhadra S, Bridges GE, Thomson DJ, *et al.* Wireless Passive Sensor for Remote pH Monitoring. *J Nanotechnol Eng Med* **2**, 011011-011011 (2011).

76. Fonseca MA, English JM, von Arx M, *et al.* Wireless micromachined ceramic pressure sensor for high-temperature applications. *J Microelectromech Syst* **11**, 337-343 (2002).

77. Harpster TJ, Stark B, Najafi K. A passive wireless integrated humidity sensor. *Sens Actuators A Phys* **95**, 100-107 (2002).

78. Nopper R, Niekrawietz R, Reindl L. Wireless Readout of Passive LC Sensors. *IEEE Trans Instrum Meas* **59**, 2450-2457 (2010).

79. Cametti C, Marchetti S, Gambi CMC, *et al.* Dielectric Relaxation Spectroscopy of Lysozyme Aqueous Solutions: Analysis of the 未-Dispersion and the Contribution of the Hydration Water. *J Phys Chem B* **115**, 7144-7153 (2011).

80. Agache PG, Monneur C, Leveque JL, *et al.* Mechanical properties and Young's modulus of human skin in vivo. *Arch Dermatol Res* **269**, 221-232 (1980).

81. Fries N. *Capillary Transport Processes in Porous Materials: Experiment and Model*. Cuvillier.

82. Sutera SP, Skalak R. The History of Poiseuille's Law. *Annu Rev Fluid Mech* **25**, 1-20 (1993).

83. Takahiro S, Hiroo I, Shigeo F, *et al.* Measurement of the electrical properties of human skin and the variation among subjects with certain skin conditions. *Phys Med Biol* **47**,

N11 (2002).

84. Gabriel C, Gabriel S, Corthout E. The dielectric properties of biological tissues: I. Literature survey. *Phys Med Biol* **41**, 2231 (1996).

85. Sardini E, Serpelloni M. Passive and self-powered autonomous sensors for remote measurements. *Sensors* **9**, 943-960 (2009).

## 2.8 Figures

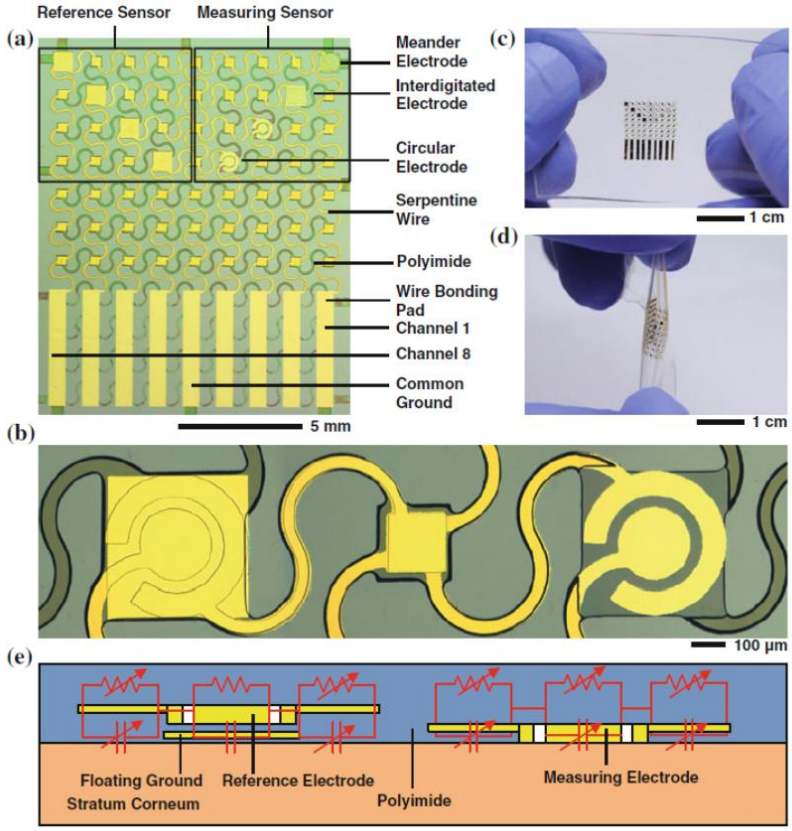


**Figure 2.1 Schematic illustrations and images of a differential hydration sensor platform with epidermal construction.** (a) Optical micrograph showing the electrode layout for a representative device on a silicon wafer just before transfer to a thin, silicone substrate. (b) Optical micrograph of a pair of reference (left) and measuring (right) electrodes, with concentric designs, corresponding to channels 4 and 5 in a. Images of a device during (c) uniaxial stretching and (d) twisting. (e) Schematic illustration and equivalent circuit model (red) of a reference (left) and measuring (right) electrode.

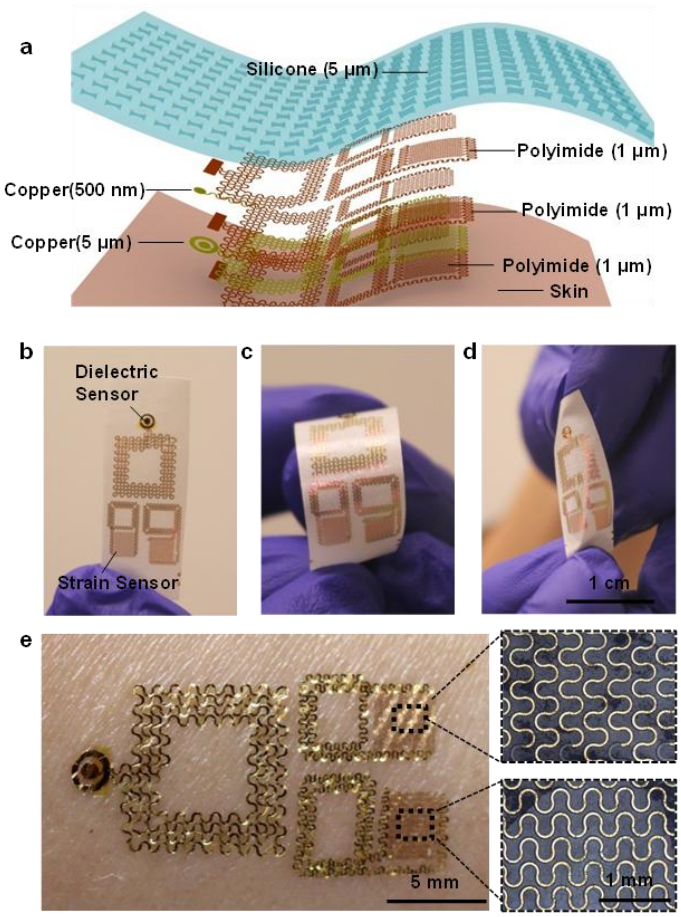


**Figure 2.2 A multimodal wireless epidermal sensor.** (a) Exploded view schematic diagram of the sensor on the skin. Images of a sensor on a water soluble tape in (b) flat, (c) bent, and (d) twisted configurations. (e) Image of a sensor integrated directly on the skin, after removal of the tape.

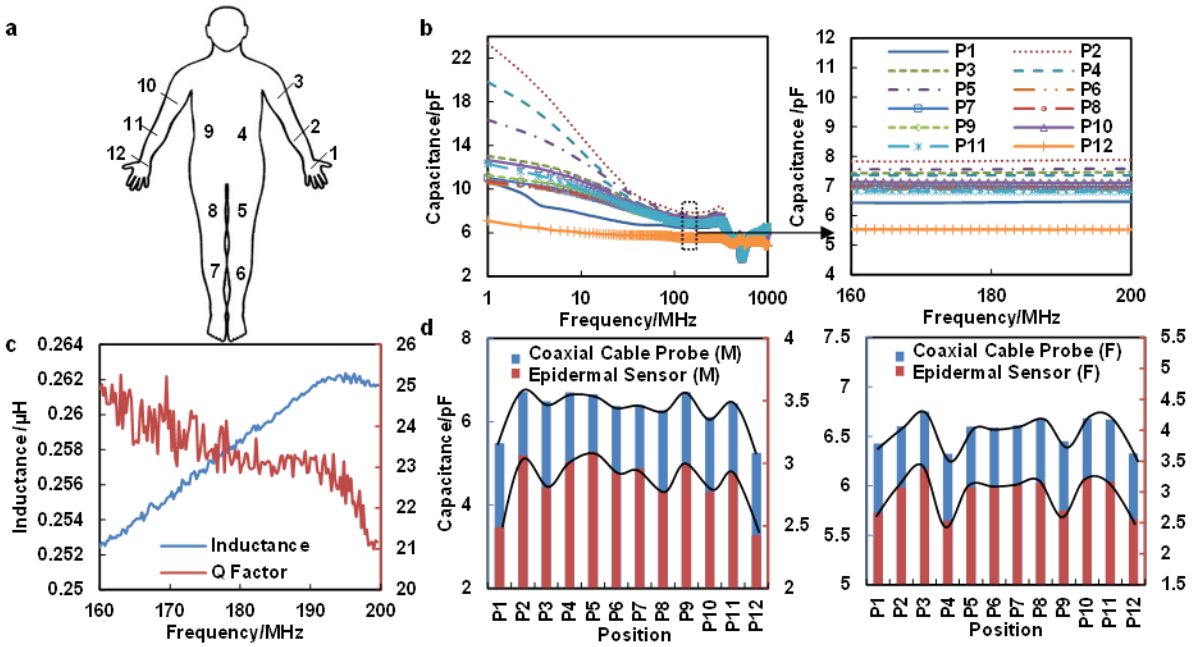


**Figure 2.3** (a) Diagram of 12 different positions for measurements of the skin. (b) Representative variations in dielectric properties of the skin for frequencies between 1 MHz to 1 GHz, evaluated using a coaxial cable probe, at the positions illustrated in (a). Minimal variations occur between 160 MHz to 200 MHz, as shown on the right. (c) Plot of the inductance and Q factor of the epidermal dielectric sensor between 160 MHz to 200 MHz. (d) Comparison of capacitance measured using a wireless sensor and a coaxial cable for two volunteers (M for male; F for Female), at the positions indicated in (a).

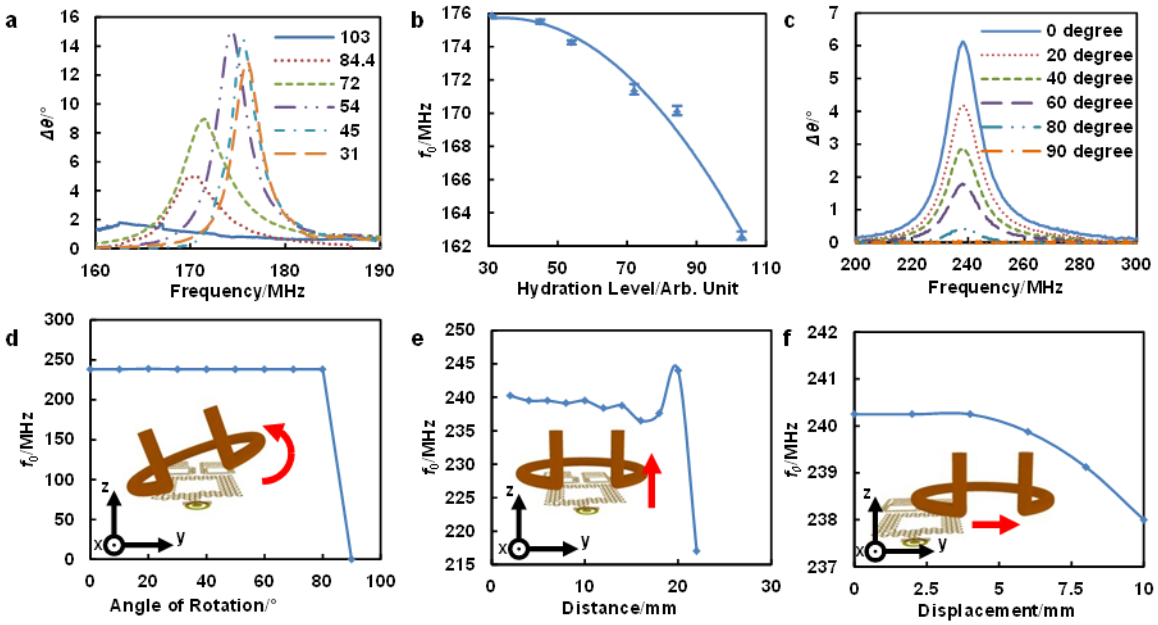


**Figure 2.4** (a) Measurements of the phase response of the primary coil, while in proximity to an epidermal dielectric sensor on the skin, at different levels of hydration. The magnitude of the phase difference changes both with dielectric properties of the skin and the distance between the primary coil to the epidermal sensor. As a result, the magnitude variation in the figure is partly due to the inconsistency of the placement of the measured forearm. (b) Relationship between the minimum phase $f_0$ and hydration levels measured using a commercial hydration sensor. (c) Phase response of the primary coil oriented at different angles relative to the epidermal dielectric sensor. Measured shifts in $f_0$ as the primary coil is displaced (d) rotationally, (e) vertically and (f) horizontally. The assessment of the influence of sensor orientation is conducted on a stretching stage in air. The increased resonance frequency of the sensor (at approximately 240 MHz) is due to the small permittivity of air. The resonance frequency of the sensor shifts back to a value within 160-200 MHz when placed on skin.

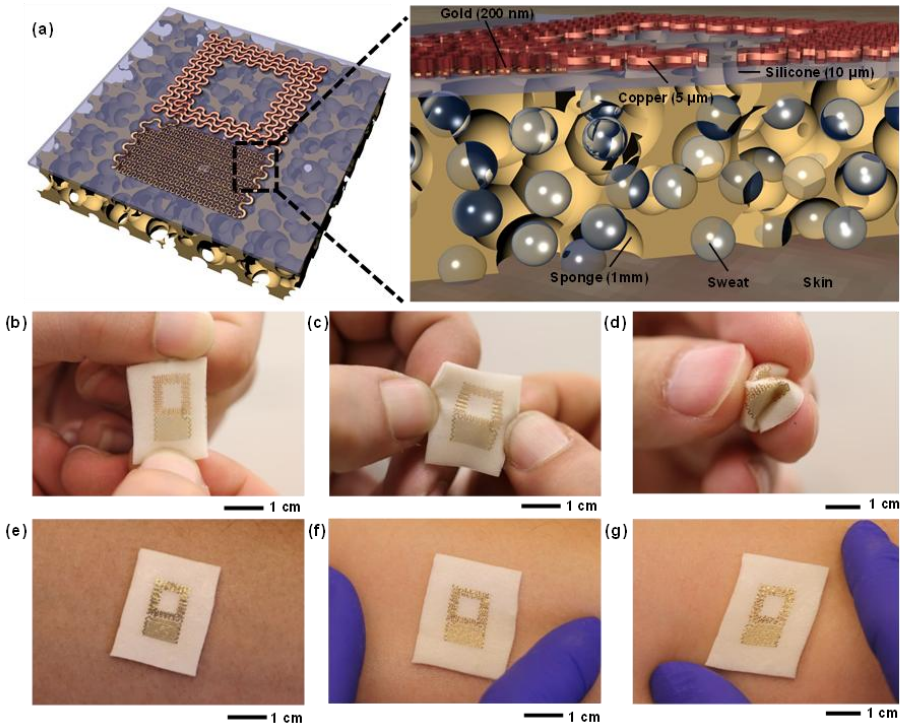


**Figure 2.5** (a) Schematic illustration of a passive wireless capacitive sensor designed for sensing of sweat from the surface of the skin. Pictures of a device in (b) longitudinal and (c) latitudinal states of deformation, and crumpled between the fingers (d). Pictures of a device mounted on the skin in (e) undeformed, (f) uniaxially stretched and (g) biaxially stretched configurations.

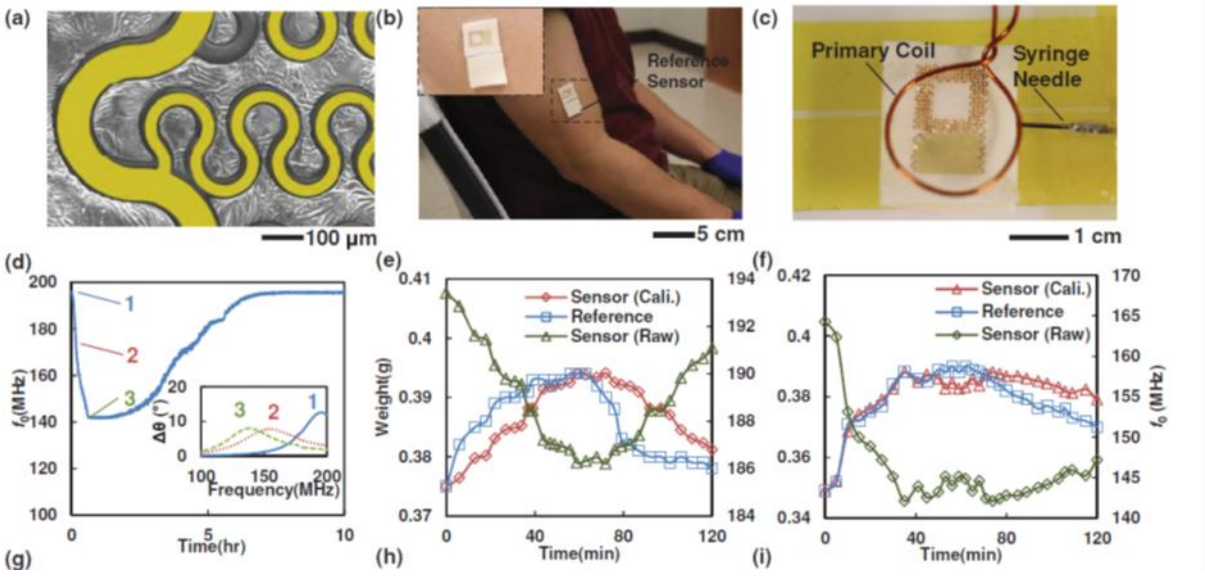


**Figure 2.6** (a) A scanning electron micrograph of a sensor on a PUR substrate coated with a thin silicone film; the regions colorized in yellow represent the interdigitated gold electrodes. (b) Picture of a sweat sensor and a reference sensor on the arm of a volunteer for *in-vivo* testing. (c) Picture of a sweat sensor underneath a primary coil. A syringe needle inserted into the sensor delivers controlled amounts of a buffer solution through a syringe pump for controlled experiments. (d) Representative data showing the response of the sensor (resonant frequency, $f_0$) as a function of time after introduction of 0.6 mL buffer solution (labeled 1). The initial response (labeled 2) corresponds to wicking of the solution into the porous substrate, to yield a stable overall shift in $f_0$ (labeled 3). As the solution evaporates over the next several hours, $f_0$ recovers to approximately the initial value. The inset shows the phase difference measured by the primary coil at the three time points indicated in the main frame. (e, f) Results of testing on two volunteers, with comparisons to changes in weight evaluated using similar porous substrates (without detection coils) placed next to the sensors. Both $f_0$ and the weight of the sensors calibrated from $f_0$ are shown, along with comparison to the weight of the reference substrates.

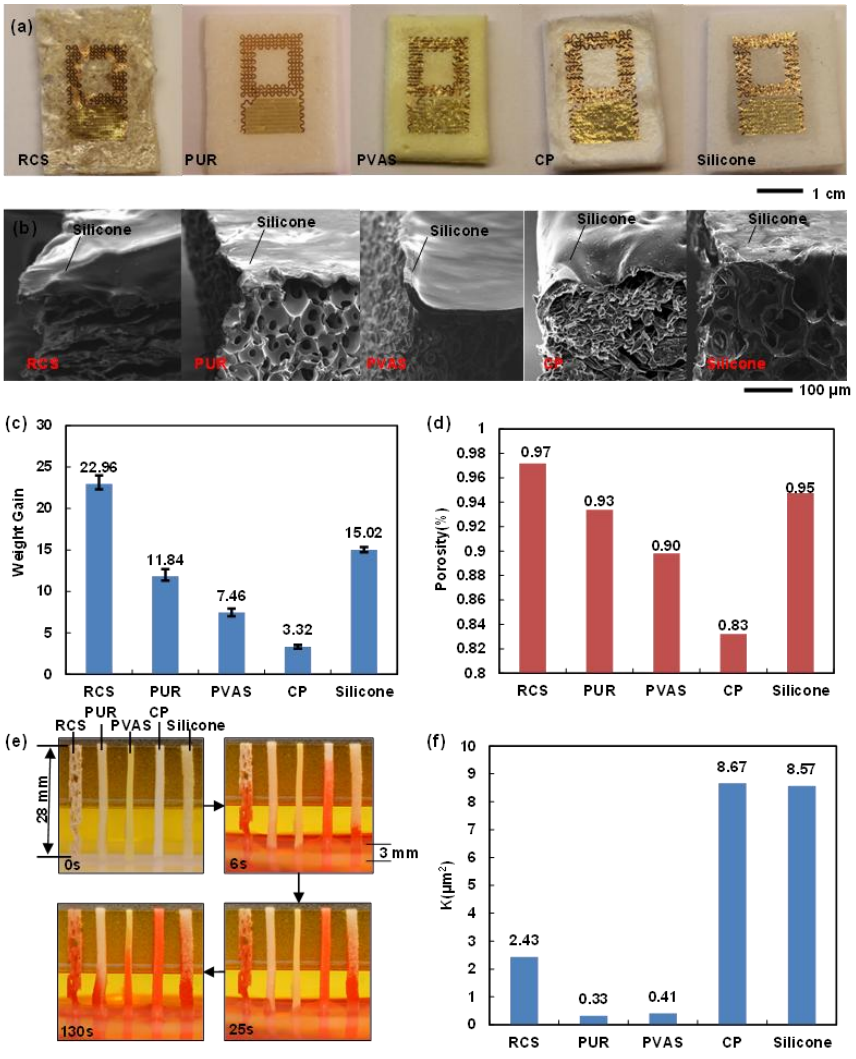


**Figure 2.7** (a) Wireless sweat sensors based on different porous substrates. (b) SEM images of the substrates coated with thin layer of silicone to facilitate chemical bonding between the sensors and the substrates. (c) Weight gain of different substrate materials associated with immersion in water. (d) Porosity of the substrate materials. (e) Images of strips of the substrate materials when partially immersed into water with red dye. (f) Water permeability of the substrate materials.

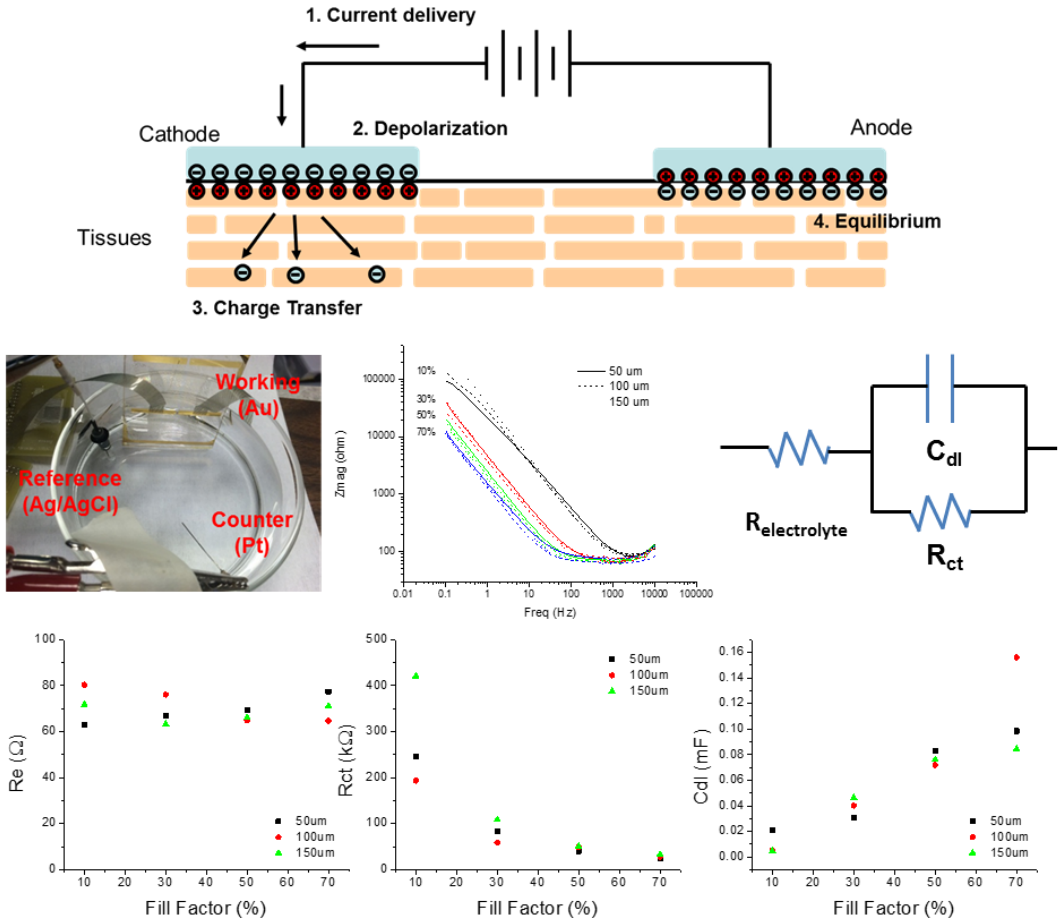


**Figure 2.8 Impedance Spectroscopy test of skin-electrode interface.** (a) Current stimulation mechanism at the skin-electrode interface. (b) Experiment setup for impedance spectroscopy measurement. (c) Impedance spectroscopy of mesh electrodes (22 $mm^2$) with 3 linewidths and 4 fill factors. (d) Randell Cell circuit equivalent model. Extracted values from impedance fitting results of (e) electrolyte resistance, (f) charge-transfer resistance, (g) double-layer capacitance.

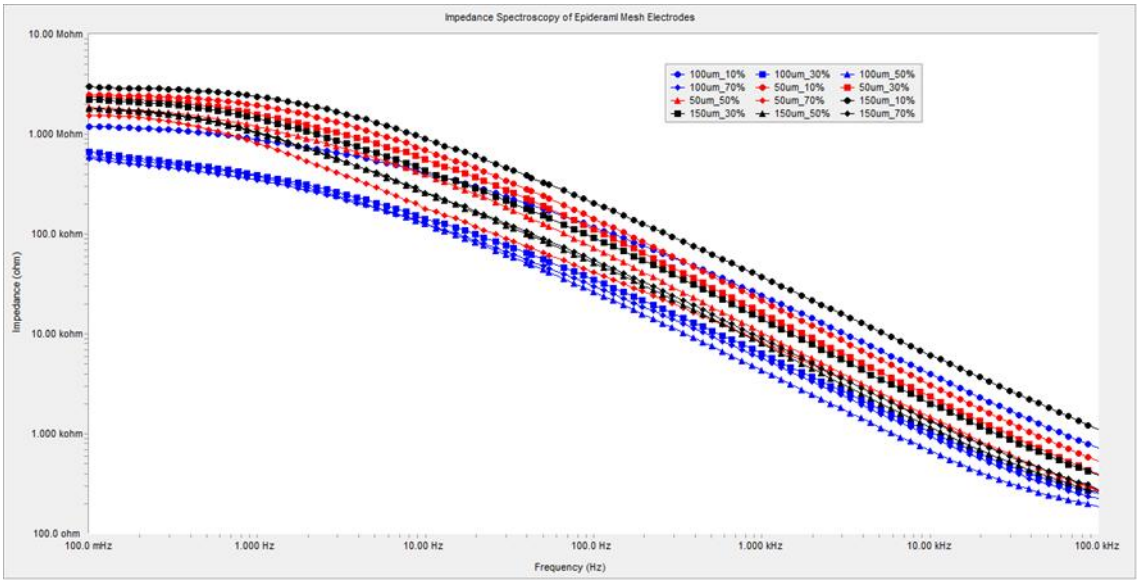


**Figure 2.9 Impedance Spectroscopy of human skin.** Impedance spectroscopy of mesh electrodes (22 $mm^2$) with 3 linewidths and 4 fill factors.

# CHAPTER 3

# EPIDERMAL STIMULATION AND SENSING PLATFORM

Significant portions of this chapter were published as "An Epidermal Stimulation and Sensing Platform for Sensorimotor Prosthetic Control, Management of Lower Back Exertion, and Electrical Muscle Activation," Baoxing Xu[†], Aadeel Akhtar[†], Yuhao Liu[†], Hang Chen, Woon-Hong Yeo, Sung II Park, Brandon Boyce, Hyunjin Kim, Jiwoo Yu, Hsin-Yen Lai, Sungyoung Jung, Yuhao Zhou, Jeonghyun Kim, Seongkyu Cho, Yonggang Huang, Timothy Bretl, John A. Rogers, *Advanced Materials*, 28:22 (2016). Reproduced with permission from the journal. ([†] equal contribution)

## 3.1 Introduction

Skin-mounted sensors of physiological signals are useful in areas ranging from clinical diagnostics to human-machine interfaces[1, 2, 3, 4, 5, 6]. The recent development of concepts in "skin-like" semiconductor technologies, sometimes referred to as epidermal electronics, create important opportunities in long-term, non-invasive, conformal interfaces to the body[7, 8, 9, 10, 11, 12, 13]. These systems offer advantages in device mechanics and user mobility over traditional technologies for healthcare monitoring and disease diagnostics, with demonstrated capabilities in precision measurement of hydration[14], strain[15, 16, 17], pressure[18, 19], temperature[20] and others parameters of interest. Additional recent work shows that similar platforms designed for the fingertips can offer advanced capabilities in electrotactile stimulation[21]. This previous work focused, however, on materials and circuit design aspects of electrotactile stimulation, without any demonstrated application. Combining these functions in a single, simple device platform designed for operation on the trunk or limbs of the body could be attractive in applications such as neuromuscular electrical stimulation[22], neuromodulation rehabilitation therapy[23], pain

mitigation and prevention[24], human-machine interfaces[5], and sensorimotor control in prosthetic and orthotic devices[25], where electromyography (EMG) and electro-stimulation could serve as sensing and actuating platforms. Here, we present systems of this type, where multiple transcutaneous electrical stimulation electrodes co-integrate on a common substrate with sensors for electromyography, temperature and mechanical strain. Abilities for simultaneous recording of physiological data and presentation of neural stimulatory inputs provide valuable functionality, as illustrated in examples of sensorimotor prosthetic control, management of lower back exertion, and electrical muscle activation.

### 3.2 Epidermal Multi-functional Platform

Figure 3.1a provides an optical micrograph of a multifunctional device constructed from patterned metal traces and polymer dielectric materials on a thin layer of silicone elastomer (thickness: 60μm, Young's modulus: ~60KPa, Smooth-on, USA), supported by a temporary, water-soluble substrate of polyvinyl alcohol (PVA, Aicello, Japan). The layout includes electrodes for electrotactile stimulation and measurement of EMG signals, temperature and strain, as in the schematic illustration of Fig. 1b. The fabrication details appear in the supporting information (Supplementary Note 1). The simplicity of the construction represents a key feature of the design. In particular, the active parts of the entire system involve only two layers of metal with patterned interlayer dielectrics; semiconductor materials are not required. The temperature sensor consists of a serpentine conductive trace (Cr/Au) with a width of 20μm, thickness of 200nm and total length of 26mm (~1mm$^2$ total area), in which the temperature dependence of the temperature coefficient of resistance in the Au serpentine traces (2.5 x $10^{-3}$ °C$^{-1}$)[20] provides the basis for the measurement. The EMG sensor uses the same metal, patterned in a different geometry, for reference, measurement and ground electrodes that each consist of 20μm wide

circular concentric rings (2mm width and 12mm length; 24mm$^2$ sensor area) in an interwoven serpentine morphology to allow mechanical stretchability, and with a spacing of ~10mm to optimize signal quality[26]. Each stimulation electrode is coaxial, consisting of an inner disk with a radius of 1.0mm, an outer ring with a radius of 2.0mm, and a 0.5mm space in between. The strain sensor, also constructed in serpentine traces (20μm) with wide radii of curvature (60μm) in the same metal layer, offers uniaxial operation in a multigrid geometry configured in an orientation opposite to that of the temperature sensor, with a width of 20 μm, thickness of 200nm, and total length of 27mm (~1.4mm$^2$ sensor area). This design minimizes the transverse sensitivity of the strain gauge and improves the accuracy of the measurement. A thin film of polyimide (PI, thickness: 1.2μm; Young's modulus ~2.5GPa; Sigma-Aldrich) encapsulates the temperature and strain sensors. The width of the PI patterns is slightly larger, by 50 m on each side, than that of the electrodes, to relax tolerances on registration. The 50 m tolerance associated with the widths of the PI patterns can accommodate any lateral etching associated with the reactive etching process. This layer also places the metal at the neutral mechanical plane, thereby minimizing the effects of bending strain on temperature. The EMG and stimulation electrodes remain exposed to the skin. All sensors connect to peripheral contact pads that allow interfaces to external power supplies and data acquisition hardware. Mounting on the skin involves washing away a water-soluble backing layer of poly(vinyl alcohol) (PVA), using procedures described previously[7]. Figure 3.1c illustrates the way in which the thin, soft construction of the device allows it to conform and adhere to the surface of the skin, based on van der Waals interactions alone. This low modulus mechanics also avoids any significant constraint on natural motions of the skin. Stability of similar types of structures under cyclic strains is excellent [27]. Long-term durability of related types of epidermal devices is demonstrated

with visual and functional evaluation over a two week period of continuous use[28]. These and other previously reported technologies also do not offer the type of multifunctional operation of the devices described here.

### 3.3 Characterization of Sensing and Stimulation Attributes

The stimulation electrodes provide an important functional capability to the epidermal device. Current injected into the skin through these electrodes stimulates sensory nerve fibers to elicit sensations that resemble tingling, vibration, light touch, or pressure[29]. While the contact area of the stimulation electrodes in the epidermal device is much smaller than that of the conventional electrodes, stimulation comfort can be maintained by corresponding settings in the current amplitude and pulse duration. A previous study using conventional hardware reported no discomfort from subjects who received 10 hr/day electrotactile stimulation on the upper arm for 2 weeks[29]. A constant-current monophasic square pulse (3 mA amplitude, 0.2 ms pulse duration, 20 Hz frequency) applied to the skin through electrode 2 using a computer-controlled linear isolated stimulator (STMISOLA, BIOPAC, Inc., CA) yields typical voltage responses, shown in Figure 3.2a, that is similar to that obtained with a conventional gel-based adhesive electrode (Neuroline 710, Ambu A/S, Denmark). The voltage response of a single pulse from the epidermal device is shown in figure 3.2b. The differences in voltage waveforms between the conventional electrodes and our epidermal device are mainly due to the different contact areas they have with the skin. We can model the voltage response across the anode and cathode of the stimulation electrodes and characterize the resistive and capacitive electrical properties of the electrodes by using a circuit model that represents the electrode-skin interface and the underlying tissue[29, 30]. Here, $R_{es}$ and $C_{es}$ are the effective resistance and capacitance, respectively, of the electrode-skin interface. We describe how to compute these values in Supplementary Note 2.

The values of $R_{es}$ and $C_{es}$ depend on the contact areas of the electrodes, their constituent materials, and also the thickness and electrical properties of the skin, and the waveform being sent[29]. Upon stimulating the skin superficial to the left flexor carpi radialis and normalizing to the size of the electrode, we obtain values of 273.5kΩmm$^2$ and 75.13nF/mm$^2$ for $R_{es}$ and $C_{es}$, respectively, for the epidermal device; and 30.79MΩmm$^2$ and 20.84pF/mm$^2$ for the conventional electrodes. Consequently, because the epidermal device has a lower normalized resistance, current can flow more freely through the skin, reducing the occurrence of local high density current areas which can cause painful stimluation[29, 31].

Due to the use of a common, compact device platform, the stimulation electrodes can cause artifacts in the EMG recordings, as shown in figure 3.2c for the case of stimulation (20 Hz, 200 μs positive monophasic square pulse across stimulation channels 1 and 2 with an amplitude of 1.6 mA) on the left flexor carpi radialis muscle of a 21-year old female subject during EMG recording for flexing of the wrist for 2 s, resting for 3 s, and then clenching of the hand for 2 s, each to maximum voluntary contraction (MVC). Figure 3.2d shows the EMG signal collected without electrical stimulation. A digital comb filter can attenuate responses at frequencies at 20 Hz and its harmonics[22], to eliminate the stimulation artifact without significantly altering the EMG data, as illustrated in Figure 3.2c. Additional experiments show that the stimulation frequency, magnitude, number and position of the electrodes do not affect the EMG measurements.

Further study reveals the extent of coupling between the other active components of the device. Constant current stimulation, for example, can potentially lead to Joule heating in the skin, with the possibility of affecting the response of the temperature sensor. Infrared (IR) images (FLIR Systems, Inc., OR) in Figure 3.2e show temperature distributions before and after

maximum stimulation (constant current, just below the pain threshold) for 2 min with the current of 1.54 mA through a single electrode. The changes in temperature are small and localized to the regions immediately adjacent to the simulation electrodes. Even when stimulating through two electrodes, the temperature change remains localized. Design choices also ensure independent operation of the strain and temperature sensors. For example, stretching the device along the x-axis by ~21%, leads to large and readily measurable changes in the response of the strain sensor, but only small changes in the temperature sensor, as shown in figure 3.2f. The mechanics of these structural designs can be captured by finite element analysis (FEA). The temperature change in other regions of the device, for example near the strain sensor, is less than 0.0001 $^{o}$C, which is consistent with the experimental measurements by an IR camera (Figure 3.2e). These temperature distributions indicate that the Joule heating due to stimulation through the electrodes will be localized to the regions of just the stimulation electrodes, and will not affect the measurements of other sensor functions such as strain sensor. The FEA results further confirm that only small amounts of strain appear in the temperature sensor (Supplementary Note 3b). The overall stretchability can therefore accommodate even large deformations associated with bending deformation at the elbows and knees. These small strains indicate successful decoupling of the temperature sensor and strain gauge with respect to the tensile direction, which has excellent agreement with experimental measurements (Figure 3.2f).

### 3.4 Sensorimotor Prosthetic Control

Advanced surgical techniques such as targeted reinnervation provide patients with upper limb amputations the ability to control a prosthetic limb using intuitive muscle commands that map to their missing limb, and to experience sensations perceived as originating from their missing limb[32, 33]. Here, nerves that originally supplied the missing limb are rerouted to intact

muscle and skin elsewhere in the body. Because the reinnervated muscle and skin sites often overlap with or are in close proximity to one another, existing, bulk electrode technologies cannot simultaneously record EMG and electrically stimulate the overlying skin for force and proprioceptive feedback, as a means to reduce the probability of prosthesis abandonment[34, 35]. The devices introduced here, where sensors and actuators can be located closely adjacent to one another, with lithographic precision, create opportunities in this context. A simple demonstration involves devices applied to the right flexor carpi radialis and the extensor carpi radialis muscle groups of a 22-year old male subject. The RMS value of the EMG signal serves as proportional control on the grip aperture of a humanoid robot (Baxter, Rethink Robotics, MA). A sensor (25 lb. Flexiforce, Tekscan, Inc., MA) mounted on the inside of gripper measures the force applied to a plastic bottle filled with water (figure 3.3a). In evaluations, the subject, blindfolded and acoustically shielded, attempts to grip the bottle, both with and without stimulation. With stimulation, the subject receives sensory input at a level proportional to the force measured by the sensor. The maximum stimulation, 2mA, in this case, corresponds to 27N, the maximum force available to the gripper. Figure 3.3b shows that, without feedback, the subject cannot consistently close the gripper without causing the bottle to collapse. With force feedback, the subject can successfully stop the grip at any desired level of gentle touch. Similar capabilities are possible with a wooden block used in place of the bottle.

Stimulation can also provide proprioceptive feedback, as demonstrated in the control of virtual arms presented on a computer screen as well as physical robotic arms. Here, two separate devices mount over the long head of the biceps brachii and the lateral head of the triceps brachii muscles (figure 3.3c). In the virtual arm targeting task, the subject attempts to flex and extend the elbow of a single degree-of-freedom virtual arm to match the orientation of a target virtual arm

presented onscreen[36, 37]. The virtual arm can move between -60° to 60°. During experiments, the subject grips a vertical handle and maintains his elbow in a fixed position at 90° with respect to the humerus to remove any natural proprioceptive cues. Flexing or extending the elbow joint against the handle generates EMG signals (figure 3.3d). Linear discriminant analysis classifies these signals to virtual arm movements every 0.1s, according to previously reported procedures[5, 36]. Evaluations involve four conditions: EMG control with conventional electrodes and no feedback; EMG control with conventional electrodes and stimulation feedback; EMG control with the epidermal device and no feedback; and EMG control with the epidermal device and electrotactile feedback. The feedback activates stimulation with electrodes 1 and 2, that maps, using the tactile funneling illusion[38], the virtual arm angular range (-60° to 60°) to different current levels (figure 3.3e). In the tactile funneling illusion, when two stimulation electrodes are simultaneously active, a single sensation is perceived between the two electrodes. By modulating the stimulation current amplitudes, the location of the perceived sensation can be adjusted to any point between the two electrodes. As a result, any virtual arm angle can be mapped to a unique stimulation location perceived between the two electrodes. In turn, the subject interprets this stimulation location as the joint angle of the virtual arm. A training phase involves free control of the virtual arm for 60s, and then presentation with five target angles to match. After each attempt, the subject presses a button to reveal the actual angle of motion. Performance tests based on 25 random targets appear in figure 3.3f, which shows a schematic illustration of the virtual arm, as well as the errors between the target angle and the subject's estimate for each of the four conditions. Feedback yields statistically significant improvements in performance (Two-Way ANOVA, Tukey post-hoc, $p<0.05$). In particular, the mean absolute errors for conditions without feedback are 37.2° and 31.6° with conventional and epidermal electrodes, respectively. With

feedback, the errors decrease significantly to 17.8° and 16.9° with conventional electrodes and epidermal electrodes, respectively. These performance gains are similar to those found in other studies using sensory substitution (electrotactile, vibrotactile, or skin stretch) for proprioceptive feedback in modulating upper limb joint angles[36, 37, 39]. While the performance with the epidermal electronics offers lower error both with and without feedback compared the conventional electrodes, no statistically significant different was found. Nevertheless, the ability to provide multiple points of stimulation while simultaneously recording EMG in a single device device, as opposed to the multiple sets of conventional electrodes needed to enable sensorimotor control, represents a significant advantage.

### 3.5 Management of Lower Back Exertion

Another application opportunity is in the prevention of excessive muscle exertion due, for example, to improper lifting that can cause chronic lower back pain. Here, a device mounted on the lower back can simultaneously monitor temperature, strain and EMG as indicators of exertion, and provide stimulatory feedback to prevent over-exertion/extension. As a demonstration of functionality relevant in this context, experiments indicate an ability to differentiate stoop motions from squat lifting. A device on the right lumbar paraspinal region (22-year old male**)** records data as the subject performs ten repetitions of four different actions: 1) stooping then standing without lifting a load, 2) stooping then standing while lifting a 25lb load (figures 3.4a,c), 3) squatting then standing without lifting a load, and 4) squatting then standing while lifting a 25lb load (figures 3.4b,d). The mounting location and deformation in three different action states appear in figures 3.4c-e. Figures 3.4f-g summarize the EMG and strain measurements for actions 1 to 4. A notable increase in EMG activity for the loaded compared to the unloaded cases suggests an ability to detect loaded lifting. Stooping motions induce

signature responses of the strain gauge, distinct from those associated with squatting. Placing thresholds on both the EMG and strain data affords an ability to detect stoop lifting and to trigger an electrotactile stimulation alert signal.

Muscle exertion can also be measured. Although both EMG and temperature can serve as indicators of muscle fatigue, literature suggests that EMG is a poor indicator of lower back muscle fatigue due to unstable motor unit recruitment in this region[40, 41]. In this circumstance, the temperature sensor provides a reliable indicator of muscle exertion, associated with increases in metabolic reactions and blood flow that lead to corresponding increases in skin temperature. To test this capability, a subject lying prone on a table flexes his back until exhaustion while holding a 25lb weight at his chest. Figure 3.4h shows that although the EMG signals from the lower back remain unchanged, the temperature clearly increases with time. This temperature response therefore provides additional functionality in the context of monitoring muscle fatigue. Together with the EMG sensor, the strain gauge and electrotactile stimulators, this platform offers important functionality in this context of intervention for lower back exertion.

## 3.6 Electrical Muscle Activation

The stimulation electrodes can provide not only sensory input, but they can also, when operated at increased current levels, induce muscle contractions, of relevance to reanimating paralyzed limbs, evaluating neuromuscular function or training for strength in athletes[42]. Figure 3.5a shows a modified device that incorporates larger muscle stimulation electrodes mounted over the long head of the subject's biceps brachii muscle. These electrodes adopt serpentine structures similar to those use for electrotactile stimulation, but they cover larger areas to allow stimulation of multiple motor units to elicit muscle contractions. As in the case of the electrotactile stimulation electrodes, these serpentine designs allow for large-strain deformation,

which is critically important in avoiding constraints or interface stresses associated with motion. In this device, an EMG sensor lies between the stimulation electrodes for monitoring in experiments that involve bicep muscle contractions in a 22-year old male subject induced by applying a positive, monophasic, constant voltage square pulse through a computer-controlled linear isolated stimulator (STMISOLA, BIOPAC, Inc., CA). Incrementally increasing the amplitude of the voltage identifies the threshold for inducing muscle twitch. Figure 3.5b shows the resulting neuromuscular voltage response, known as the M-Wave, from 1Hz stimulation at 50V recorded from the EMG sensor. Figure 3.5c shows one period of a representative M-wave at 50V, 30V and 10V. Reducing the voltage decreases the amplitude of the muscle contraction, leading to a reduction in the M-wave amplitude, and vice versa. The amplitude of the M-wave can be used to modulate the stimulation voltage to produce a desired contraction level. As a test of the ability to recover voluntary EMG during electrical muscle stimulation using the device, the subject attempts to contract his biceps during application of 1Hz stimulation at 50V. Other studies achieve similar results[22], but only with large bulky electrodes for stimulation and recording, as opposed to the compact, thin, conformal profile of the devices introduced here. Additionally, we measured the temperature of the skin using the same device to detect muscle fatigue induced by long-term electrical muscle stimulation. Figure 3.5d shows that the temperature increases quickly with the onset of stimulation and then becomes constant due to the heat transfer with air as the muscle fatigues. The temperature provides an important index of stimulation-induced muscle fatigue, similar to fatigue detection on the forearm and the upper arm, and will be important in modulating input voltages during long-term usage of electrical muscle stimulation. Consequently, the device is able to use both M-wave and muscle fatigue information to enable fine control of muscle contractions in electrical muscle stimulation applications.

## 3.7 Conclusions

In conclusion, the conformal, multifunctional, epidermal device reported here seamlessly integrates sensors for electromyography, temperature, and strain with electrical stimulation electrodes, in a simple architecture that incorporates only metal traces and dielectric layers. Demonstrated application possibilities include prosthetic control with sensory feedback, monitors and stimulation signals related to lower back exertion, and electrical muscle stimulation with feedback control. Future work will investigate long-term application in clinical settings, with a focus on patients with upper limb amputations to simultaneously control and feel from their prosthetic device, and accelerating rehabilitation for stroke patients through the use of electrical muscle stimulation to reanimate paralyzed limbs. In such cases, means for accommodating variations in stimulation parameters that occur with changes in the impedance of the electrode-skin interface over time will be important[43]. All such applications can exploit emerging capabilities in wireless power transfer and control in skin-like formats[2, 7, 44].

## 3.8 Methods

**Device fabrication.** The fabrication (details in **Supplementary Note S1**) began with spin-coating a sacrificial layer of poly(methylmethacrylate) (PMMA, 100 nm, MicroChem) onto a silicon wafer, followed by a layer of polyimide (PI, 1.2um, SigmaAldrich). Sputter deposition then formed a bilayer of chromium/gold (Cr/Au, 5nm/200 nm). Photolithography, wet-etching and oxygen reactive ion etching steps defined patterns for the temperature, strain, and EMG sensors as well as the electrical muscle and electrotactile stimulation anodes. A second PI film was then coated and patterned as an insulating layer for additional bilayer of metal (Cr/Au, 7nm/300 nm). Similar photolithography, wet-etching and oxygen reactive ion-etching steps defined the stimulation cathodes. A third patterned layer of PI served to encapsulate the

interconnects, the temperature and strain sensors, and the contacts. Dissolution of the PMMA allowed the entire device to be retrieved onto a water-soluble tape (3M). Electron beam evaporation of a bilayer of chromium/silica ($Cr/SiO_2$, 5nm/60nm) formed an exposed oxide for bonding to the surface of a thin film (~0.5 mm) of silicone (Ecoflex, Smooth-on Inc.) pre-treated by exposure to ozone induced by ultraviolet light and coated on a substrate of polyvinyl alcohol (PVA, Aicello, Toyohashi). Anisotropic conductive films (Elform) served as flexible electrical cable connections to contact pads on the device, for data acquisition and power supply.

**EMG signals measurement.** The EMG signals were recorded using a 16-channel EMG acquisition system (DelSys, Inc., MA) and amplified and band-pass filtered through an SA Instrumentation Isolated Bioamplifier (James Long, NY) along with a National Instruments DAQ. When measuring EMG, the middle EMG port on the epidermal device served as a ground electrode for obtaining a high quality signal. The other two ports provided interfaces for the differential recording electrode pair. The gain of the amplifier was set to 1000. Specially designed MATLAB codes allowed removal of stimulation artifacts from the EMG signal.

**Strain measurement.** A 4-channel National Instruments Digital Multimeter was used to record the electrical resistance. The initial resistance, $R_0$, of the strain sensor was measured on the unstrained device mounted on the skin. Upon application of strain, the resistance, $R$, was recorded as a function of time. From the resistance, the strain could be computed, according to $\varepsilon = |R - R_0| / R_0 / G$, where $G$ is the gauge factor (~2.6 for the cases examined here). The effects of changes in temperature on the relative resistance during deformation were negligible, as shown in Figure 3.2.

**Temperature measurement.** The same system for measuring strain can be used to measure temperature. The change in temperature can be extracted from the difference between the measured resistance, $R$ , and the initial resistance, $R_0$ at the initial temperature $T_0$, according to $\Delta T = T - T_0 = \alpha |R - R_0|$, where $\alpha$ is the thermal coefficient (0.25K/Ω for the cases examined here). The temperature data acquisition involves a National Instrument PXI-6289 board with custom software interface. The 16 bit A/D converter provides a resolution of 0.02℃ at a sampling frequency of 66.67 Hz. The standard deviation of the temperature measurement over a period of 150 s is 0.021 ℃ for the sensor on skin[20].

**Current and voltage stimulation.** Electrical signals for stimulation were provided by a computer-controlled National Instruments digital to analog converter (NI-myDAQ) interfaced to an isolated linear stimulator (BIOPAC System, Inc. CA). The current or voltage stimulation waveforms were adjustable using specially designed software in MATLAB. Forearm, biceps, triceps and lower back muscles were all successfully stimulated using this system.

## 3.9 Supplementary Information

### Supplementary Note 3.1: Fabrication procedure for epidermal devices

**Deposition of 1st layer Chrome/Gold**

1. Clean silicon wafer
2. Treat silicon wafer surface with Ultra-violet/ozone(UV-O) for 3mins
3. Spin coat PMMA (A2, 495)(2000rpm, 30s)
4. Anneal at 180℃ for 3-4min
5. Spin coat PI(4000 rpm, 30s)

6. Anneal at 150℃ for 5min
7. Anneal at 250℃ under vacuum for1 hr
8. Deposit 1st layer Cr(5nm)/Au(200nm) with electron beam evaporator

**1st mask (mask#1 Au) for temperature, strain and EMG sensors**

9. Spin coat PR AZ5214 (3000rpm, 30s)
10. Anneal at 110℃ for 1-2min
11. Align mask#1 and expose with Karl Suss MJB3
12. Develop in developer AZ917
13. Anneal at 110℃ for 3-4min
14. Etch Au with TFA Au etchant
15. Etch Cr with CR-7 Cr Mask Etchant
16. Remove PR with acetone/IPA/DI water

**2nd mask (mask#2 vias) for PI insulation layer:**

17. Spin coat PI(2000rpm, 30s)
18. Anneal at 150℃ for 5min
19. Anneal at 250℃ under vacuum for 1 hr
20. Spin coat PR AZ4620(2500rpm, 30s)
21. Anneal at 110℃ for 3min
22. Align via mask#2 and expose with Karl Suss MJB3
23. Develop in developer AZ400K diluted with water 1:3
24. Etch exposed PI with March RIE.
25. Remove PR with acetone/IPA/DI water

**3rd mask (mask #3 Au) for electrodes**

26. Deposit Cr (8 nm)/Au (300 nm) with Sputter

27. Spin coat PR AZ5214 (3000rpm, 30sec)

28. Anneal at 110℃ for 1-2min

29. Align mask#3 and expose with Karl Suss MJB3

30. Develop in developer AZ917

31. Anneal at 110℃ for 3min

32. Etch Au with TFA Au etchant

33. Etch Cr with CR-7 Cr Mask Etchant

34. Etch exposed PI with March RIE

35. Remove PR with acetone/IPA/DI water

**4th mask (mask #4 PI) for the cover of strain and temperature sensors and connector wires and pads**

36. Spin coat PI(4000rpm, 30s)

37. Anneal at 150℃ for 5min

38. Anneal at 250℃ under vacuum for1 hr

39. Spin coat PR AZ4620(2500rpm, 30s)

40. Anneal at 110℃ for 3min

41. Align via mask#4 and expose with Karl Suss MJB3

42. Develop in developer AZ400K diluted with water 1:3

43. Etch exposed PI with March RIE

44. Remove PR with acetone/IPA/DI water

**Pickup using water-soluble tap**

45. Lift up device with acetone

46. Pick up device with water-soluble tape
47. Deposit Cr (5nm) and SiO2 (60nm) with electron beam evaporator

**Transfer onto Ecoflex/PVA substrate**

48. Prepare Ecoflex/PVA substrate on glass wafer (coat PVA film onto glass wafer; spin coat Ecoflex (Part B:PartA, 2:1) (3000rpm, 120s); curl for one day at room temperature)
49. Prebake glass wafer with PVA and Ecoflex substrate
50. Treat Ecoflex/PVA substrate with Ultra-violet/ozone(UV-O) for 3min
51. Transfer device from water-soluble tape to Ecoflex/PVA substrate
52. Wash away water-soluble tape
53. Connect the ACF cable

**Supplementary Note 3.2: Circuit model and analysis of electrode on the skin**

The contact between electrode and skin can be described as a resistor and a capacitor in parallel. Supplementary Fig. S3a shows the equivalent circuit model, where $R_{es}$ and $C_{es}$ are the effective resistance and capacitance of the electrode-skin interface, respectively. When a constant current is supplied, a typical resistor–capacitor voltage step response curve is measured using both conventional electrodes and the epidermal device. Here, we take the charging phase for analysis[1,2]. Using the equation for capacitive charging, we can estimate the steady-state voltage, RC time constant, and the DC offset.

$$V(t) = (V_s - V_o) \times (1 - \exp^{-\frac{x}{\tau}}) + V_o$$

Where $V_s$ is the steady-state voltage, $V_o$ is the DC offset and $\tau$ is the time constant for charging phase. The resistive part of the impedance can be computed by taking the steady-state voltage

($V_s$), subtracting it from the DC offset ($V_0$), and then dividing it by the stimulation current amplitude[1,2]. To account for the different sizes of electrodes, the resistance is normalized by multiplying the area of the electrode[1]:

$$R_{norm} = \frac{V_s - V_0}{I} \times area_{electrode}$$

The capacitive part can then be computed by dividing the resistance value from the estimate of $\tau$. To account for the different sizes of the electrodes, the capacitance is normalized by dividing by the area of the anode[1]:

$$C_{norm} = \frac{\tau}{R} \times \frac{1}{area_{electrode}}$$

The area of the conventional electrode was 263mm$^2$ and the area of the epidermal stimulation electrode was 3.14mm$^2$.

**Supplementary Note 3.3a: Joule heat generation from current stimulation**

Supplementary Figure S4a shows the global IR camera images of the device onto the arm before and after 2-minute simulation with the current amplitude of 1.54 mA through one electrode. Even when the current stimulation is activated by two electrodes, the temperature rising is also localized in the contact areas between electrodes and skin, as shown in Supplementary Figure S4b. Finite element analysis (FEA) is used to study the temperature increase in the device due to the joule heating. The device, which is modeled by the heat transfer shell elements (DS4,

ABAQUS[3]), with the substrate (Ecoflex, ~30um in thickness, thermal conductivity ~0.16 W/mK, modeled by the heat transfer brick elements (DC3D8, ABAQUS[1])) is mounted, and therefore in direct contact with, the skin tissues. Their thickness and thermal properties are given in Supplementary Table 3.1. The temperature at the bottle of the muscle layer has a constant body temperature 37 $^{o}$C due to heating of the blood. The upper surface of the substrate has natural convection with air, where the convective heat transfer coefficient is 13 W/m$^2$K.[4] The room temperature is taken from Supplementary Figure S4a as 21 $^{o}$C. The temperature of the substrate surface exposure to air is 30 $^{o}$C with none electrodes activated, which is consistent with the experiment as show in Supplementary Figure S4b. The power for each electrode is calculated by $P=\eta UI$, where $U$ and $I$ are the stimulation current and the measured voltage respectively, and $\eta$ is the ratio of current pulse time to its period. Supplementary Figure S4c shows the temperature distribution in the whole device at steady state; where only left half of the device is shown as two symmetrical electrodes are activated. The bottom left magnified view shows the temperature in the electrode; the average increase is ~0.002 $^{o}$C. The bottom right magnified view shows temperature in the strain sensor; its temperature change is less than 0.0001 $^{o}$C, which is consistent with the experiments that no temperature change is captured by global IR camera images, and confirms that the Joule heating due to stimulation will not affect the strain measurement.

**Supplementary Table 3.1: The thickness and thermal properties of various tissues under the device.**

| Parameters | Skin | Fat | Muscle |
|---|---|---|---|
| **Desity ($kg/m^3$)** [5-8] | 1085 | 850 | 1085 |
| **Specific heat capacity (J/kg K)** [5-8] | 3680 | 2300 | 3768 |
| **Thermal conductivity (J/m K)** [5-8] | 0.47 | 0.16 | 0.42 |
| **Thickness (mm)** [7-10] | 1.0 | 4.4 | 13.6 |

**Supplementary Note 3.3b: FEA analysis on mechanical deformation**

FEA is also carried out to study the effects of mechanical deformation of this stretchable device on both the temperature and EMG measurements. The silicone elastomer (Ecoflex, ~30 μm in thickness, with modulus ~60 kPa) is modeled by the hexahedron element (C3D8R, ABAQUS[1]), while the device is modeled by the composite shell element (S4R, ABAQUS[1]). Supplementary Figure S5a shows the strain distribution in the Au layer of the device under 21% stretch, where the maximum strain occurs at the joint of the electrode to wires and is less than 0.3% (yield strain of gold), which indicates that the device can sustain larger, cyclic stretch without plastic deformation. The normal strain distributions in the horizontal (x) and vertical (y) directions in the temperature sensor are shown in Supplementary Figure S5b. For the average normal strain (-0.07%) in y direction, the average change in the electrical resistance of the temperature sensor is equivalent to that for -0.09 $^{o}$C temperature change, which is much smaller than that due to muscle reaction during subsequent experiments (~2 $^{o}$C). Due to the Poisson's effect (vertical contraction for horizontal stretch) of the substrate, the EMG buckles into sinusoidal deformation in the out-of-plane direction to minimize the strains, as show in Supplementary Figure S5c. The

maximum strain in the EMG is as small as 0.09% due to its meshed serpentine structure, which indicates a negligible effect of mechanical deformation on EMG measurements.

**Supplementary Note 3.4a: Robot teleoperation-gripping water bottle**

One of humanoid robot hands (Baxter, Rethink Robotics)) is to mimic a virtual hand. The object to be gripped is a plastic bottle with water and the water is helpful to monitor deformation of bottle. A very thin force sensor is attached inside of robot hand gripper to extract the gripping force of gripper applied to the bottle through a computer. Epidermal device was mounted on the forearm of the subject volunteer (male, 23years old), and the subject was asked to flex his forearm with elbow on the table.

**Supplementary Note 3.4b: Fatigue test on arm muscle groups**

The epidermal device was mounted on the skin of arm of a subject volunteer (male, 23years old). He was asked to hold a 20lb weight in hand as long as he could. The EMG and temperature measurements were carried out to simultaneously record the data for analysis. The EMG amplitude shows an obvious decrease while the temperature shows an obvious increase as a function of measurement time.

**Supplementary Note 3.5: Robot teleoperation-Rotation of elbow**

Two epidermal devices were attached on the upper arm of the subject volunteer (male, 23years old). One was on biceps and the other was on triceps. Two electrodes on the biceps epidermal device were chosen to send current stimulation. The subject was asked to place his forearm in parallel with the table and the hand was held tightly on a supporter. When he try to lift the

support up, the biceps was activated, generating EMG signals. When he compressed the support down, the triceps was activated, generating EMG signals as well. He was asked to lift up and compress down the support back and forth, EMG signals were generated alternatively, driving the virtual elbow rotation. The subject was trained before test, referred to as offline training process, and was asked to get the knowledge of one-to-one correspondence between stimulation sensation (position and intensity) and elbow position. In the practical test, referred to as online process, the subject would try to match positions of the virtual arm based on his training experience (guess) and the given-target. The conventional electrodes and stimulation pads were mounted on the biceps and triceps to perform the test separately for comparison.

**Supplementary Note 3.6: Fatigue test on low back muscle**

A volunteer (male, 23years old) was first asked to lay on his stomach on a table with the epidermal device mounted on the skin of low back. He was then asked to hold a 20lb weight in the hands, and the volunteer was first flex his back with angle of $26^{o}$ to the table (i.e. ground). The EMG and temperature measurements were performed to simultaneously record the data for analysis. The EMG barely shows any change, but the temperature behaves an obvious increase.

## 3.10 References


1. Ramanathan C, Ghanem RN, Jia P, *et al.* Noninvasive electrocardiographic imaging for cardiac electrophysiology and arrhythmia. *Nat Med* **10**, 422-428 (2004).

2. Xu S, Zhang Y, Jia L, *et al.* Soft Microfluidic Assemblies of Sensors, Circuits, and Radios for the Skin. *Science* **344**, 70-74 (2014).

3. Budinger TF. Biomonitoring with wireless communications. *Ann Rev Biomed Eng* **5**, 383-412 (2003).

4. Tee BCK, Wang C, Allen R, *et al.* An electrically and mechanically self-healing

composite with pressure- and flexion-sensitive properties for electronic skin applications. *Nat Nano* **7**, 825-832 (2012).

5. Jeong J-W, Yeo W-H, Akhtar A, *et al.* Materials and Optimized Designs for Human-Machine Interfaces Via Epidermal Electronics. *Adv Mater* **25**, 6839-6846 (2013).

6. Asghari Oskoei M, Hu H. Myoelectric control systems—A survey. *Biomed Sign Proc Control* **2**, 275-294 (2007).

7. Kim D-H, Lu N, Ma R, *et al.* Epidermal Electronics. *Science* **333**, 838-843 (2011).

8. Kim D-H, Lu N, Ghaffari R, *et al.* Materials for multifunctional balloon catheters with capabilities in cardiac electrophysiological mapping and ablation therapy. *Nat Mater* **10**, 316-323 (2011).

9. Kim D-H, Ghaffari R, Lu N, *et al.* Electronic sensor and actuator webs for large-area complex geometry cardiac mapping and therapy. *Proc Natl Acad Sci* **109**, 19910-19915 (2012).

10. Ramuz M, Tee BCK, Tok JBH, *et al.* Transparent, Optical, Pressure-Sensitive Artificial Skin for Large-Area Stretchable Electronics. *Adv Mater* **24**, 3223-3227 (2012).

11. Son D, Lee J, Qiao S, *et al.* Multifunctional wearable devices for diagnosis and therapy of movement disorders. *Nat Nano* **9**, 397-404 (2014).

12. Jeong GS, Baek D-H, Jung HC, *et al.* Solderable and electroplatable flexible electronic circuit on a porous stretchable elastomer. *Nat Commun* **3**, 977 (2012).

13. Kaltenbrunner M, Sekitani T, Reeder J, *et al.* An ultra-lightweight design for imperceptible plastic electronics. *Nature* **499**, 458-463 (2013).

14. Huang X, Liu Y, Cheng H, *et al.* Materials and Designs for Wireless Epidermal Sensors of Hydration and Strain. *Adv Funct Mater* **24**, 3846-3854 (2014).

15. Pang C, Lee G-Y, Kim T-i, *et al.* A flexible and highly sensitive strain-gauge sensor using reversible interlocking of nanofibres. *Nat Mater* **11**, 795-801 (2012).

16. Yamada T, Hayamizu Y, Yamamoto Y, *et al.* A stretchable carbon nanotube strain sensor for human-motion detection. *Nat Nano* **6**, 296-301 (2011).

17. Lu N, Lu C, Yang S, *et al.* Highly Sensitive Skin-Mountable Strain Gauges Based Entirely on Elastomers. *Adv Funct Mater* **22**, 4044-4050 (2012).

18. Wang C, Hwang D, Yu Z, *et al.* User-interactive electronic skin for instantaneous pressure visualization. *Nat Mater* **12**, 899-904 (2013).

19. Lipomi DJ, Vosgueritchian M, Tee BCK, *et al.* Skin-like pressure and strain sensors based on transparent elastic films of carbon nanotubes. *Nat Nano* **6**, 788-792 (2011).

20. Webb RC, Bonifas AP, Behnaz A, *et al.* Ultrathin conformal devices for precise and continuous thermal characterization of human skin. *Nat Mater* **12**, 938-944 (2013).

21. Ying M, Bonifas AP, Lu N, *et al.* Silicon nanomembranes for fingertip electronics. *Nanotechnology* **23**, 344004 (2012).

22. Frigo C, Ferrarin M, Frasson W, *et al.* EMG signals detection and processing for on-line control of functional electrical stimulation. *J Electromyogr Kines* **10**, 351-360 (2000).

23. Gerasimenko Y, Gorodnichev R, Moshonkina T, *et al.* Transcutaneous electrical spinal-cord stimulation in humans. *Ann Phys Rehabil Med* **52**, 53-62 (1989).

24. John D. Loeser, Richard G. Black, Amalia Christman. Relief of pain by transcutaneous stimulation. *J Neurosurgery* **42**, 308-314 (1975).

25. Antfolk C, D'Alonzo M, Rosén B, *et al.* Sensory feedback in upper limb prosthetics. *Expert Rev Med Dev* **10**, 45-54 (2013).

26. Young AJ, Hargrove LJ, Kuiken TA. The Effects of Electrode Size and Orientation on the Sensitivity of Myoelectric Pattern Recognition Systems to Electrode Shift. *IEEE Trans Biomed Eng* **58**, 2537-2544 (2011).

27. Dagdeviren C, Yang BD, Su Y, *et al.* Conformal piezoelectric energy harvesting and storage from motions of the heart, lung, and diaphragm. *Proc Natl Acad Sci* **111**, 1927-1932 (2014).

28. Yeo W-H, Kim Y-S, Lee J, *et al.* Multifunctional Epidermal Electronics Printed Directly Onto the Skin. *Adv Mater* **25**, 2773-2778 (2013).

29. Kaczmarek KA, Webster JG, Bach-y-Rita P, *et al.* Electrotactile and vibrotactile displays for sensory substitution systems. *IEEE Trans Biomed Eng* **38**, 1-16 (1991).

30. Long-Fei W, Jing-Quan L, Bin Y, *et al.* PDMS-Based Low Cost Flexible Dry Electrode for Long-Term EEG Measurement. *IEEE Sens J* **12**, 2898-2904 (2012).

31. Keller T, Kuhn A. Electrodes for transcutaneous (surface) electrical stimulation. *J Automat Contr* **18**, 35-45 (2008).

32. Kuiken TA, Li G, Lock BA, *et al.* Targeted Muscle Reinnervation for Real-Time Myoelectric Control of Multifunction Artificial Arms. *JAMA J Am Med Ass* **301**, 619-628 (2009).

33. Kuiken TA, Marasco PD, Lock BA, *et al.* Redirection of cutaneous sensation from the

hand to the chest skin of human amputees with targeted reinnervation. *Proc Natl Acad Sci* **104**, 20061-20066 (2007).

34. Atkins DJ, Heard DCY, Donovan WH. Epidemiologic overview of individuals with upper-limb loss and their reported research priorities. *JPO: J Prosth Orth* **8**, 2-11 (1996).

35. Peerdeman B, Boere D, Witteveen H, *et al.* Myoelectric forearm prostheses: state of the art from a user-centered perspective. *J Rehabil Res Dev* **48**, 719-738 (2011).

36. Akhtar A, Nguyen M, Wan L, *et al.* Passive Mechanical Skin Stretch for Multiple Degree-of-Freedom Proprioception in a Hand Prosthesis. In: *Haptics: Neuroscience, Devices, Modeling, and Applications* (ed^(eds Auvray M, Duriez C). Springer Berlin Heidelberg (2014).

37. Wheeler J, Bark K, Savall J, *et al.* Investigation of Rotational Skin Stretch for Proprioceptive Feedback With Application to Myoelectric Systems. *IEEE Trans Neural Syst Rehab Eng* **18**, 58-66 (2010).

38. Nohama P, Lopes AV, Cliquet A. Electrotactile Stimulator for Artificial Proprioception. *Artif Organs* **19**, 225-230 (1995).

39. Witteveen HJB, Droog EA, Rietman JS, *et al.* Vibro- and Electrotactile User Feedback on Hand Opening for Myoelectric Forearm Prostheses. *IEEE Trans Biomed Eng* **59**, 2219-2226 (2012).

40. Farina D, Gazzoni M, Merletti R. Assessment of low back muscle fatigue by surface EMG signal analysis: methodological aspects. *J Electromyogr Kines* **13**, 319-332 (2003).

41. Yoshitake Y, Ue H, Miyazaki M, *et al.* Assessment of lower-back muscle fatigue using electromyography, mechanomyography, and near-infrared spectroscopy. *Eur J Appl Physiol* **84**, 174-179 (2001).

42. Maffiuletti N, Minetto M, Farina D, *et al.* Electrical stimulation for neuromuscular testing and training: state-of-the art and unresolved issues. *Eur J Appl Physiol* **111**, 2391-2397 (2011).

43. Akhtar A, Boyce B, Bretl T. The relationship between energy, phase charge, impedance, and perceived sensation in electrotactile stimulation. (2014).

44. Huang X, Liu Y, Chen K, *et al.* Stretchable, Wireless Sensors and Functional Substrates for Epidermal Characterization of Sweat. *Small* **10**, 3083-3090 (2014).

## 3.11 Figures

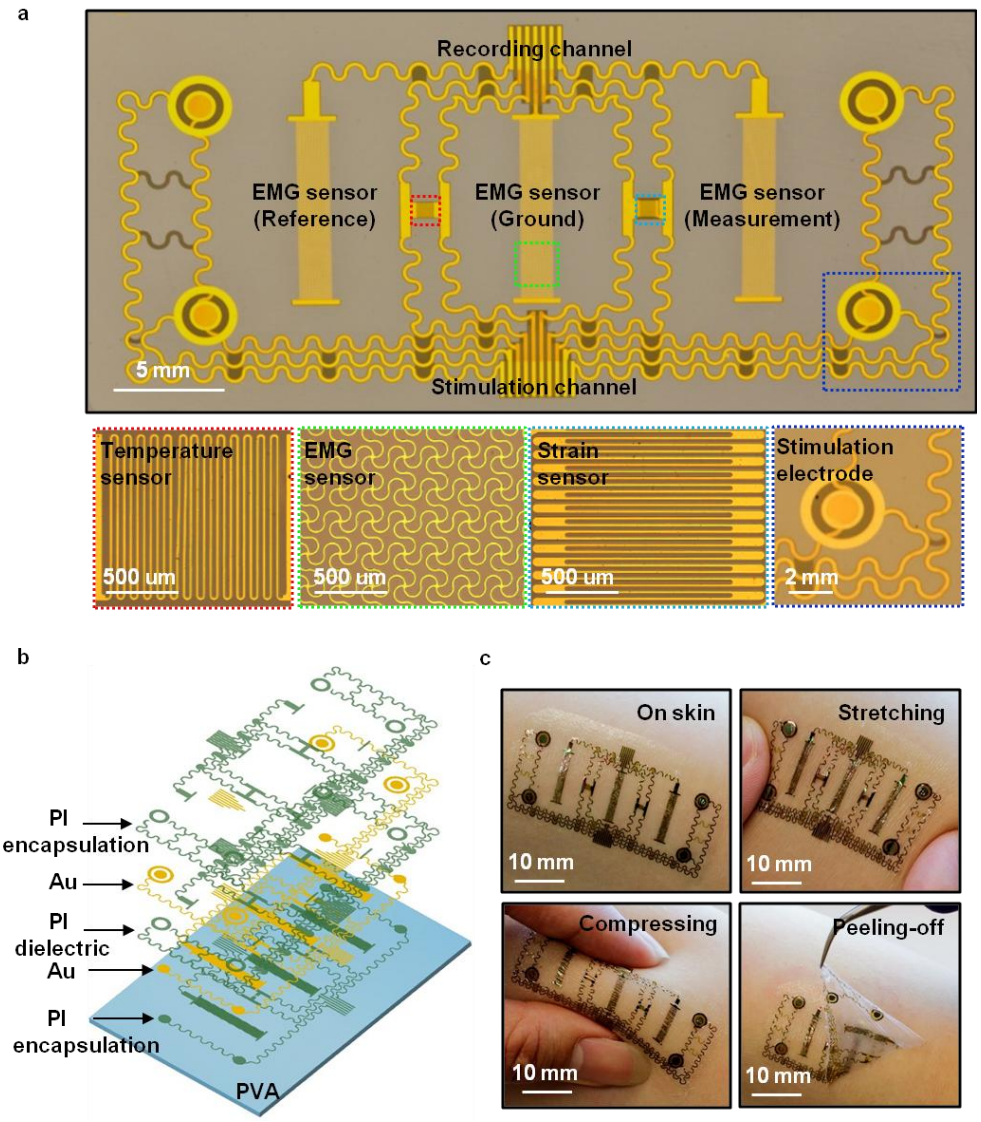


**Figure 3.1 Images and design features of a simple, multifunctional device with skin-like physical characteristics and capabilities in both sensing and stimulation.** (a) Planar view optical micrograph of a representative device. The insets highlight various active regions. (b) Exploded-view schematic illustration of the multilayer construction, comprised only of patterns of metals and dielectrics. (c) Images of a device mounted on the forearm, with examples under stretching, compressing and peeling-off.

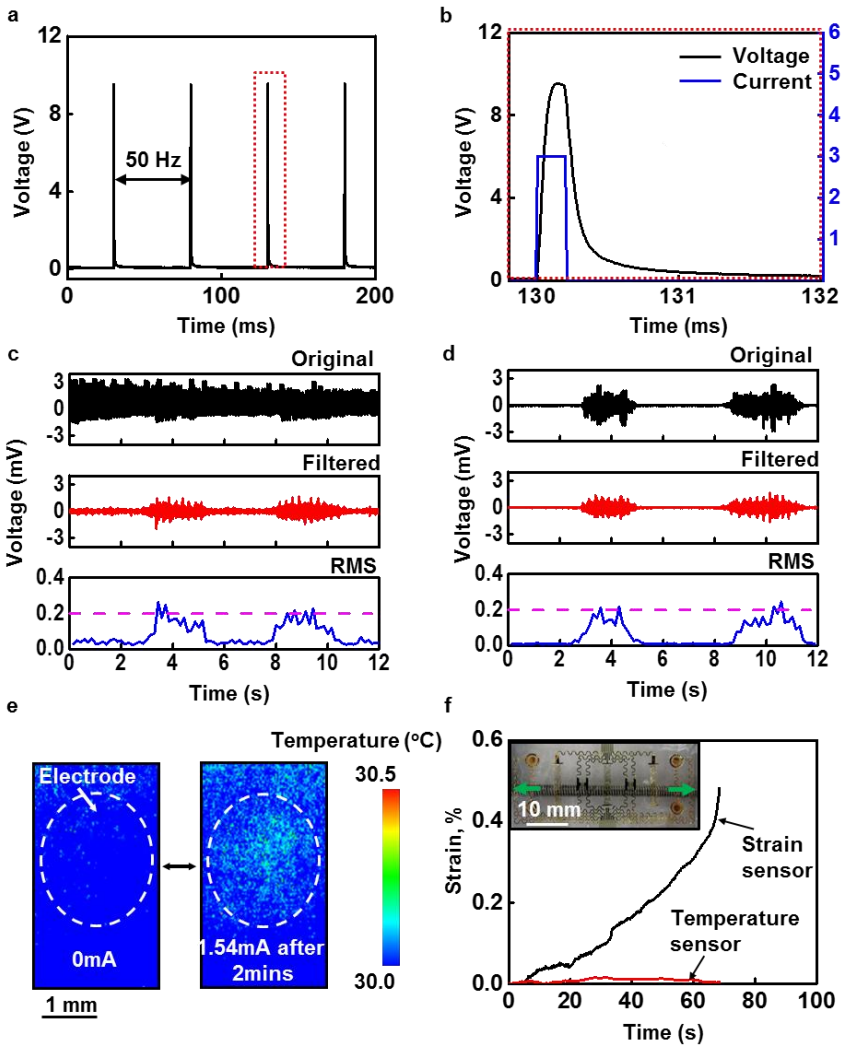


**Figure 3.2 Summary of functional attributes in sensing and stimulation.** (a) Voltage recorded between the two coaxial electrodes associated with an electrotactile stimulator during 20Hz operation at 3mA. (b) Magnified view of the recorded voltage over one period of stimulation (black), with applied stimulation current signal (blue) (c) EMG signals collected from the forearm (original, filtered, and root mean square (RMS)) during simultaneous stimulation through top two electrodes (Figure 1a). The raw recorded data includes signals that arise from the stimulation, which masking the EMG response. Optimized digital filters can remove the effects of stimulation, to yield EMG data that correspond well to recordings performed without stimulation, shown in (d). (e) Infrared images of a stimulation electrode on the skin before (left) and after (right) 2 minutes of 20Hz operation at 1.54mA. (f) Mechanical analysis of the effect of stretch along the x-direction applied to the device, as measured by the epidermal strain gauge, on epidermal temperature measurements taken simultaneously. The inset shows the epidermal device being stretched by a stretcher.

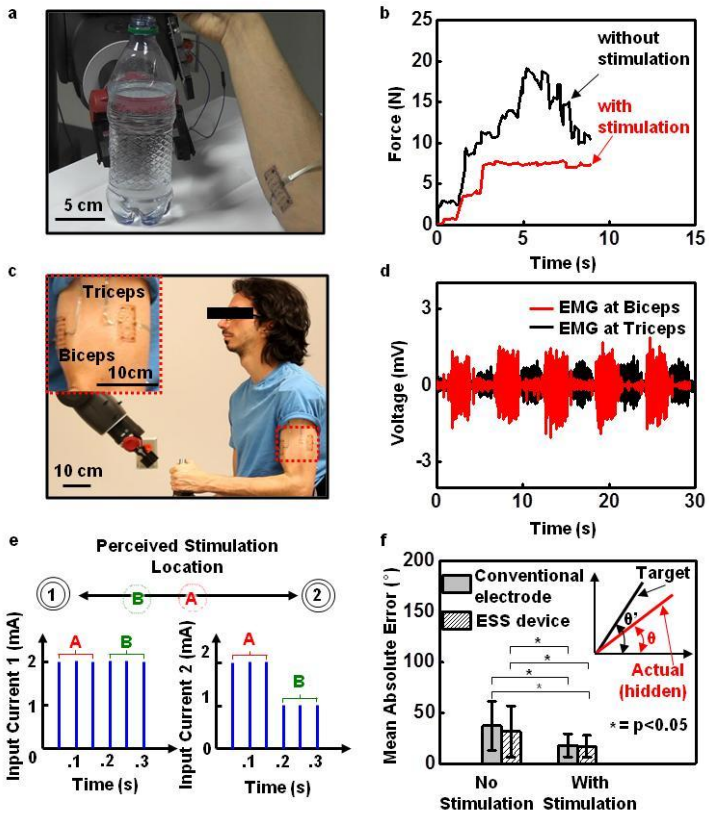


**Figure 3.3 Application in sensorimotor control of a robot arm.** (a) Image of a device on the forearm while controlling a robot arm to grip a bottle filled with water. (b) Gripping force with and without stimulation feedback. When feedback is present, the subject can grip the bottle in a controlled manner, to prevent collapse. (c) Image of devices on the bicep and tricep (inset) during control of the angle of the elbow of a robot arm. (d) EMG signals by two devices when alternating between flexion and extension of the robot arm's elbow angle. (e) Example stimulation waveforms used to produce the tactile funneling illusion. When two stimulation electrodes are simultaneously active, sensation is perceived between the two electrodes. By modulating the stimulation current amplitudes, the location of the perceived sensation can be adjusted to any point between the two electrodes, as shown for current amplitudes A and B in the second electrode. The perceived sensation will be felt closer to the electrode with the higher current amplitude. (f) Accuracies from the virtual arm targeting task comparing performance with and without stimulation using both conventional electrodes and the device ($p<0.05$, One-Way ANOVA, Tukey post-hoc). The hidden virtual arm (inset, red line) was controlled via EMG to match a static visible target joint angle (inset, black line). When stimulation was present, the joint angle of the hidden virtual arm was mapped linearly to a location between two stimulation electrodes via the tactile funneling location.

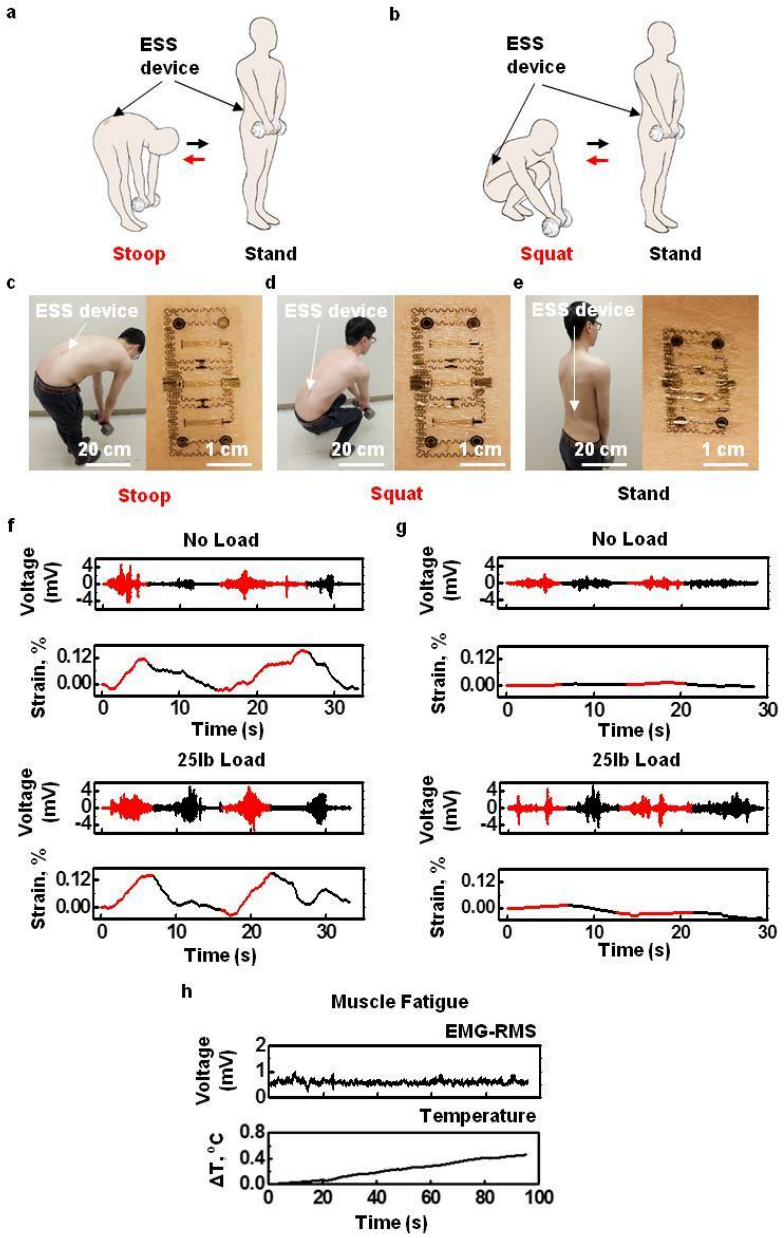


**Figure 3.4 Application in the assessment of exertion and posture of the lower back during lifting.** Cartoon illustration motions associated with (a) stoop lifting and (b) squat lifting. Image of a device mounted on the skin surface of lower back muscle groups and the deformation of device under (c) stoop position with 25lb weight, (d) squat position with 25lb weight and (e) stand position with 25lb weight. (f) Comparison of EMG and strain during stooping (red) and standing (black) with and without a 25lb load (top and bottom, respectively). (g) Comparison of recorded EMG and strain during squatting (red) and standing (black) with and without a 25lb load (top and bottom, respectively). (h) Simultaneously recorded lower back EMG-RMS and temperature signals during muscle fatigue.

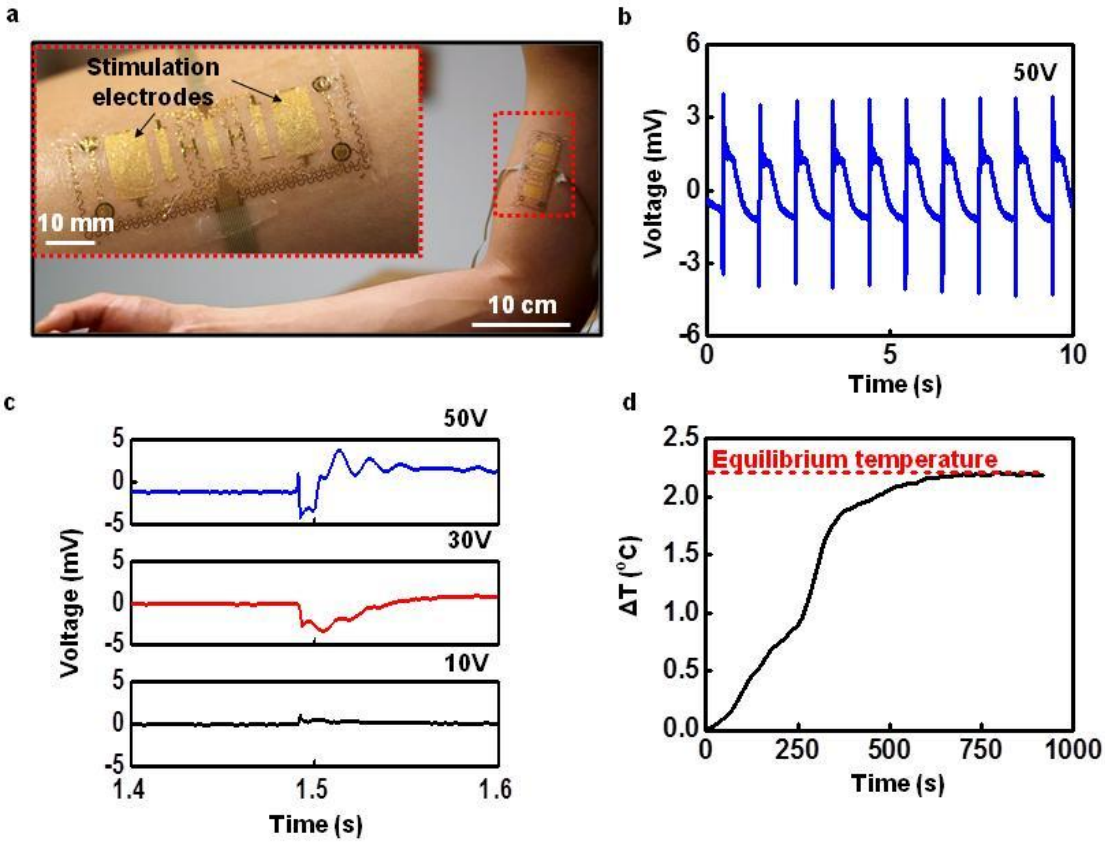


**Figure 3.5 Device with large-area electrodes for electrical muscle stimulation.** (a) Image of a device mounted on the biceps (magnified view, inset). (b) Example of evoked M-waves from induced contraction of the biceps by during 1Hz stimulation at a voltage of 50V. (c) Magnified view of a resulting M-wave at 50V, 30V and 10V stimulations. (d) Measured temperature from epidermal device during prolonged electrical muscle stimulation for 15 minutes.

# CHAPTER 4

# EPIDERMAL MECHANO-ACOUSTIC SENSING ELECTRONICS

Significant portions of this chapter were published as "Epidermal mechano-acoustic sensing electronics for cardiovascular diagnostics and human-machine interfaces," Yuhao Liu, James J. S. Norton, Raza Qazi, Zhanan Zou, Kaitlyn R. Ammann, Hank Liu, Lingqing Yan, Phat L. Tran, Kyung-In Jang, Jungwoo Lee, Douglas Zhang, Kristopher Killian, Sung Hee Jung, Timothy Bretl, Jianliang Xiao, Marvin J. Slepian, Yonggang Huang, Jae-Woong Jeong, John A. Rogers, *Science Advance* (2016). Manuscript is under review.

## 4.1 Introduction

Unusual classes of electronics technologies enabled by recent advances [1, 2, 3, 4, 5, 6] in materials science and mechanics principles can be designed with physical properties that match the soft, mechanical compliance of the skin, thereby allowing long-term (up to ~2 weeks) integration with nearly any external surface of the body, with form factors that resemble those of a temporary tattoo. Such systems, referred to as epidermal electronics, qualitatively expand the range of physiological measurements that are possible in wearable device platforms [7, 8, 9, 10, 11, 12, 13]. Many of these operational modes rely critically on an intimate, physical interface to the skin. Examples include precision measurement of temperature and thermal transport characteristics [14, 15], recording of electrophysiological processes and variations in electrical impedance [16, 17, 18], characterization of skin stiffness [5, 19], and monitoring of quasi-static or dynamic dimensional changes such as those associated with swelling/deswelling or pulsatile blood flow [20, 21]. The critical enabling properties of the devices and their interfaces with the skin include low thermal and electrical contact resistances, small thermal masses, and soft, compliant mechanics. Another, previously underutilized yet important, feature is that the devices can be constructed with

exceptionally low mass densities, approaching those of the epidermis itself. An unexplored consequence of this characteristic is that mechano-acoustic coupling of the device to the body through the skin can be highly efficient. The associated opportunity examined here is in precision measurements of acoustic and vibratory signatures of body processes and of mechanically active implants.

Mechano-acoustic signals are known to contain essential information for clinical diagnosis and healthcare applications [22, 23]. Specifically, mechanical waves that propagate through the tissues and fluids of the body due to natural physiological activity reveal characteristic signatures of individual events, such as the closure of heart valves, contraction of skeletal muscles, vibration of the vocal folds and movement in the gastrointestinal tract. The frequencies range from a fraction of Hz (e.g. respiratory rate [23]) to a thousand Hz (e.g. speech [24, 25]), often with low amplitudes [26, 27]. Physiological auscultation typically occurs with analog or digital stethoscopes, in individual procedures conducted during clinical examinations. An alternative approach relies on accelerometers in conventional, rigid electronic packages, typically strapped physically to the body to provide the necessary mechanical coupling. Research demonstrations include recording of phonocardiograms (PCG; sounds from the heart) [28], seismocardiograms (SCG; vibrations of the chest induced by beating of the heart) [29, 30, 31, 32, 33, 34] and ballistocardiograms (BCG; recoil motions associated with reactions to cardiovascular pressure [28, 30, 35, 36, 37]) and sounds associated with respiration [22, 23]. In the context of cardiovascular health, such measurements yield important insights that complement those inferred from electrocardiograms (ECG). For example, structural defects in heart valves manifest as mechano-acoustic responses and do not appear directly in ECG traces. Previously reported digital measurement methods are useful for laboratory and clinical studies but (I) their

form factors (rigid designs, and large size, e.g. 150 x 70 x 25 mm) limit choices in mounting locations and prohibit practical utility as a wearable, (II) their bulk construction involves physical masses that suppress, through inertial effects, subtle motions associated with important physiological events, (III) their mass densities and moduli are dissimilar from those of the skin, thereby leading to acoustic impedance mismatches with the skin, and (III) they offer only a single mode of operation, without the ability, for example, to capture ECG and PCG/SCG/BCG signals simultaneously.

Here, we present a different type of mechano-acoustic-electrophysiological sensing platform that exploits the most advanced concepts in stretchable electronics to allow soft, conformal integration with the skin. The result allows precision recordings of vital physiological signals in ways that bypass many of the limitations of conventional technologies. The mechano-acoustic modality leverages miniaturized, low-power accelerometers with bandwidths tuned to essential body processes (0.5 Hz to 550 Hz) and associated conditioning electronics. Soft, strain-isolating core-shell packaging assemblies, together with electronics for electrophysiological recording from dry, capacitive electrodes, represent the other essential features of these stretchable systems. The resulting devices with masses, thicknesses, effective moduli and bending stiffnesses that are 213.6 mg, 2 mm, 31.8 kPa (in x-direction), 31.1 kPa (in y-direction), 1.02 N-m (in x-direction), 0.94 N-m (in y-direction), which correspond to values that are orders of magnitude lower than those of previously reported. The outcomes include qualitative improvements in measurement capabilities and wearability, in formats that can interface with nearly any region of the body, including sensitive parts of the neck for capturing signals associated with respiration, swallowing and vocal utterances. The following describes the key properties of these devices and demonstrates their utility in wide ranging examples, from human

studies on patients with cardiovascular disease to human-machine interfaces for video game control. Specific data show simultaneous recording of arterial pressure variations on the neck, (EP) signals and SCG from the chest for systole and diastole cardiac cycles, and four auscultation sites (Aortic, Pulmonary, Tricuspid, and Mitral) for heart murmurs. Vibrational acoustics of ventricular assist devices (VADs), i.e. devices utilized to augment failing myocardial function, though often complicated by intra-device thrombus formation, can be captured and used for detection of pump thrombosis or drive malfunction. Beyond cardiology, applications exist in speech recognition and classification for human-machine interfaces, in modes that capture vibrations of the larynx without interference from noise in the ambient environment. Baseline studies on the biocompatibility of the skin-interface, the mechanical properties and fundamental aspects of the interface coupling provide additional insights into the operation.

## 4.2 Device Design and Circuit Considerations

The mechano-acoustic-electrophysiological sensing platform introduced here incorporates filamentary serpentine copper traces (3 μm, placed at the neutral plane between layers of polyimide encapsulation, 1.2 m) as interconnects between commercial, small-scale chip components, all encapsulated above and below by an ultra-low modulus elastomeric core (Silbione RT Gel 4717 A/B, Bluestar Silicone, $E$ = 5 kPa [2, 38]). A thin layer of a low modulus silicone (Ecoflex, Smooth-on, $E$ = 60 kPa [9]) serves as a shell (figures. 4.1A). This core/shell structure minimizes physical constrains on motions of the interconnects to improve stretchability [2, 7, 8, 9, 11] and it mechanically isolates the constituent device components to reduce stresses (and associated discomfort) at the skin interface, as described in detail previously [38]. Openings in this structure provide access to contact pads for attaching a pair of electrophysiological measurement electrodes (Au, 200 nm) and a thin cable connection (ACF, Elform, 100 μm) to an external data

acquisition system (figure 4.1B). The result is a soft, skin-compatible device platform (figures. 4.1C) that can accommodate significant levels of deformation without altering the operation (figures 4.1D). The direct mechanical interface to the skin, the robustness of adhesion that follows from the low modulus construction, the low total mass and the multifunctional operation represent key distinguishing features over previously reported wearable accelerometers. Each of these attributes is critical to the operational modes described in the following.

The sensing circuit consists of a mechano-acoustic sensor (ADXL 335, Analog Devices), low pass and high pass filters, a pre-amplifier (TSV991A, STMicroelectronics, USA), and removable and reusable capacitive electrodes for EP recording[8]. The sensor has a frequency bandwidth (0.5 – 550 Hz) that lies between the range of targeted cardiovascular sounds and speech. For healthy adults, the first ($S_1$) and the second sound ($S_2$) of the heart have acoustic frequencies at 10–180 Hz and 50–250 Hz, respectively [39]. Vibration frequencies of vocal folds in humans in the range 90–2000 Hz [40], with an average fundamental frequency of ~116 Hz (Male, Mean age: 19.5), ~217 Hz (Female, Mean age: 19.5), and ~226 Hz (Child, Ages 8 to 11) in conversation [41]. To enable sensing of cardiac operation and speech, the cutoff frequency of the low pass filter is 500 Hz. The high pass filter (cutoff frequency = 15 Hz) removes motion artifacts.

## 4.3 Device Characterization

The experimental and simulation results of figure 4.1 summarize key characteristics of the materials and structures that lead to the type of soft mechanics, water permeability and adhesive, biocompatible surfaces needed for comfortable, robust, long-lived integration on the skin. Results show that an additional base layer of silbione on the bottom shell surface can provide adequate adhesive force (1.16 kPa) for a non-destructive and reversible attachment to

skin. Measurements of water-vapor permeability of silbione, in combination with previously reported results of Ecoflex [2], demonstrate that the core-shell encapsulation layer has a water-vapor transmission loss rate that is similar to that of widely used medical tapes (Tegaderm, 3M Medical).

Cytotoxicity tests that involve culturing mouse embryonic fibroblast cells (MEFs) on the surfaces of the device for 5 days demonstrate biocompatibility. Specifically, cells spread uniformly over the samples and remain attached for the duration of the assay, with no observable signs of apoptosis or necrosis (figure 4.1E). Visualizing cells at 1, 3, and 5 day time points by staining with calcein AM and ethidium homodimer-1 (EthD-1) indicates >95% viability after 5 days.

Experimental studies and three dimensional finite element analysis (3D-FEA) of the system under a bi-axial strain of 25% allows examination of the mechanics for levels of deformation that exceed those likely to be encountered on the skin. Optical images and corresponding simulation results in figure 1F show good agreement. The strain contour in the upper layer of figure 1F indicates that the maximum principal strains in most locations are below 1%. Large strains (~2.5%, still below the fracture threshold of the PI/Cu/PI system) occur only in certain regions of the interconnects, highlighted by the red dashed box. Figure 4.1G shows a magnified view of this region, where the influence of two adjacent components leads to a local region of strain concentration. The calculated strains are lower than the fracture strain of copper (~5%), indicating a total biaxial stretchability of the device that is larger than 25%. Consistent with previous studies, stretching is mainly absorbed by deformations of the serpentine interconnects [5]. Assuming a yield strain of ~0.3 % in the copper, the elastic stretchability in both directions is ~4.6 %. Results of 3D-FEA for an otherwise identical system, but without any of the

device components. The deformation patterns also show good agreement with experiment when bi-axially stretched by 25%, with a similar strain concentration effect is observed in the same region. Stress-strain measurements along the device length reveal effective moduli of ~32.1 kPa (with chips) and ~8.68 kPa (without chips), much smaller than the epidermis (~100 – 200 kPa), and confirm the stretchability up to 25% strain. The layouts can be adjusted to meet application requirements.

The mechano-acoustic response captured without analog filters using a vibration simulator (3B Scientific) shows the expected frequency bandwidth. For use on the body, the depth of the source varies according to location and associated organ. As examples, the larynx is ~5 mm below the surface of the neck, and the valves of the heart are ~30 mm away from the surface of the chest. In vitro experiments use fresh chicken breast with thicknesses between 1 mm to 30 mm placed between the sensor and vibration simulator to simulate the effects of this separation. Results indicate that the spectral power of the measured response exhibits a power law behavior with respect to frequency and an asymptotic decay with respect to tissue thickness (figure 4.1H), as expected from the acoustic attenuation [42, 43] by absorption and scattering in viscoelastic materials [44, 45, 46]. The average decrease in spectral power between frequencies in the measurement range is 51% on 1 mm tissue and 83% on 30 mm tissue.

Partly due to this attenuation and partly due to the small amplitudes at the source, mechano-acoustic signals at the surface of the skin are relatively weak, and increasingly so with increasing frequency[43]. Measurements, therefore, must account for effects in mechanical coupling and impedance match between the devices and the skin. The mass of the sensor system is an important characteristic in this regard. Increasing the mass increases the mechanical load at the skin interface, thereby decreasing the mechano-acoustic motions. In vitro experiments to

demonstrate the effects involve experiments like those described above but with the sensor placed in an acrylic box (19 x 42.5 x 55 mm, 9.36 g) with different added test masses (figure 4.2). Results in figures 4.2A to 4.2C show a general trend of decreasing spectral power with tissue thickness and mass for all frequencies. A simple mechanical model consisting of a mass, a spring and a damping source (**Supplementary Note 1**) can capture the overall behaviors (figure 4.2D). The computed results at three different frequencies, 50 Hz, 100 Hz and 200 Hz indicate that the response decreases with increasing mass, tissue thickness and frequency. In vivo studies of speech recognition confirm that increasing mass leads to decreasing signal (figure 4.2E).

In addition to overall mass, the distribution of this mass and the overall mechanics of the structure are important. In particular, in a soft, low modulus device platform, only the mass of the mechano-acoustic sensor chip is important; whereas in a rigid platform, the overall mass limits the performance. Results in figure 4.2F verify that in a low modulus device platform, added mass is only significant when located at the position of the sensor, and that added mass at different locations have similar loading effects for the case of a rigid platform. Finite element analysis of a similar system (**Supplementary Note 2**) is consistent with the experimental data. These findings suggest that low mass and low modulus characteristics are critically important. An additional implication is that in physical forms reported here, batteries, radios and other components of interest for future embodiments can be included in the platform without adversely affecting the measurement process.

## 4.4 Seismocardiography Measurement

Seismocardiography (SCG) captures the thoracic vibrations from atroventricular contractions and blood ejection into the vascular tree by on the skin of the sternum [22, 29, 47]. Each beat cycle produces a characteristic SCG complex, as a quasi-periodic waveform with frequncy

components that reflect contraction of the heart muscle and associated ejection of blood. Figure 4.3A shows a device and its pair of conformal capacitive electrodes laminated onto the sternum for simultaneuous measurements of SCG and ECG.

A single cardiac cycle includes systole (contraction of heart muscle) and diastole (relaxation of heart muscle) motions of the atria and the ventricles as illustrated in figure 4.3B. These motions involve electrical signals followed by mechanical coupling and a sequence of mechano-acoustic signatures as the heart chambers contract and valves close. These electrophysiological and mechanical data form the basis of electrocardiograms and cardiac auscultations, respectively. Figure 4.3C shows ECG and SCG signals measured simultanuously from a healthy male subject (Age 22). Magnified views of a single cardiac cycle (figure 4.3D) highlight all of the key features of these two waveforms. This information is useful in the assessment of systolic and diastolic ventricular function. For example, the electromechanical activation time (the time interval from the onset of the QRS to the point of peak intensity of $S_1$) corresponds to the time required for the left ventricle (LV) to achieve sufficient pressure to force the mitral valve closed. Its prolongation indicates systolic heart failure. Reductions in the interval between $S_1$ and $S_2$ (termed left ventricular systolic time (LVST)) is a sign of LV dysfunction. Overall, data from the epidermal mechano-acoustic sensors reported here have a quality comparable to that of data obtained using a commercial electronic stethoscope (JABES Electronic Stethoscope, GS Technology Co.), where $S_1$ and $S_2$ are clearly delineated (figure 4.2E). This device can also measure pressure pulse waves associated with arterial blood flow. A sensor placed on the carotid artery at the neck can capture such data, along with ECG signals.

For subjects with cardiovascular pathologies, murmurs are often present in addition to signatures associated with $S_1$ and $S_2$. The holo systolic murmurs of the mitral and tricuspid valve

regurgitation that occur during systole have acoustic signatures of characteristic constant intensity and high frequency. In constrast, diastolic murmurs are often detected in patients with aortic or pulmonic valve regurgitation (44-45). Clinical validation of the device operation in this context involves recording cardiac mechano-acoustic responses with ECG signals from eight patient volunteers diagnosed with cardiac valvular stenosis or regurgitation. Figure 4.3G shows the auscultation mounting sites that yield optimal results for the aortic (A), pulmonary (P), tricuspid (T) and mitral (M) heart valves. An elderly patient (Female, Age 78) with diagnosed mild tricuspid and pulmonary regurgitation by echocardiography reveals a short, constant intensity murmur at tricuspid and pulmonary sites in systole and diastole, respectively as indicated by the arrows (figure 4.3, G to J). Measurement from the aortic site shows no signs of stenosis or regurgitation. Signal from the mitral site is weak, likely due to non-optimal sensor placement.

## 4.5 Acoustic Analysis of Ventricular Assist Devices

Additional biomedical applications are in monitoring of mechanical circulatory support devices such as those that augment dysfunctional ventricular pump function, and serve as important temporary or permanent alternatives to heart transplantation[48]. The latest continuous flow left ventricular assist devices (LVADs) offer improved durability and hemodynamic restoration, though with the limitation of adverse events, including a loss of pump function due to pump thrombosis or other mechanical failure[49]. Previous work in the context of the first failure mode shows that the formation of blood clots on the rotor leads to changes in the sounds of the pump[48, 49, 50, 51, 52]. These changes can be difficult or impossible to discern using stethoscopes or unaided human hearing, particularly for early stage thrombosis. The mechano-acoustic sensors reported here enable a surface-mounted mode for monitoring changes in vibration signatures in

the LVAD pump. Studies reported here focus on an *in-vitro* model with a commercial LVAD (HeartMate II, HM II; Thoratec Corporation, Inc., Pleasanton, CA, USA) and continuous flow for detecting changes in acoustic signal correlating to variation in pump speed, circulating fluid, and thrombus embolization.

The experimental system consists of a circulatory closed loop that involves medical grade tubing (Tygon) connected to HM II with valves to assist in removal of air bubbles and to allow introduction of blood clots. The device laminates conformally onto the metal housing of pump impeller and brushless DC motor to provide direct measurements of vibration (figure 4.4A). The spectral power of signal collected for a short time (30 s) during operation of HM II at 8400 RPM appears in figure 4.4B. The panel in the lower part of figure 4.4B shows characteristic signatures at A - 139.7 Hz, B - 166 Hz and its second harmonic at 332 Hz. Increasing the pump speed from 8400 RPM to 9400 RPM leads to decreases in the frequency of peak A from 139.7 Hz to 156.2 Hz (figure 4.4C), while peak B stays unchanged (figure 4.4D). These data suggest that peak A can serve as a reliable indication of pump speed. Replacing water with glycerol, a fluid medium with viscosity similar to blood serum but higher than water, leads to no significant change in the acoustic signature (figure 4.4E). This result suggests that the acoustic signatures are dominated by pump rotation, and they are insensitive to changes in circulating fluid viscosity.

Introducing a 500 μL blood clot prepared from bovine whole blood through the air valve at the inflow of the HM II during operation at 9400 RPM serves to simulate thrombosis and embolization. Immediately after injection, the blood clot travels through the LVAD and exits the outflow tubing with minimal distortion. The associated widening of peak A suggests that clot interaction with the pump impeller produces additional frequencies (figure 4.4F, top panel). While the clot travels through the remainder of the circulation loop, the pump remains

undisturbed and the vibration signature returns to its initial, i.e. two-peak state, but with peak A at a higher amplitude than peak B (figure 4.4F, second panel), possibly due to tiny blood clots attached on the pump impeller. After several passages, the clot dissipates completely into microscopic fragments invisible to the unaided eye. This process creates another strong group of frequencies around peak A (figure 4.4F, third panel). Finally, the vibration signature restores to the circulation state, with peak A again at higher amplitude, confirming previous observation (figure 4.4F, bottom panel). These results serve as a reference that validates the use of an accelerometer to capture acoustic signatures in LVAD for pump thrombosis detection and monitoring.

## 4.6 Speech Recognition and Human-machine Interfaces

Two features of epidermal mechano-acoustic devices (figure 4.5A), specifically their use of multiple sensors in a single device platform and their compatibility with direct placement on even sensitive regions of the skin, enable unusual applications in speech capture and recognition. Implications range from improved communication capabilities for individuals with speech impairments [53] to the design of voice activated human-machine interfaces [54, 55, 56, 57, 58].

First, with appropriate placement, epidermal mechano-acoustic devices can simultaneously capture both EMG signals from articulator muscle groups and acoustic vibrations from the vocal chords. Figure 4.5B shows EMG signals (top) and mechano-acoustic vibrations (bottom) recorded while speaking ‘left’, ‘right’, ‘up’, and ‘down’. The spectrogram (figure 4.5C – top left) highlights the unique time-frequency characteristics of each of the four words. The low frequency components of the nasal consonant in ‘down’ are particularly prominent. Previous research suggests that the fusion of multiple sensors can improve speech recognition [59, 60, 61]. A specific suggestion is that throat EMG can enhance traditional speech recognition

techniques [58, 62], although simultaneous recording of EMG and acoustics in a single device has not been demonstrated. In fact, an earlier study [53] showed that fusion of acoustic data with EMG signals measured using separate devices improved word recognition accuracy in a small group of patients with dysarthria.

Second, the intimate contact between the sensors and the skin renders their operation almost unaffected by ambient acoustic noise. Figure 4.5C compares spectrograms of speech ('left', 'right', 'up', 'down') recorded by an epidermal sensor and by a standard microphone (iPhone, Apple Inc.). In a quiet environment, both the epidermal sensor and the microphone show similar responses. A noisy environment, on the other hand, significantly degrades the quality of recording from the microphone but does not affect the epidermal sensor. This feature could allow the epidermal acoustic sensor to be used for communication in loud environments such as by first responders [63], ground controllers, or security agents.

A simple isolated word detection system, used it in real-time to play a Pac-Man game, demonstrates the potential of the epidermal acoustic sensor for human machine interfaces. Implementation begins with a training phase based on four commands: 'left', 'right', 'up', and 'down'. Preprocessing involves implementation of noise reduction techniques, which does not alter classification accuracy. Classification occurs in real-time using linear discriminate analysis (LDA). A confusion matrix (figure 4.5D) summarizes the accuracy of this classifier, in which the columns represent the predicted word and the rows represent the targeted word. In this example, the recognition accuracy is 90%. Further improvements are possible through additional training, different classification methods [64], and a wider pass-band on the sensor. A video of a user playing a Pac-Man game appears in the published version; these same speech recognition strategies can be applied to almost any type of HMI, such as drone and prosthesis control [9, 11, 12].

## 4.7 Conclusions

The class of device reported here exploits thin, lightweight, low modulus and skin-compatible architecture to enable mechano-acoustic sensing. These physical attributes, while important for wearability and comfort in previous types of 'epidermal' technologies, represent critically important, enabling features for the systems introduced here because they allow high fidelity mechanical coupling across the skin/device interface. The results create many opportunities in precision recording of sounds and vibratory signatures not only of natural body processes but also of the operation of mechanical implants such as LVADs. Bench studies and simulation results highlight the fundamental physics associated with this type of sensing. A range of uses with human subjects, in contexts ranging from cardiovascular diagnosis in the detection of regurgitation heart murmur at pulmonary and tricuspid auscultation sites, to machine interfaces in the real-time control of computer gaming systems, foreshadows some of the broad ranging uses of these concepts. Other potential clinical applications include heart rate variability analysis, and beat-to-beat assessment of the pre-ejection period, and left ventricular ejection time. Body sounds ranging from snoring, respiration and gastrointestinal tract movement are also of some interest. In many cases, fully wireless capabilities in data transfer, on-board data storage/processing and integrated power supply will be necessary, particularly for applications that require continuous, untethered operation. Preliminary data indicate that the most advanced commercial skin-mounted devices with these features (BiostampRC, MC10, Inc) offer areal mass densities and low modulus designs that are sufficient to allow same level of mechano-acoustic sensing, as well as multifunctional operation in EP recording. Further optimization of the mechanics and mass distributions associated with this platform, using the design rules outlined here, and exploration of its use in clinical applications to establish a catalog of mechano-acoustic

signatures of health/wellness represent promising directions for future research.

## 4.8 Methods

### Fabrication of epidermal mechano-acoustic device

The fabrication process involves three parts: (1) patterning of the circuit interconnects, (2) transfer printing and chip bonding onto a soft, core/shell substrate and (3) covering the top surface with a similar soft core/shell structure. Fabrication of the interconnects began with a commercial laminate (Microthin, Oak Mitsui Inc.) that contains a copper carrier film (17.5 μm) and thin copper foil (3 μm) separated by a release layer. Spin-coating and thermal curing formed a film of polyimide (1.2 μm, PI 2545, HD Microsystems) on the side with the thin copper foil (3 μm). Peeling this PI coated layer from the thick copper layer allowed its attachment onto a glass slide coated with poly(dimethylsiloxane) (PDMS, Sylgard 184, Dow Corning). Photolithography and metal etching defined a pattern of interconnects in the copper. Another spin-coating and curing process yielded a uniform layer of PI on the resulting pattern. Photolithography and reactive ion etching (RIE, March, Nordson) yielded top and bottom layers of PI in geometries matching those of the interconnects. (2) A piece water soluble tape (Aquasol, New York) enabled transfer of these encapsulated interconnects onto a trilayer film supported by a silicon wafer, prepared by spin-coating (4000 RPM) and curing a thin layer of an ultrasoft silicone (Silbione, RT Gel 4717 A/B, Bluestar Silicones), followed by a layer of a slightly stiffer silicone (Ecoflex, 00-30, Smooth-on) at 1000 RPM and finally another layer of ultrasoft silicone at 1000 RPM. This trilayer defined the skin-adhesive interface and the core/shell substrate. Removal of the tape by immersion in water exposed the interconnects to allow bonding of the device components onto designated pads using solder paste (Ind. 290, Indium Corporation) and a heat gun at ~165 ℃. (3) Encapsulation began with manual placement of cured, individual pieces of

silicone onto the pads that connect to the ECG electrodes and to those that interface to the ACF cable. Spin-coating (1000 RPM) and curing a layer of Silbione followed by a layer of Ecoflex at 1000 RPM defined the core/shell superstrate. Removal of the silicone pieces completed the fabrication process. Attachment of the ACF cable and ECG electrodes occurred just prior to mounting the device on the skin.

**Device Characterization**

**Adhesive force tests**

Standard vertical peel measurements defined the adhesive force between test samples and the skin on the flexor muscle. Each sample (2.5x2.5 cm, 1 mm thickness) was prepared by mixing monomer and curing agent components for Silibone and Ecoflex and then thermally curing the materials. The bi-layer structure consisted of a 500 μm thick layer of Ecoflex on a glass substrate, with a 500 μm thick layer of Silbione on top. The test substrate was placed on the skin and a corner of the substrate was attached to the hook of a force gauge at 90 degree (Mark-10, USA). The reported strength of adhesion corresponds to the measured force divided by the substrate area.

**Transmission water-vapor loss test**

Measurements of water-vapor loss follow standards in ASTM E96-95. Films of Silbione were prepared by spin-coating at 250, 500, 1000, and 2000 RPM on wafer substrate. Flasks (125 mL) were filled with dry cobalt chloride (Drierite) at equal weight, and sealed with the Silbione/Ecoflex films using plastic bands. Changes in weight of each flask were recorded daily for 6 days. The water vapor transmission rates follow from these measurements.

**Cell Viability Assay**

Mouse embryonic fibroblasts (MEFs) were obtained from Professor Kristopher Kilian's laboratory. MEFs were isolated from embryos at day 13 d.p.c. (day post-coitum) with 0.05% Trypsin (Gibco). Cells were cultured in Dulbecco's Modified Eagle's Medium (DMEM) high glucose (4.5g/mL) media supplemented with 10% fetal bovine serum (USA origin, Sigma), 1% penicillin/streptomycin. Media was changed every 3 days and passaged at 80% confluency.

Device samples were sterilized by autoclaving at 121℃ for 60 min., followed by exposing to UV irradiation for 30 min. and finally by washing in phosphate buffered saline (PBS). The device surface was exposed to 25µg/mL of laminin (Sigma L2020) in PBS for 30 min. then transferred to a 6-well plate. MEFs were seeded on samples at an initial concentration of 20,000 cells/mL and cultured for 5 days. After 1, 3, and 5 days in culture, devices were incubated with Hoechst 33342 (1µg/mL), calcein AM (2µM), and ethidium homodimer-1 (EthD-1, 4µM) in PBS solution for 20 minutes. Samples were mounted onto glass slides and imaged with an INCell Analyzer 2000 (GE). Immunofluorescent images were analyzed using ImageJ software. Measurements of cell viability correspond to the proportion of live cells (green) over all cells (green + red). Cells grown on tissue culture plastic (TCP) in standard DMEM and in DMEM with 10% DMSO served as positive and negative controls, respectively.

**Characterizing the vibration response**

Tests involved attaching the devices, without analog low and high-pass filters, to a flat aluminum stand mounted on a vibration generator (3B Scientific, USA). The vibration was generated by a 1

cm pole connected to the diaphragm of a loud speaker (SR 1010, Somogyi, 50 W, 100 mm, 8 Ohm) fitted inside a plastic housing. The square-wave output of a function generator (FG100, 3B Scientific) provided 3 V output to the loud speaker at discrete frequencies of 1, 5, 10, 50, 100, 250 and 500 Hz. A commercial system (Powerlab, AD instrument) enabled data acquisition, without filters, at a sampling rate of 1 kHz.

Measurements of the influence of tissue thickness used fresh chicken breast (Miller Amish Poultry, Illinois) sliced into 2 cm by 2 cm pieces at thicknesses of 1, 5, 10 and 30 mm. When inserted between the sensor and the vibration stand (4 x 4 cm), the moist surfaces of the tissue ensured sufficient adhesion to prevent relative movement during vibration, using square waves with amplitudes of 3.7V and frequencies of 50, 100, 200, 300, 400, and 480 Hz.

Effect of mass and tissue thickness used the same experimental setups described above. The sensor was taped firmly to the bottom center of an acrylic box (19 x 42.5 x 55 mm, 9.36 g). A medical tape (Silicone Tape, 3M Medical) wrapped onto the vibration stand stabilizes the box on the chicken tissue. Screw nuts (3/8”, 1.38 g) were used as elements for added mass, fixed firmly to the top cover of the acrylic box by a double-sided adhesive.

Speech sensing was evaluated using a sensor placed in the acrylic box as described above. Measurements involved acoustic vibrations associated with a subject saying “left” with different added mass. The acrylic box attached to the subject’s throat via doubled-sided adhesive between the skin and box interface, and medical tape on top of the box. To study the effect of mass location, a set of four mass elements were connected in a column and attached to the middle,

upper right, upper left, lower right, and lower left locations of the bottom of the box.

**Mechanical modeling and finite element analysis**

Three-dimensional finite element analysis (FEA) simulations based on commercial software packages (ABAQUS) guided optimization of the mechanics of the system. The elastomers were modeled by eight-node, three-dimensional hexahedron elements (C3D8R). The electronic chips, serpentine interconnects and polyimide layers were modeled by four-node shell elements (S4R). Displacement boundary conditions applied to the substrate allowed the system to be stretched. The Young's modulus (E) and Poisson's ratio (ν) of the materials were as following: $E_{Silbione}$ = 5 kPa, $\nu_{Silbione}$ = 0.48 for Silbione; $E_{Ecoflex}$ = 60 kPa, $\nu_{Ecoflex}$ = 0.48 for Ecoflex; $E_{PI}$ = 2.5 GPa, $\nu_{PI}$ = 0.34 for polyimide; $E_{Cu}$ = 119 GPa, $\nu_{Cu}$ = 0.35 for copper.

FEA using ABAQUS also determined the effects of frequency, mass and tissue thickness on the mechano-acoustic signal. Here, three dimensional hexahedron elements (C3D8R) were used to model the tissue, the mass objects, and the accelerator, all under a sinusoidal force input. The tissue was modeled as a viscoelastic solid, with Young's modulus 0.18MPa [65] and a Prony series function with constants $g_i = k_i = 0.91001$ and $\tau_i = 0.9899$ sec. After frequency analysis of the whole system, modal dynamic was chosen as the analysis method to simulate system vibration.

**Demonstrations of seismocardiography**

Clinical tests at Camp Lowell Cardiology (Tucson, AZ) involved eight elderly patients as volunteer, all providing informed consent. Optimal sensor placement site at traditional aortic (A), pulmonary (P), tricuspid (T), mitral (M) locations was determined by ultrasound probes with

verification of heart murmurs by echocardiogram (GE Healthcare). A 3-lead setup enabled simultaneous recording of ECG using the same device platform. A Powerlab system (AD instrument) with bio-amp module served as the hardware for data acquisition and analysis. During measurement, the subject was asked to "stop breathing" for 3 seconds, then to "breathe normally" after a verbal count-down to eliminate the respiratory effect on the baseline and amplitude of the SCG data. Passing the output of the accelerometer through a 20 Hz low-pass digital filter followed by an A/D converter in the Powerlab system yielded processed data at a sampling rate of 1 kHz. A band-pass digital filter with 1 Hz low cut-off and 30 Hz high cut-off frequency was used with the ECG signal. All vibration signals were converted from output voltage to "Mechano-acoustic Response (arbitrary units)".

**Measurements from left ventricular assisted devices (LVAD)**

The test platform consisted of closed loop created by connecting a commercial LVAD (HeartMateII, Thoratec Inc., Pleasanton, CA) and respective driver, by ~1 m of medical grade tubing (Tygon) at the inlet and outlet, with syringe ports at each location for introduction of water, without air bubbles. Tape secured the device the housing of the LVAD. Baseline studies involved measurements of vibration during operation of the LVAD at various speeds between 8400 RPM to 9400 RPM, with 200 RPM increments. Additional similar experiments used 30% (v/v) glycerol in water.

Studies of the effects of VAD thrombosis utilized fresh blood clots formed via addition of calcium chloride added to 10% (v/v) acid citrate dextrose (ACD) in fresh bovine whole blood, to reach a concentration of 25 mM. Blood clots formed spontaneously during storage overnight at

room temperature. Clots with weights of ~250 mg were introduced into the closed loop before activating the LVAD. The sensor response was recorded during circulation of a single clot while operating the LVAD at 9400 RPM. Additional similar experiments used 30% (v/v) glycerol in water.

**Algorithms for classification of data related to speech**

Real-time classification of speech signals relied on a simple four class (*'left', 'right', 'up', 'down'*) isolated word recognition system with a *'null'* state. Prior to classification, the data was preprocessed to reduce ambient noise using spectral subtraction [66] and then digitally filtered, using an eighth order Butterworth filter, from 30 Hz to 1000 Hz. The resulting data were defined as *'null'* unless the root mean squared value surpassed a threshold. Analyzing the energy of the signal in a sliding 50 ms window enabled determination of the exact onset and offset of the word. Fourier transformation with a 100 ms time window and a 70ms overlap defined time frequency estimate of the data during the duration of the word. The results were averaged and reduced in dimensionality using principal component analysis to form a feature vector. This feature vector was finally classified using LDA. Training involved 20 trials from each class, with 90% accuracy (figure 4.5D). The resulting classifier enabled real-time operation in a simple video game (https://pypi.python.org/pypi/pacman-game/).

**Experiments on human subjects**

All experiments on human skins were conducted under approval from Institutional Review Board at the University of Illinois at Urbana-Champaign (protocol number: 13229) and received informed consent from the volunteer subjects.

**Statistical and Data Analysis**

Spectra shown in figures 4.2, 4.4 to 4.5 resulted from a Fast Fourier Transform algorithm with 1024 window size, Hann (cosine-bell) window type, and 50% overlap. For data displayed in Spectral Power mode, the signal corresponded to an average of 3 FFTs in frequency domain. All data processing was performed using LabChart and OriginLab.

## 4.9 References


1. Fan JA, Yeo W-H, Su Y, *et al.* Fractal design concepts for stretchable electronics. *Nature Communication* **5**, (2014).

2. Jang K-I, Han SY, Xu S, *et al.* Rugged and breathable forms of stretchable electronics with adherent composite substrates for transcutaneous monitoring. *Nature communications* **5**, (2014).

3. Jeong J-W, McCall Jordan G, Shin G, *et al.* Wireless Optofluidic Systems for Programmable In Vivo Pharmacology and Optogenetics. *Cell* **162**, 662-674 (2015).

4. Kim D-H, Lu N, Ma R, *et al.* Epidermal Electronics. *Science* **333**, 838-843 (2011).

5. Wang S, Li M, Wu J, *et al.* Mechanics of epidermal electronics. *Journal of Applied Mechanics* **79**, 031022 (2012).

6. Xu S, Yan Z, Jang K-I, *et al.* Assembly of micro/nanomaterials into complex, three-dimensional architectures by compressive buckling. *Science* **347**, 154-159 (2015).

7. Hattori Y, Falgout L, Lee W, *et al.* Multifunctional Skin-Like Electronics for Quantitative, Clinical Monitoring of Cutaneous Wound Healing. *Advanced healthcare materials* **3**, 1597-1607 (2014).

8. Jeong JW, Kim MK, Cheng H, *et al.* Capacitive Epidermal Electronics for Electrically Safe, Long-Term Electrophysiological Measurements. *Advanced healthcare materials* **3**, 642-648 (2014).

9. Jeong J-W, Yeo W-H, Akhtar A, *et al.* Materials and Optimized Designs for Human-Machine Interfaces Via Epidermal Electronics. *Advanced Materials* **25**, 6839-6846 (2013).

10. Kim J, Banks A, Cheng H, *et al.* Epidermal Electronics with Advanced Capabilities in Near-Field Communication. *small* **11**, 906-912 (2015).

11. Norton JJ, Lee DS, Lee JW, *et al.* Soft, curved electrode systems capable of integration on the auricle as a persistent brain–computer interface. *Proceedings of the National Academy of Sciences* **112**, 3920-3925 (2015).

12. Xu B, Akhtar A, Liu Y, *et al.* An Epidermal Stimulation and Sensing Platform for Sensorimotor Prosthetic Control, Management of Lower Back Exertion, and Electrical Muscle Activation. *Advanced Materials*, n/a-n/a (2015).

13. Xu S, Zhang Y, Jia L, *et al.* Soft microfluidic assemblies of sensors, circuits, and radios for the skin. *Science* **344**, 70-74 (2014).

14. Webb RC, Bonifas AP, Behnaz A, *et al.* Ultrathin conformal devices for precise and continuous thermal characterization of human skin. *Nature materials* **12**, 938-944 (2013).

15. Webb RC, Pielak RM, Bastien P, *et al.* Thermal transport characteristics of human skin measured in vivo using ultrathin conformal arrays of thermal sensors and actuators. *PloS one* **10**, e0118131 (2015).

16. Huang X, Huanyu C, Kaile C, *et al.* Epidermal Impedance Sensing Sheets for Precision Hydration Assessment and Spatial Mapping. *Biomedical Engineering, IEEE Transactions on* **60**, 2848-2857 (2013).

17. Huang X, Yeo W-H, Liu Y, *et al.* Epidermal Differential Impedance Sensor for Conformal Skin Hydration Monitoring. *Biointerphases* **7**, 52 (2012).

18. Yeo W-H, Kim Y-S, Lee J, *et al.* Multifunctional Epidermal Electronics Printed Directly Onto the Skin. *Advanced Materials* **25**, 2773-2778 (2013).

19. Dagdeviren C, Shi Y, Joe P, *et al.* Conformal piezoelectric systems for clinical and experimental characterization of soft tissue biomechanics. *Nature materials* **14**, 728-736 (2015).

20. Dagdeviren C, Su Y, Joe P, *et al.* Conformable amplified lead zirconate titanate sensors with enhanced piezoelectric response for cutaneous pressure monitoring. *Nature communications* **5**, (2014).

21. Webb RC, Ma Y, Krishnan S, *et al.* Epidermal devices for noninvasive, precise, and continuous mapping of macrovascular and microvascular blood flow. *Science advances* **1**, e1500701 (2015).

22. Hu Y, Kim EG, Cao G, *et al.* Physiological acoustic sensing based on accelerometers: A survey for mobile healthcare. *Annals of biomedical engineering* **42**, 2264-2277 (2014).

23. Pasterkamp H, Kraman SS, Wodicka GR. Respiratory sounds: advances beyond the stethoscope. *American journal of respiratory and critical care medicine* **156**, 974-987 (1997).

24. Titze IR. The physics of small-amplitude oscillation of the vocal folds. *The Journal of the Acoustical Society of America* **83**, 1536-1552 (1988).

25. Zeng F-G, Fu Q-J, Morse R. Human hearing enhanced by noise. *Brain research* **869**, 251-255 (2000).

26. Dunn F, Hartmann W, Campbell D, *et al. Springer handbook of acoustics*. Springer (2015).

27. Gelfand SA. *Essentials of audiology*. New York: Thieme, 2007 (2007).

28. Postolache O, Girão P, Postolache G. Seismocardiogram and Ballistocardiogram Sensing. *Advanced Instrument Engineering: Measurement, Calibration, and Design: Measurement, Calibration, and Design*, 223 (2013).

29. Castiglioni P, Faini A, Parati G, *et al.* Wearable Seismocardiography. (2007).

30. Inan OT, Migeotte PF, Park KS, *et al.* Ballistocardiography and Seismocardiography: A Review of Recent Advances. *IEEE Journal of Biomedical and Health Informatics* **19**, 1414-1427 (2015).

31. Rienzo MD, Meriggi P, Rizzo F, *et al.* A wearable system for the seismocardiogram assessment in daily life conditions. IEEE (2011).

32. Salerno DM, Zanetti J. Seismocardiography for monitoring changes in left ventricular function during ischemia. *Chest* **100**, 991-993 (1991).

33. Zanetti JM, Poliac MO, Crow RS. Seismocardiography: waveform identification and noise analysis. (1991).

34. Zanetti JM, Salerno DM. Seismocardiography: a technique for recording precordial acceleration. (1991).

35. He DD, Winokur ES, Sodini CG. A continuous, wearable, and wireless heart monitor using head ballistocardiogram (BCG) and head electrocardiogram (ECG). IEEE (2011).

36. Octavian P, Pedro G, Gabriela P. Seismocardiogram and Ballistocardiogram Sensing. In: *Advanced Instrument Engineering: Measurement, Calibration, and Design* (ed^(eds). IGI Global (2013).

37. Elliott LV, Packard RG, Kyrazis DT. Acceleration Ballistocardiography Design, Construction, and Application of a New Instrument. *Circulation* **9**, 281-291 (1954).

38. Lee CH, Ma Y, Jang KI, *et al.* Soft Core/Shell Packages for Stretchable Electronics. *Advanced Functional Materials* **25**, 3698-3704 (2015).

39. Debbal S, Bereksi-Reguig F. Computerized heart sounds analysis. *Computers in biology and medicine* **38**, 263-280 (2008).

40. Titze IR, Martin DW. Principles of voice production. *The Journal of the Acoustical Society of America* **104**, 1148-1148 (1998).

41. Baken RJ, Orlikoff RF. *Clinical measurement of speech and voice*. Cengage Learning (2000).

42. Laugier P, Haïat G. Introduction to the physics of ultrasound. In: *Bone quantitative ultrasound* (ed^(eds). Springer (2011).

43. Vermarien H, Van Vollenhoven E. The recording of heart vibrations: a problem of vibration measurement on soft tissue. *Medical and Biological Engineering and Computing* **22**, 168-178 (1984).

44. Szabo TL, Wu J. A model for longitudinal and shear wave propagation in viscoelastic media. *The Journal of the Acoustical Society of America* **107**, 2437-2446 (2000).

45. Szabo TL. Time domain wave equations for lossy media obeying a frequency power law. *The Journal of the Acoustical Society of America* **96**, 491-500 (1994).

46. Müller TM, Gurevich B. Wave-induced fluid flow in random porous media: Attenuation and dispersion of elastic waves. *The Journal of the Acoustical Society of America* **117**, 2732-2741 (2005).

47. Chuo Y, Marzencki M, Hung B, *et al.* Mechanically flexible wireless multisensor platform for human physical activity and vitals monitoring. *Biomedical Circuits and Systems, IEEE Transactions on* **4**, 281-294 (2010).

48. Hubbert L, Sundbom P, Loebe M, *et al.* Acoustic analysis of a mechanical circulatory support. *Artificial organs* **38**, 593-598 (2014).

49. Kaufmann F, Hörmandinger C, Stepanenko A, *et al.* Acoustic spectral analysis for determining pump thrombosis in rotary blood pumps. *ASAIO Journal* **60**, 502-507 (2014).

50. Hasin T, Deo S, Maleszewski JJ, *et al.* The role of medical management for acute intravascular hemolysis in patients supported on axial flow LVAD. *ASAIO Journal* **60**, 9-14 (2014).

51. Kawahito K. Transformation of vibration signals in rotary blood pumps: the diagnostic potential of pump failure. *Journal of Artificial Organs* **16**, 393-396 (2013).

52. Yost GL, Royston TJ, Bhat G, *et al.* Acoustic Characterization of Axial Flow Left Ventricular Assist Device Operation In Vitro and In Vivo. *ASAIO Journal* **62**, 46-55 (2016).

53. Deng Y, Patel R, Heaton JT, *et al.* Disordered speech recognition using acoustic and sEMG signals. (2009).

54. Erzin E. Improving throat microphone speech recognition by joint analysis of throat and acoustic microphone recordings. *Audio, Speech, and Language Processing, IEEE Transactions on* **17**, 1316-1324 (2009).

55. Jorgensen C, Binsted K. Web browser control using EMG based sub vocal speech recognition. IEEE (2005).

56. Mainardi E, Davalli A. Controlling a prosthetic arm with a throat microphone. IEEE (2007).

57. Wand M, Schulte C, Janke M, *et al.* Array-based Electromyographic Silent Speech Interface. (2013).

58. Jorgensen C, Dusan S. Speech interfaces based upon surface electromyography. *Speech Communication* **52**, 354-366 (2010).

59. Dupont S, Ris C, Bachelart D. Combined use of close-talk and throat microphones for improved speech recognition under non-stationary background noise. (2004).

60. Graciarena M, Franco H, Sonmez K, *et al.* Combining standard and throat microphones for robust speech recognition. *Signal Processing Letters, IEEE* **10**, 72-74 (2003).

61. Heracleous P, Even J, Ishi CT, *et al.* Fusion of standard and alternative acoustic sensors for robust automatic speech recognition. IEEE (2012).

62. Lee K-S. SNR-adaptive stream weighting for audio-MES ASR. *Biomedical Engineering, IEEE Transactions on* **55**, 2001-2010 (2008).

63. Betts BJ, Binsted K, Jorgensen C. Small-vocabulary speech recognition using surface electromyography. *Interacting with Computers* **18**, 1242-1259 (2006).

64. Hinton G, Deng L, Yu D, *et al.* Deep neural networks for acoustic modeling in speech recognition: The shared views of four research groups. *Signal Processing Magazine, IEEE* **29**, 82-97 (2012).

65. Moss R, Halpern W. Elastic and viscous properties of resting frog skeletal muscle. *Biophysical journal* **17**, 213 (1977).

66. Boll SF. Suppression of acoustic noise in speech using spectral subtraction. *Acoustics, Speech and Signal Processing, IEEE Transactions on* **27**, 113-120 (1979).

## 4.10 Figures

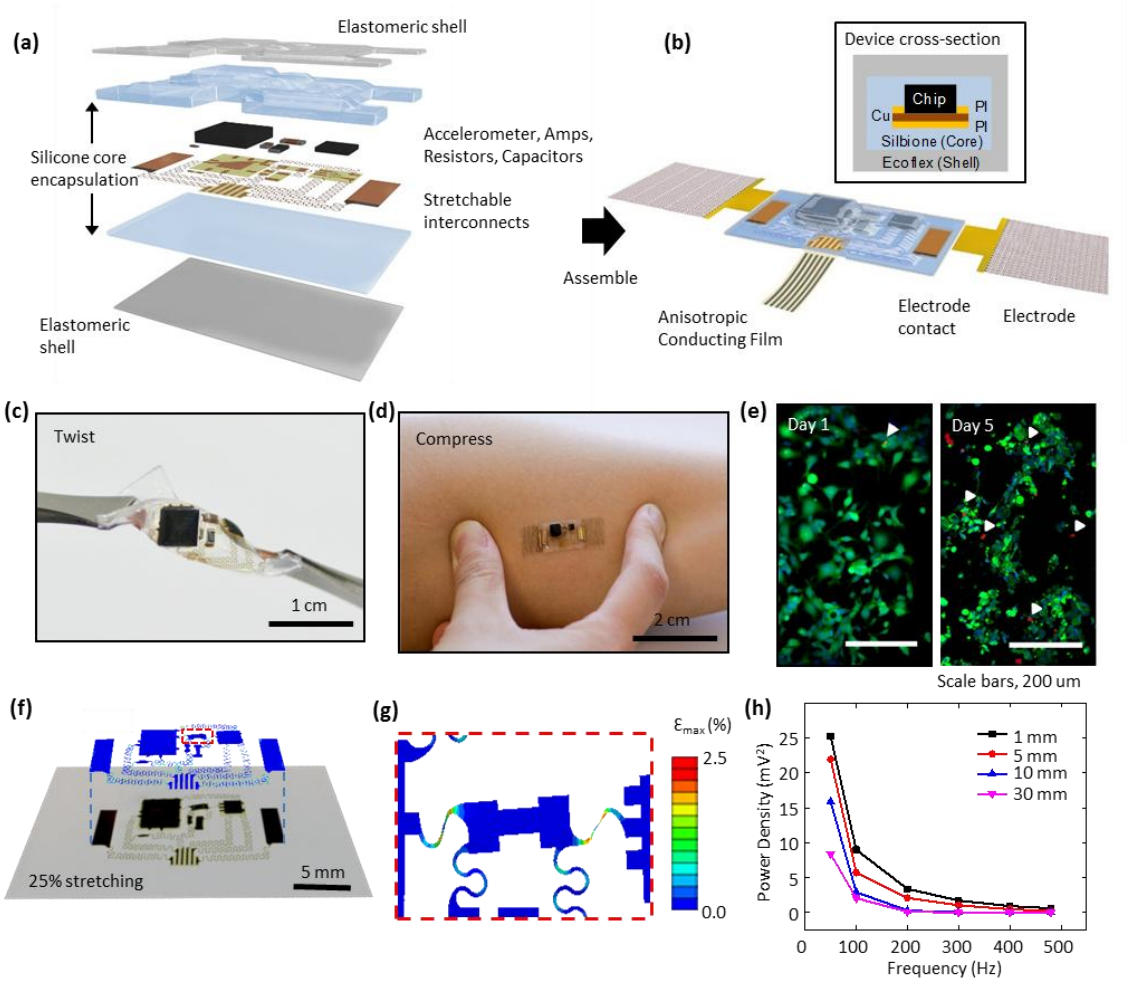


**Figure 4.1 Schematic illustration of an epidermal mechano-acoustic-electrophysiological measurement device.** (a) Exploded view diagram of the overall design structure of the system. (b) Illustration of the assembled device and its interface with soft EP measurement electrodes and flexible cable for power supply and data acquisition. A cross sectional view appears in the upper inset. (c) Device held by tweezers in a twisted configuration. (d) Device mounted on skin while compressed by pinching. (e) Fluorescence micrographs of cells cultured on the surface of a device to illustrate its biocompatibility. Green and red regions correspond to live and dead cells, respectively. The white arrows highlight the latter. (f) Overlay of optical image and finite element simulation results for a device under bi-axial stretching to a strain of 25%. (g) Magnified view of modeling results for the part of the interconnect structures that experiences the highest strain. (h) Vibrational response summarized in a plot of spectral power measured while mounted on a layer of chicken breast, to simulate tissue, on a vibration source.

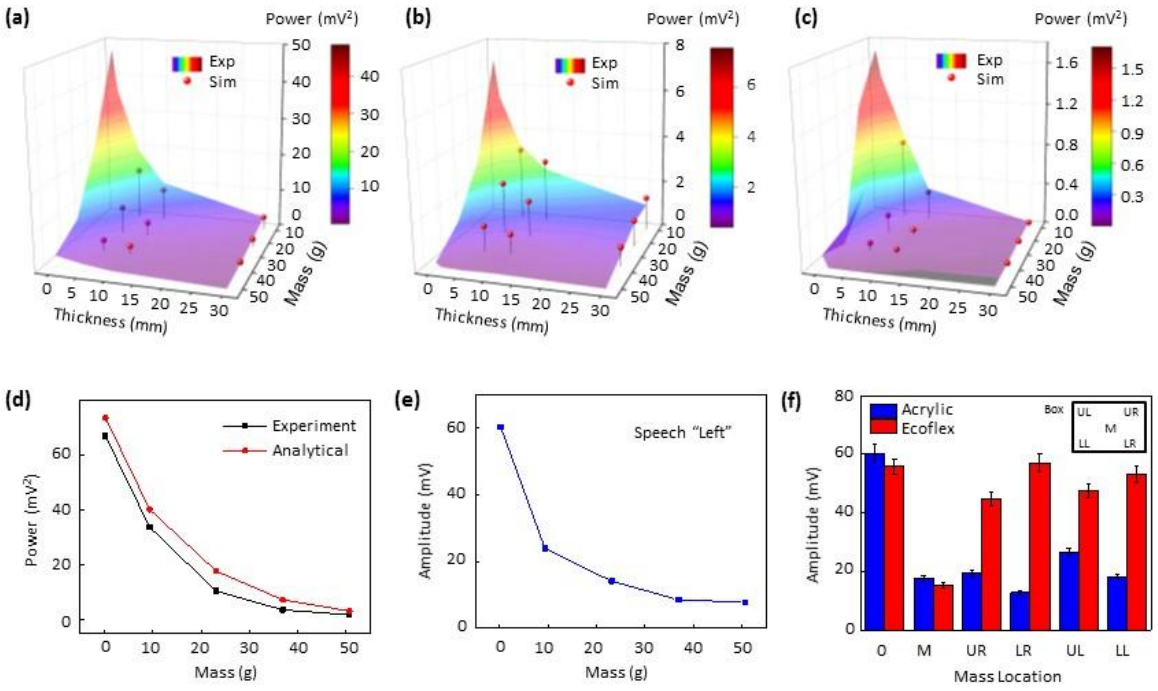


**Figure 4.2 Summary of the experimental and computational studies of the effects of device mass, modulus, tissue thickness and signal frequency on measured mechano-acoustic signals.** Experimental spectral power and simulation results associated with the mechano-acoustic response of a device mounted in an acrylic box placed on a tissue sample on a vibrational source at frequencies of (a) 50 Hz, (b) 100 Hz, (c) 200 Hz. (d) Comparison of measured (experiment) and computed (analytical) dependence of spectral power on mass. (e) Measured maximum signal amplitude recorded with a device mounted on the neck as the subject said the word "left" as a function of mass of the device. (f) Amplitude measured using a device in a rigid box and on a thin substrate of Ecoflex, as a function of spatial location of the added mass.

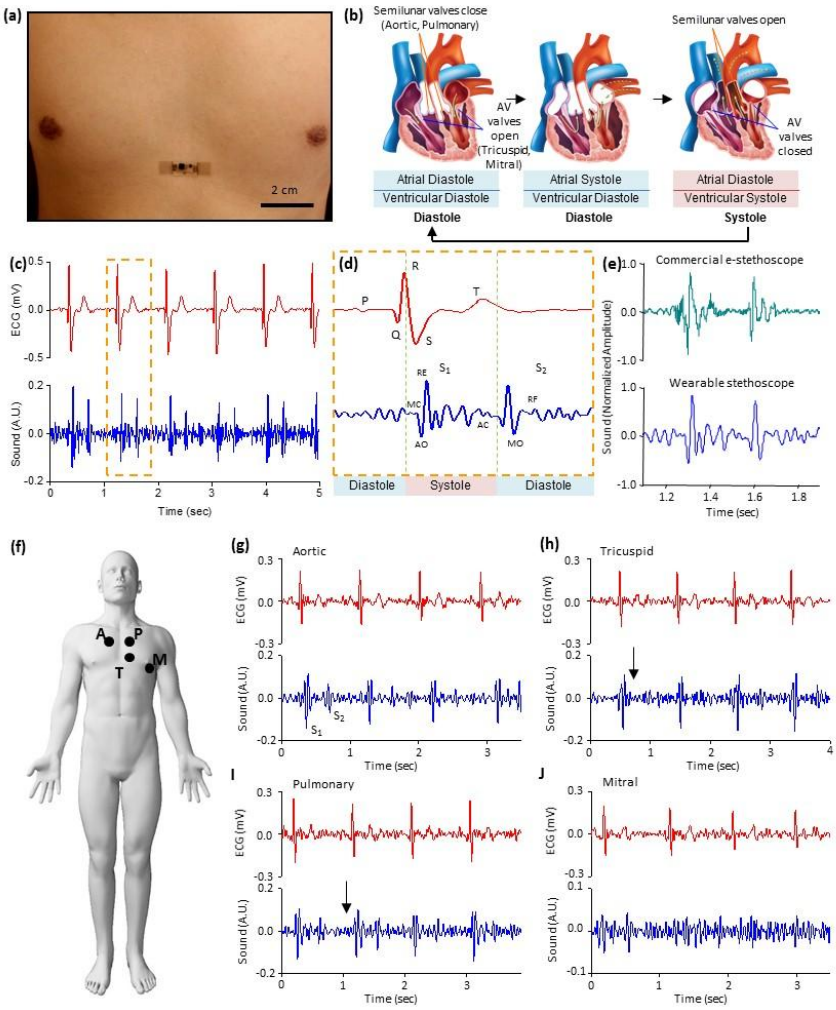


**Figure 4.3 Applications of mechano-acoustic-electophysiological sensing with an epidermal device in diagnosing cardiovascular health status.** (a) Image of an epidermal device mounted on the chest. (b) Schematic diagram of cardiac cycle: (left) artrial and ventricular diastole, (middle) artrial systole and ventricular diastole, (right) ventricular systole and atrial diastole. (c) Plot of ECG (top) and heart sound (bottom) signals measured simultaneously. d) Magnified view of ECG (top) and heart sound (bottom) signals measured in (c), MC: Mitral valve closure, AO: Aortic valve opening, RE: Rapid ventricular ejection, AC: Aortic valve closure, MO: Mitral valve opening, RF: Rapid ventricular filling. (e) Comparison of heart sound signals measured using a commercial electronic stethoscope and the reported device. (f) Schematic illustration of the measurement site: A – Aortic, P – Pulmonary, T – Tricuspid, M – Mitral. A representative measurement from 78 year-old female patient with diagnosed mild pulmonary and tricuspid regurgitation at (**g**) aortic site, (**h**) tricuspid site, (**i**) pulmonary site, and (**j**) mitral site.

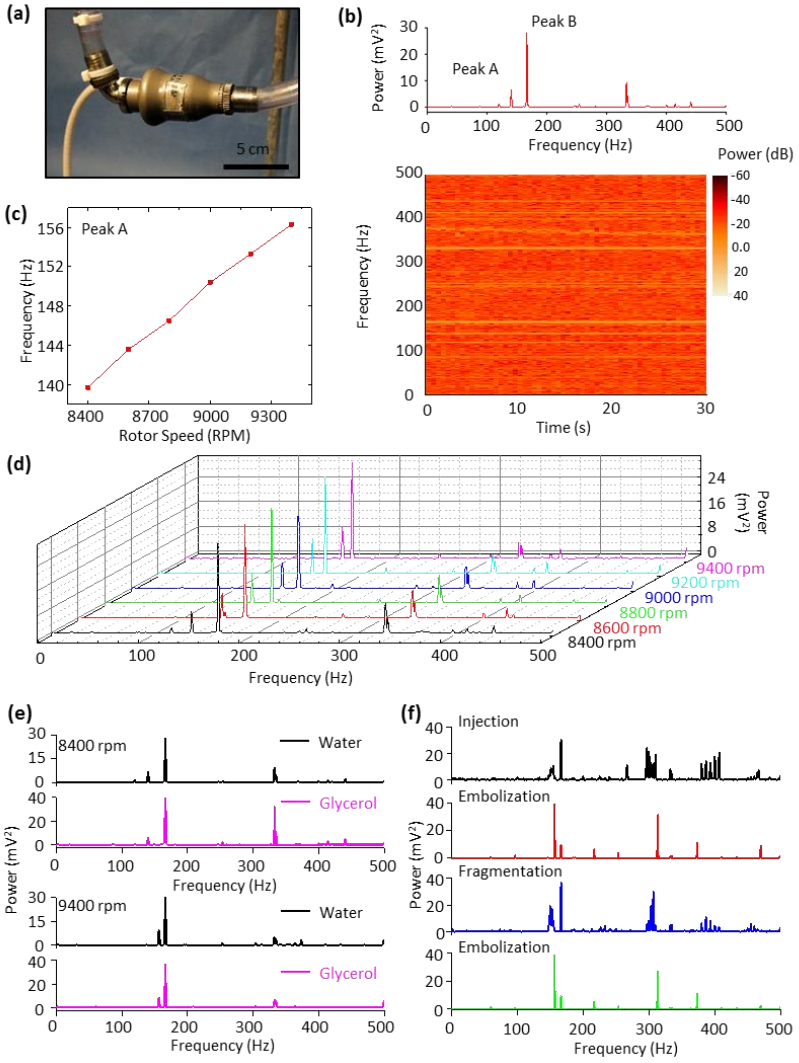


**Figure 4.4 Applications of mechano-acoustic sensing with an epidermal device in diagnosing ventricular assisted device (VAD) operation.** (a) Image of the experimental circulation loop with the device mounted on the VAD (HeartMate II). (b) Fast-Fourier Transform (FFT) of the vibration response (top) and spectrogram (bottom) associated with operation of the VAD at 8400 RPM in a water circulation loop. (c) FFT spectral power of the vibration response for operating frequencies between 8400 RPM to 9400 RPM. Distinctive changes with VAD speed occur only on the peak around 150 Hz. (d) Comparison of vibrational response in a circulation loop with water and with glycerol at 8400 RPM (top) and 9400 RPM (bottom). (e) Demonstration of changes in acoustic signature associated with circulation of a 500 μL blood clot in the glycerol loop during stages of initial injection of blood clot, first few circulation passes without decomposition, subsequent complete decomposition, and circulation of tiny blood clots.

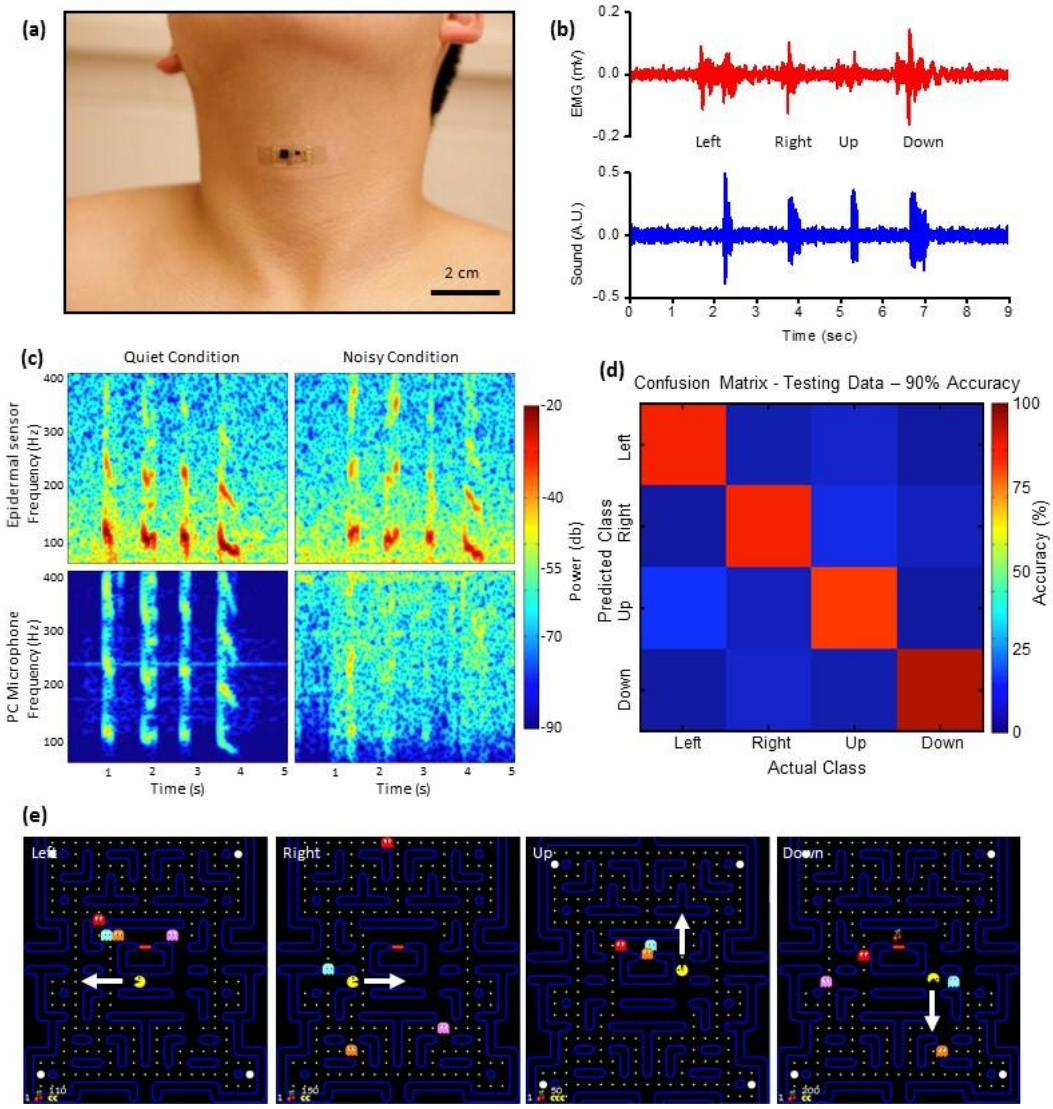


**Figure 4.5 Applications of mechano-acoustic sensing with an epidermal device for speech recognition.** (a) Image of an epidermal device mounted on the vocal cords. (b) Plot of EMG (top) and vocal vibrational (bottom) signals measured simultaneously from the neck. (c) Comparison of speech recorded with the reported device (top row) and with an external microphone (bottom row). The left and right columns represent recording made in quiet and noisy conditions, respectively. (d) Confusion matrix that describes the performance of the speech classification; the number in the box and the color bar show the number of samples in the classification test. (e) Demonstration of speech recognition and classification in a Pac-man game with left, right, up and down instruction.

# CHAPTER 5

# EPIDERMAL RADIO FREQUENCY ELECTRONICS FOR WIRELESS POWER TRANSFER

Significant portions of this chapter were published as "Epidermal Radio Frequency Electronics for Wireless Power Transfer," Xian Huang[†], Yuhao Liu[†], Gil Woo Kong, Jung Hun Seo, Kyung-In Jang, Yinji Ma, Xue Feng, Shimin Mao, Qiwen Chen, Daizhen Li, Chuxuan Wang, Hank Liu, Jonathan A. Fan, Dwipayan Patnaik, Limei Tian, Giovanni A. Salvatore, Zhenqiang Ma, Yonggang Huang, John A Rogers, *Nature Microsystems and Nanoengineering* (2016). Manuscript is accepted and in press. ([†] equal contribution)

## 5.1 Introduction

Recent research and development in wearable technologies has yielded a broad range of devices with applications in daily health monitoring[1], activity tracking[2, 3], data logging[4], human machine interfaces[5, 6] and clinic diagnostics[7, 8]. Future advances in this rapidly evolving area will improve processes for delivering health care[9] and for reshaping personal lifestyles to enhance well being[10]. A dominating challenge in the realization of comfortable, non-irritating interfaces with the body follows from the current use of rigid or semi-rigid substrates and packages directly adopted from those found in non-wearable consumer electronics[1]. The result is a mechanical and geometrical mismatch with the soft and curvilinear textures of the body, thereby necessitating the use of fixtures (wrist bands, head bands, chest straps, or glasses)[11] or strong adhesives for mounting. Additional negative consequences include inconsistent, unreliable skin coupling, discomfort associated with contact pressure and interfacial shear and frictional forces, and constraints in locations for body integration, thereby adversely affecting the user experiences and the sensor accuracy. Such circumstances motivate the development of wearable devices that

offer improved compatibility with the skin, at the level of the materials, the geometries, the mass density, the mechanical properties and the air/water permeability[12, 13]. Recent work[14, 15, 16, 17] establishes various routes to ultrathin, soft electronic technologies, sometimes referred to as epidermal electronic systems (EES). Such EES have physical properties that approximate those of the epidermis, integrating both passive sensing functions[18, 19] and active modalities[20] for daily healthcare monitoring with maximum comfort and high sensing precision.

The practical feasibility of EES in continuous monitoring outside of hospital or laboratory settings demands unusual schemes for power supply because batteries[21] and external connections[15, 20, 22, 23] are unacceptable. Although recent research demonstrates options in stretchable batteries[24] and in miniaturized platforms for harvesting energy from incident light[25], thermal gradients[26], mechanical motions[27], and near-field electromagnetic (EM) waves[28,29], additional options could be useful. Possibilities include inductive coupling[30, 31], mid-field microwave-propagation[32] and far-field radio-frequency (RF) harvesting[33, 34], each of which exists in some form as wireless sources of power for conventional biomedical devices. The third approach is particularly attractive when implemented in commonly available industry-science-medical frequency bands, due to its versatility in power transfer and operation frequency, and its long range transmission capabilities. Conventional hardware for such devices[28, 34, 35, 36, 37] demands, however, commercial-off-the-shelf (COTS) components that are challenging to render into forms suitable for chronic integration with the skin. An epidermal embodiment would, therefore, be attractive.

Here, we introduce materials and integration concepts for such a technology, in which the functional components exploit ultrathin active and passive elements, configured for soft, elastic mechanical properties. These wireless RF power systems use a laminated construction that

facilitates optimization of analog performance, with capabilities for robust operation under significant levels of mechanical deformation. Detailed studies of the device characteristics, including effects of RF absorption in the human body, define the key design considerations. Wireless operation of power small-scale LEDs in full epidermal platforms mounted on the skin of the arm and placed at distances of several meters from an RF transmitter and of several centimeters from a standard cell phone, both with and without device deformation, illustrate the performance. The results establish an attractive option for wireless power delivery to epidermal systems of various types, for both healthcare and non-healthcare applications alike.

## 5.2 Modularization Approach and Soft Contact Lamination

Standard, monolithic strategies in design and fabrication limit the ability to optimize performance or conduct parametric studies of the analog RF circuits introduced here, where variability that arises from the uncertain dielectric properties of the surrounding biological tissues can cause significant complications. This circumstance demands a modularized approach to assembly, in which component fabrication and characterization occurs before collective integration, via soft-contact lamination processes described in **Supplementary Note 1**, to yield functional systems for performance evaluation. This lamination can be conducted in a reversible mode for test/evaluation, or an irreversible for final device assembly. The latter relies on cold welding that occurs upon contact between exposed gold electrode pads on opposing surfaces[40]. One reversible variant involves the formation of a blocking self-assembly monolayer (SAM) on the gold to prevent cold welding. In addition to control over the interface chemistries, we find that the kinetics of cold welding differ depending on the mechanical properties and geometries of the substrates. In all cases, lamination occurs without external pressure, in a soft mode, in which the "wetting" properties associated with low modulus elastomeric substrates[38] and van der Waals

forces[38, 39] drive contact between multiple, thin, soft electronic components to establish contacts. Although previously demonstrated in the context of organic electronic devices[38, 40], this same strategy works well with inorganic stretchable systems, as illustrated in studies of basic test structures. Here, gold-gold cold welding that follows from contact at exposed pads yields low electrical resistance and robust operation under stretching. Observation of the gold-gold interface (figure 5.1b) reveals homogeneous welding and intimate electrical contact.

## 5.3 Wireless Power Harvester Circuit Design

Figure 5.1a shows a modularized version of a completed device that includes an impedance matcher connected to a loop antenna, and a voltage doubler combined together by the soft-contact lamination technique described above. The load, for purposes of functional demonstration, is a small-scale LED (figure 5.1b). Each component incorporates stacked ultrathin layers of metals, polymers, and semiconducting materials (figure 5.1e) in open-mesh, serpentine layouts to yield soft, elastic mechanical properties for skin-mounted applications, using design principles described elsewhere[41]. Specifically, these components have total thicknesses between 6 m and 10 m, they exhibit effective linear elastic moduli of ~60 kPa for strains up to 6 %, they have area mass densities of ~10 mg/cm$^2$ and thermal masses of ~7.6 mJ/cm$^2$/K, all of which are comparable to corresponding properties of the epidermis itself[41, 42]. Modularization enhances the system-level yields, and offers the ability to explore various combinations of components with different electrical properties and functions.

The overall device occupies an area of 5.1x3.9 cm$^2$, dominated by the dimensions of the antenna. The inner area of the loop (4.2x3.1 cm$^2$) defines the space for the other components. The antenna consists of circular serpentine metallic mesh structures with inner radii of 340 m and outer radii of 440 m. The impedance matcher is a LC resonator. The inductor consists of a 3

turn square coil with traces that have 70 m widths, inner lengths of 130 m and outer lengths of 570 m. The capacitor uses a parallel plate design with a serpentine layout, in which Parylene-C (1 m) serves as the dielectric. The length of each serpentine electrode is ~1.8 mm. The total number of electrodes lies between 2 to 16, thereby providing different capacitances. The impedance matcher forms a low pass filter circuit with the first capacitor in a voltage doubler, and matches the impedance between the voltage doubler and antenna. The voltage doubler contains two p-intrinsic-n (PIN) diodes and two capacitors that each use 10 electrodes with an average length of ~ 0.8 mm, and Parylene-C (1 m) as the dielectric. The wedge shaped PIN diodes each cover an area of ~0.2mm$^2$ and use single crystalline nanomembranes of silicon (Si NMs) as the semiconductor. The half-wave rectification provided by the doubler converts an AC voltage output at the impedance matcher into a DC voltage with twice the magnitude, for powering the load circuit. Specifically, the PIN diodes function as switches to allow voltage to accumulate on $C_1$ only during the negative cycle of the input voltage. Voltage doubling on $C_2$ results from these use of $C_1$ as an additional voltage source during the positive cycle of the input voltage. In addition, $C_2$ reduces fluctuations in the output voltage. The small-scale red LED that serves as the load is a de-packaged surface-mounted device (Rohm, PICOLED SML-P11).

Modularized assembly begins with transfer printing of the voltage doubler registered to alignment marks on a membrane of polydimethylsiloxane (PDMS, Dow Corning, Sylgard 184; 20 m in thickness) that supports the loop antenna. The impedance matcher then laminates between the antenna and the doubler. Attachment of the load circuit on the other end of voltage doubler completes the process (figure 5.1c). Slight variations in the impedance match between the loop antenna and voltage doubler demand pre-integration tests that involve temporarily attaching impedance matchers with various capacitance values on a separate silicone substrate as

a test platform (Ecoflex, Smooth-on, thickness: 500 m). Reversible lamination enables characterization of the power transfer efficiency with various combinations of matchers in different dielectric environments (e.g. in air or on skin). The matcher that yields maximum output from the LED is irreversibly laminated, without silicone substrate, to the existing loop antenna and voltage doubler on the PDMS membrane together with a load circuit containing the LED (figure 5.1d). Advanced mechanical design considerations[17] yield characteristics that, as supported by observation under scanning electron microscope (SEM) using a skin replica (Dragon skin, Smooth-on), enable the PIN diodes and capacitor traces to follow the topography of the skin (figure 5.1f and 5.1g), indicating a high level of compliance and an ability for intimate skin contact.

## 5.4 Components Performance

Measurements of the voltage doubler involve placement of the contact pads against a pair of probes connected to a RF signal generator, while another pair of probes connects the output near capacitor $C_2$ to a high-speed oscilloscope. This setup determines the open-circuit voltage with variable frequency input at powers of ~100 mW. As an example, three voltage doublers fabricated in a single batch yield voltage levels ranging from 0.8 V at 500 MHz to 0.3 V at 1 GHz. The modularized approach allows selection of devices with performance finely matched to optimize overall performance.

The PIN diodes in the doublers incorporate single-crystalline nanomembranes of silicon (SiNMs), with switching speeds and current densities that meet requirements in high frequency power applications. Wedge shaped diodes (figure 5.2a) with similar intrinsic region lengths (7 m) but with decreasing surface areas at 0.40, 0.15 and 0.17 $mm^2$ respectively for Diode 1 (D1), Diode 2 (D2) and Diode 3 (D3) characterized through contacts to metal pads (Cr/Au, 10/300nm

thickness) in a ground-signal-ground (GSG) reveal current-voltage (I-V) responses that match those from simulation results (Silvaco). The threshold voltages are 0.7 V, independent of design; the current levels (1.8, 1.6, and 1.4 mA at 2.0 V respectively for D1, D2 and D3) scale with surface areas of the diodes (figure 5.2b). The junction capacitances are 0.40, 0.32, and 0.13 pF, respectively for D1, D2, and D3 at 100 mW input power, extracted using equivalent circuit models[43] (figure 5.2c and **Supplementary Note 3**), and are proportional to the surface areas. The junction resistances vary from 40.9, 69.0 to 120.8 Ω and are inversely proportional to area (figure 5.2d). D2 offers a favorable balance between junction capacitance and resistance. Rectification of RF signals at 100 MHz, 700 MHz and 2.4 GHz in a half-wave circuit design (figure 5.2e) yields voltage magnitudes of ~0.7 V, ~0.8 V and ~0.5 V respectively. The frequency dependence follows from variations in the impedance of the diode and the matching between the diode and the test setup. Measuring the scattering parameters associated with RF signals that have a DC bias at the input, and then decoupling this DC component at the output yields the switching speeds. The diode shows switching capability from conducting to non-conducting states up to 2.0 GHz, indicated by an increased S21 parameter with bias voltage levels larger than 0.5 V, and a crossing point at 2.0 GHz (figure 5.2d). Higher current levels in forward bias are possible with diodes that have rectangular shapes, but increased resistance associated with the correspondingly larger intrinsic areas can lead to high temperatures during operation, and cause device failure.

Maximum conversion efficiencies of power received by the antenna to DC output by the voltage doubler can be realized by comparative analysis of performance achieved with impedance matchers (labeled from M1 to M6) that offer different capacitance values to compensate for different dielectric environments (figure 5.3a). The different capacitances,

achieved by changing the numbers of serpentine parallel-plate capacitors, lead to resonant frequencies between 1 GHz to 700 MHz (figure 5.3b). Operation while performing thermal infrared (IR) imaging can reveal heating and associated losses in the matchers. As shown in figure 5.3c, temperature increases ($\Delta T \sim 42$ ℃ and 34 ℃) occur at the inductors on M1 and M4, with little heating in the diodes (~30 ℃), consistent with ineffective coupling. Comparatively, small temperature changes occur in M6, indicating high energy conversion efficiency.

## 5.5 Simulations of the Specific Absorption Rate

Finite element modeling (Ansys HFSS) can quantify the specific absorption rate (SAR) in the human body during exposure under conditions similar to those used in RF power transfer experiments. For a transmission antenna operating at 15 W (figure 5.3d), electrical field distribution within a human body model was obtained at a distance (1.0 m) near the boundary of electromagnetic wave, which is considered as the strongest electric field in far field applications. The magnitude of the electrical field reaches a maximum near the eyes, which corresponds to the largest SAR value (~410 mW/kg). Three body positions indicated by L1 (equal to the level of the antenna), L2, and L3 further illustrate the spatial distribution of the SAR (figure 5.3d). The local SAR was ~124 mW/kg and 17.2 μW/kg in the front and back part of the model at L1 (figure 5.3e). The SAR in subcutaneous tissues such as fat and muscle experiences different levels of attenuation, determined by the dielectric properties of these tissue layers. The simulated SAR in all cases is much lower than the limits associated with FCC guidelines (1.6 W/kg)[44]. The skin directly underneath the device has some additional SAR from the loop antenna. Calculation from the Friis transmission equation shows a theoretical, ideal RF power available on the skin region at a distance of 1.5 m away from the transmission antenna (**Supplementary Note 4**). This power is largely absorbed by the loop antenna on the skin while only a small portion reflects on creating

SAR to the skin. Similarly, simulations of the electrical field distribution underneath the loop antenna reveals the largest field magnitudes near the locations of the antenna patterns. According to this simulation, the local SAR value associated with reflections from the loop antenna is 380 mW/kg (figure 5.3f), again smaller than the partial body FCC limit.

## 5.6 Antenna Design and Characterization

The epidermal loop antenna has an expected donut-shaped radiation pattern with maximum and minimum gain values in the plane and out of the plane of the antenna, respectively (figure 5.3g). The gain is ~2.89 dB in air at a frequency of 1.65 GHz, corresponding to the dip in the S11 curve (figure 5.3h). This gain decreases significantly (~-18.5 dB) upon placement on the skin, consistent with simulations that show the S11 parameter changes significantly due to the dielectric property of skin (figure 5.3h). The strong dependence of key properties on surrounding dielectric characteristics emphasizes the importance of modularization schemes for efficient impedance matching.

Measurements of the antenna under uniaxial and biaxial strain define variations in properties with physical deformation. In particular, a network analyzer can capture the magnitude and phase of the S11 parameters of the antennas under different strain levels up to 20%. The S11 parameters can be used to calculate the impedance of the antenna using equations in **Supplementary Note 5**.

For a loop antenna with dimensions of 5.1 × 4 $cm^2$, the fundamental resonance frequency in the magnitude of the S11 parameters decreases consistently from ~1.01GHz to 0.96 GHz for strains along x (5.1 cm) and in a biaxial mode. Only small changes (less than 6 MHz) occur for the same levels of strain along y (4 cm). The corresponding calculated impedances at these resonance frequencies vary only from 19 to 13 Ω, thereby illustrating stable performance under

mild stretching.

The small difference in the dependence of the impedance on stretching along x and y may be due to the elongated overall geometries, i.e. lengths of 5.1 and 4 cm in these two directions. Shifts in the fundamental resonance frequencies (~1.0 GHz) are smaller than those in the harmonic modes (~1.6 GHz). Additionally, stretching in one direction is accompanied by compression in the other direction, resulting in small area and circumference changes. Thus, the values of $R_r$, $R_L$, and $L$ undergo minimal changes according to **equation 4.4** to **4.7** (**Supplementary Note 5**), in which area and circumference play major roles in determining the impedance and resonance frequency of the antenna.

The response of a meander dipole antenna with strain provides a useful point of comparison. The anisotropic design of the dipole antenna suggests a distinct response of the S11 parameters and the impedance with stretching along the poles. Small frequency shifts in S11 parameters occur for strain along x (5.3 cm), while larger shifts accompany strains along y (2.0 cm) and in biaxial modes. As variation in effective length of the antenna in x direction is much smaller than in the effective length along y direction, the antenna properties show larger changes during y direction stretching.

The Q factor of the antennas is ~5.1. The impedance of the loop antenna can be first determined by considering an equivalent model that contains serially connected radiation resistance, loss resistance, and inductance. These components, as well as the overall impedance, can be determined by the **equation 4.1** to **4.3** (**Supplementary Note 5**).

## 5.7 Mechanical Properties

The fully integrated systems have high levels of flexibility and stretchability due to their

overall layouts (figure 5.4a) [16, 17], with an ability to accommodate extreme deformations of the skin, including uniaxial stretching (figure 5.4b), biaxial (figure 5.4c) stretching and squeezing (figure 5.4d). Mechanical simulations using finite element analysis techniques (ABAQUS) [45] indicate that for 20% uniaxial stretching in the x and the y directions, the strains in the electronic materials remain less than 2% (figure 5.4e and 5.4f), with the largest strains at the corners of the loop antenna. The calculated strains are lower than the fracture strain of copper (~5%), revealing that the total biaxial stretchability of the epidermal RF system is larger than 20 %. Assuming a yield strain of ~0.3 % in the copper, the elastic stretchability in both directions is ~6 %.

## 5.8 Radio-frequency Wireless Power Transfer

The systems operate effectively even during deformation, with stable power output under significant twisting and stretching (figure 5.5a**)** for both the loop and meander dipole antennas. Sufficient RF power can be captured for operation of an integrated LED in both static and stretched states (20% strain, repeated; figure 5.5b) for the case of a transmission antenna (700 – 2500 MHz; 11 dBi) emitting 15 W of RF power (~1.0 GHz) at distances of up to 1.5 m. A device mounted on a phantom skin substrate[46] and illuminated with similar RF power reveals only a small increase in temperature (~0.4 ℃ ; IR camera). Together with the SAR simulation results described above, this finding supports safe operation under FCC regulations. Under these conditions, the open circuit voltage of the RF system is ~8V in air (figure 5.5e) and ~6.5 V on skin (figure 5.5f), sufficient for operating circuits with simple sensing and communication functions[47]. A RF power transfer system integrated with a loop antenna can power an LED on the skin in continuous and pulsed mode for deeper skin penetration depth (figure 5.5d**)**. Devices can also be designed to allow similar operation based on the RF output of a cell phone antenna (AT&T, 850 MHz; Blackberry, 8520; figure 5.5c).

## 5.9 Conclusions

The results reported here establish the materials, designs and integration strategies for an epidermal wireless RF power transfer system. This option for battery-free operation complements other approaches, to add flexibility in system level design. Within exposure guidelines, sufficient power can be received for operating many different building block components needed in epidermal technologies, ranging from radios to sensors, memory devices and low power microprocessors. Further improvements in the harvesting capabilities will follow from advances in antenna designs to improve angular bandwidth and to reduce losses associated with RF coupling to the skin. Addition of some modest amount of storage, either in the form of supercapacitors or chip scale batteries, will help to eliminate effects of intermittency in the received power.

## 5.10 Fabrication and Methods

### Device Fabrication

The major processes involve fabricating separate functional components on a carrier wafer, releasing them for purposes of transfer printing temporarily to water soluble tapes, then to PDMS membranes, such that they can be integrated into modularized forms to complete the final systems. Fabrication of the voltage doubler starts with a silicon on insulator wafer (SOI; SOITEC) that is thermally oxidized to form a doping barrier layer (~300 nm). Photolithography and reaction ion etching (RIE; Plasma-Therm) defines a hard mask in the silicon dioxide in the geometry of the regions for doping. P-type doping occurs in a diffusion furnace (Intel) at 1100 ℃ with solid-state boron nitride as a dopant source (PDS, Saint-Gobain). N-type doping with phosphorus uses the same procedures. Immersion in hydrofluoric acid (HF, 49%, Transene

Company) removes the silicon dioxide masking layer. RIE (CS 1701, Nordson) creates an array of holes (3 m diameter; 50 m spacing) in the device silicon to facilitate undercut of the buried oxide by buffered oxide etching in HF, to form a released silicon nanomembranes (SiNMs) on the carrier wafer. Transfer printing with a poly(dimethylsiloxane) (PDMS; Sylgard 184, Dow Corning) stamp delivers the SiNMs onto a partially cured polyimide layer (PI; PI2545, HD Microsystems; 110 ℃ for 1 min) spin cast on a wafer with underlying, sacrificial coating of poly(methyl methacrylate) (PMMA 495, Microchem; 60 nm). Further curing of the PI film for 1 min at 110 ℃ separates the PDMS stamp from the SiNMs. Remove the PDMS stamp and full curing of the PI film (250 ℃ for 1 hour in $N_2$) with the SiNMs complete the transfer printing process. Photolithography and RIE then define wedge shapes in the SiNM to for the RF diodes. Metal bilayers (25/300 nm of chromium/gold) deposited by electron beam evaporation form electrical interconnects in geometries defined by photolithography. A layer of parylene forms a dielectric for the parallel plate capacitor with the same metallization. RIE defines via holes through the parylene at designed locations to allows the connection between the top and bottom layers of metal (Cr/Au, 25/500 nm in thickness) for the capacitor plates, defined by photolithography and wet chemical etching. An additional layer of polyimide encapsulates the voltage doubler; photolithography and RIE define the final device layout. Immersion in acetone at 100 ℃ removes the PMMA, to allow retrieval of the devices onto water soluble tape (Aquasol, New York) temporarily, then to silicone substrate. The fabrication details of other components appear in the **Supplemental Note 6**.

**RF Harvesting and Characterization**

Characterization uses a signal generator (Agilent N5181A, 100 kHz-6 GHz), power amplifier

(Empower 1119-BBM3K5KHM, 500 MHz - 2500 MHz), and wideband antenna (Wilson 204475, 700 MHz-2700 MHz). The signal generator defines the RF frequency and pulse waveform, while the amplifier boosts the signal by 48 dB to an output power of 15 W. The wideband antenna provides stable gain that varies only slightly around 11 dBi throughout the frequency band of 700 to 2500 MHz. Testing of the individual components occurs prior to assembly. For example, a network analyzer (Agilent E5062A, 300 kHz-3 GHz) yields the S parameters and impedance values of the loop antennas; an impedance analyzer (Agilent 4291A, 2MHz-1.8 GHz) reveals properties of the matchers. A setup uses two probes to inject 100 mW RF power into the voltage doubler from RF signal generator, and two additional probes connect with the output of the doubler to measure its open circuit voltage using an oscilloscope (Agilent DSO8104A, 1 GHz, 4 GSa/s).

**S-parameter Measurement**

Measurement of the S parameters of the diodes uses a network analyzer (Agilent E8364A 45 MHz–50 GHz), calibrated using a standard Short-Open-Load-Thru (SOLT) on-wafer probing kit for a frequency range of 45 MHz–50 GHz. The RF signal and DC bias are applied biases between 0 V to 3 V at a fixed RF power of -5 dBm to determine the insertion loss and together using a bias-tee (T). The measurements involve DC isolation characteristics of diodes. The diode transfer curves are simulated using Silvaco software.

**PIN Diode Rectification Test**

For measurement of the rectifying characteristics of the diodes, the Agilent 8648D Synthesized RF Signal Generator (9 kHz to 4 GHz) supplies the RF and DC combined signal and the RF

power amplifier (SPA-120-18-003-SMA, 18 dB gain broadband amplifier operating in the 100 MHz to 12 GHz frequency range) boosts the output power to 100 mW. The output RF characteristics are obtained the by the Wide-Bandwidth Oscilloscope (Agilent 86100A Infiniium DCA). The two systems share a 10 MHz reference signal to synchronize the phase. All systems are connected by RF cables (Gore cable, performed up to 50 GHz).

**Mechanical Simulation**

A commercial finite element analysis software (ABAQUS) allows computational study of the stretchability of the systems. The structures and materials used in four simulated components are combined to simplified models that facilitate simulation. The structures include 2 μm/1 μm of Cu/PI for the antenna, and 2 μm/1 μm/1 μm of PI/Au/PI for the voltage doubler, the matcher, and the load circuit. These layers are modeled by the composite shell element (S4R), while the silicone elastomer (PDMS, ~20 μm in thickness, with modulus ~60 kPa) and the skin (~1 mm in thickness, with modulus ~130 kPa[41]) is modeled by the hexahedron element (C3D8R)[45].

**SAR Simulation**

The simulation of SAR uses HFSS and a standard human body model that includes the major body organs and structures. To simplify the simulation, the model contains only three layers: skin, fat, and muscle. Calculations involve a panel antenna with a gain of 11 dBi and a supply power of 15 W placed 1.0 m away from the closed point of the human body model. The thickness of individual layers varies according to different body locations. The focus is on three representative locations indicated by L1 to L3 are (figure 5.3d). The simulation of SAR underneath the epidermal loop antenna (on a PDMS substrate with 20 m thickness) uses planar

layers of skin (2 mm in thickness), fat (2 mm), and muscle (10 mm). The power available at the loop antenna is calculated based on Friis transmission, as described in the supplemental materials, and is 34 mW (at 1.16 GHz ), with only 1.89 mW of reflected power.

## 5.11 Supplementary Information

### Supplementary Note 1: Soft-contact lamination

Methods in soft lamination are known to provide efficient electrical contacts in organic transistors[38, 40], solar cells[48], and carbon nanotube-based passive integrated devices[49]. A key feature is that, instead of conventional adhesives[50], mechanical compression bonding techniques[51], thermal annealing approaches[52], or surface chemistry modifications[53], this type of soft-contact lamination exploits the "wetting" properties that follow from low modulus elastomeric substrates, van der Waals forces[38, 39] and cold welding of thin gold films[54]. The results establish conformal, microscopic-scale electrical contacts in ambient environment.

*Reversible Approach*

This approach exploits only the "wetting" properties from low modulus elastomeric substrate, via van der Waals forces, to provide temporary low resistance electrical contact between two metal pads transfer-printed on silicone substrate. We use this method mainly for impedance matching tests between antennas and doublers, in which the matchers are transfer-printed on separate silicone substrates. The process begins with transfer-printing of an electronic component on a thin silicone substrate (PDMS, 20 m), then delivering an electronic component on another comparatively thicker silicon substrate (PDMS, 500 m). Treatment of the latter with ethanoethiol (Sigma Alrich) vapor for 5 to 10 s creates a self-assembled monolayer of alkyl thiolates at the gold-gold interface to prevent cold welding[54]. Alignment and lamination of the metal connector

areas in two circuit components spontaneously bring them into physical and electrical contact without external applied pressure and heat treatment. The roughness, cleanliness and surface chemistry of silicone substrate may affect electrical contact results. A large surface area of silicone substrate improves "wetting" and spontaneously attachment.

*Irreversible Approach*

The permanent construction of wireless RF power system by irreversible soft-contact lamination begins with the fabrication of individual circuit components on wafer substrates, and ends with integration of these components via intrinsically irreversible cold welding process. The assembly starts with transfer-printing an electronic component on a silicone substrate, similar to the reversible approach. Then, delivering an electronic component onto a temporary water soluble tape (Aquasol, cellulose), without silicone substrate, will be brought in contact with target device. Alignment of the circular metal pads in two circuit components brings them in physical and electrical contacts under ambient air pressure, room temperature, and the presence of volatile organic contaminants. With small applied contact pressure (< 10 to 20 $N/m^2$)[54, 55], layers of nanoscale metallic atoms based on same[56, 57, 58] or different [59, 60]materials can be bonded together. In the test structure, a 20 nm gold ultrathin film deposited on bonding pad surfaces formed the atomic layers; the underlying compliant elastomeric supports facilitate the atomic contact at gold-gold interface between bonding pads. This process allows fast surface diffusion of metal atoms, forming strong adhesion between two nanoscale metal layers in close contact.

**Supplementary Note 2: Antenna Design**

Loop antennas, which are used extensively in the HF through the UHF bands, meet the key

requirements for operation in the epidermal RF power transfer system. Meander dipole antennas are also of interest, due to the ease of adjusting their operating frequency by changing their lengths. Both types of antennas are considered electrically small, where the overall length is less than one tenth of the wavelength of the RF radiation at their resonant frequency. Although these antennas have low radiation efficiency, they are suitable as receiver antennas in the systems described here. Experimental characterization can be accomplished through measurements with a network analyzer. Finite element analysis software (HFSS) can be used to further explore the properties, including the radiation patterns.

The rectangular loop antenna has an effective length of *a* (3.5 cm) and an effective width of *b* (4.6 cm). Assume that a current $I=I_0e^{-i\omega t}$ flows uniformly around the loop, where $\omega$ is the angular frequency. For an observer at angles $(\theta,\phi)$ with respect to the z axis (in a spherical coordinate system with origin at the antenna), the unit wave vector has rectangular components.

$$\hat{k} = \sin\theta\cos\phi\hat{x} + \sin\theta\sin\phi\hat{y} + \cos\theta\hat{z} \qquad \textbf{(1.1)}$$

For a small loop, where *a* and *b* are much smaller than λ, the wavelength of the RF radiation, the electric field of the loop antenna can be expressed as

$$E = -\hat{\phi}k^2 I_0 ab\frac{e^{i(kr-\omega t)}}{cr}\sin\theta \qquad (0.8)$$

Where c is the speed of light. For a rectangular loop, the radiation pattern is

$$\frac{dP}{d\Omega} = \frac{8I_0^2\sin^2(\frac{ka}{2}\sin\theta\cos\phi)\sin^2(\frac{kb}{2}\sin\theta\cos\phi)}{\pi c\sin^2\theta\sin^2 2\phi} \qquad (0.8)$$

**Supplementary Note 3: Electrical analysis of SiNM diodes**

The diode in the voltage doubler adopts a PIN diode format. The dielectric relaxation frequency of the diode can be determined from the following equation:

$$f_{r,\mathrm{GHz}} = 1/(2\pi\varepsilon_0\varepsilon_R\rho_{\Omega-cm}) \tag{2.1}$$

Where $\varepsilon_0$ is the vacuum permittivity, $\varepsilon_r$ is the static permittivity of silicon and ρ is the resistivity of the silicon. The optimum operating frequency for the PIN diode is at least three times higher than the dielectric relaxation frequency. The performance of the PIN diode is determined by its i-region resistance $R_I$, junction resistance $R_j$, and junction capacitance $C_j$. The values of these parameters can be individually determined by the following equations. An expression for the i-region resistance of the PIN diode at high frequency is

$$R_I = 4V_T \sinh(\frac{W}{2L})[\tan^{-1}(\exp(\frac{W}{2L}) - \frac{\pi}{4})]\Big/ I_0 \approx \frac{W^2}{2\mu_{AP}\tau I_0} \tag{2.2}$$

$$R_J(f) = \frac{KT}{qI_0}\beta\tanh(\frac{W}{2L})\cos(\phi - \frac{\theta}{2}) \tag{2.3}$$

and

$$C_j = \frac{\varepsilon_0\varepsilon_R\pi D^2}{4W} \tag{2.4}$$

Where $D$ is the PIN diode diameter and $W$ is the i-region thickness. A PIN diode, designed for high frequency operation, is usually fabricated to have low capacitance because the reactance of the diode in the OFF condition must be large compared to the line impedance. The ratio of the PIN's area to thickness is adjusted to obtain the desired capacitance. The resistivity or doping level of the i-layer is not critical as long as it is greater than 20 - 50 Ohm-cm for operation at 1GHz. The transit time and the relaxation frequency requirements are easily obtained.

**Supplementary Note 4: SAR Simulation**

The power available at the loop antenna is calculated based on Friis transmission equation,

$$\frac{P_r}{P_t} = G_t G_r \left( \frac{\lambda}{4\pi L} \right)^2 \tag{3.1}$$

Where $P_t$ is the transmitted power, $P_r$ the received power, $G_t$ the transmit antenna gain, $G_r$ the loop antenna gain, $L$ is the distance between two antennas, and $\lambda$ the wavelength of the RF radiation. For present experiments, $P_t$ is 15 W, $G_t$ is 11 dBi and $G_r$ is -0.15 dBi for operation on skin as determined by simulation using HFSS. The result is that the power received by the loop antenna at a distance of 1.0 m from the transmit antenna is 0.034 W at a frequency of 1.16 GHz. Only a small part of the received power leaks into the surrounding environment through the loop antenna, the percentage of this part of emitted energy is determined by the reflection coefficient ($\Gamma$) of the antenna, which is 0.235 according to the simulation result from HFSS As a result, for 0.034 W input power, only 1.89 mW of power will be reflected.

**Supplementary Note 5: Antenna scattering parameter and impedance calculation**

The S11 parameters can be used to calculate the impedance of the antenna using the following equations:

$$R + jX = |S11|\cos\theta + j|S11|\sin\theta \tag{4.1}$$

$$Z_{\text{real}} = Z_0 \left( \left(1 - R^2 - X^2\right) \Big/ \left( \left(1-R\right)^2 + X^2 \right) \right) \tag{4.2}$$

$$Z_{\text{img}} = Z_0 \left( 2Xj \Big/ \left( \left(1-R\right)^2 + X^2 \right) \right) \tag{4.3}$$

in which, |S11| and θ are the magnitude and phase of the S11 parameters measured by the network analyzer. R and X are the real part and imaginary part of the S11 parameters, and $Z_{real}$ and $Z_{img}$ are the real part and imaginary part of the complex antenna impedance.

These components as well as the overall impedance can be determined using the following equations:

$$Z_{in} = R_r + R_L + j\omega L \tag{4.4}$$

$$R_r = 31200\left(S/\lambda^2\right)^2 \tag{4.5}$$

$$R_L = \frac{2(l_1 + l_2)}{2\pi a}\sqrt{\frac{\omega\mu}{2\sigma}} \tag{4.6}$$

$$L = \frac{\mu_0}{\pi}\left[l_2 \cosh^{-1}\frac{l_1}{2a} + l_1 \cosh^{-1}\frac{l_2}{2a}\right] \tag{4.7}$$

Where $R_r$ and $R_L$ are the radiation resistance and loss resistance of the loop antenna, $L$ is the inductance of the antenna. S is the area of the antenna, $l_1$ and $l_2$ and the length of the loop antenna in x and y direction, $a$ is the wire radius, $\omega$, $\mu$, $\sigma$ are angular frequency, permeability, and conductivity, respectively.

**Supplementary Note 6: Device Fabrication**

The RF energy system is an integrated system composed of an antenna, impedance matcher, voltage doubler, connector and an LED (PicoLED, SML-P11, Rohm Semiconductor). All modularized components involve different fabrication procedures, each starting with silicon wafers (University Wafers, 3”, 16-22 Ohm/cm) as bare substrates. Poylmethyl-methacrylate (PMMA, MicroChem, 495 A2) and polyimide (PI, HD Microsystems, PI2545) spin cast onto

these wafers serve as sacrificial layers whose elimination releases the completed components for integration onto an epidermal substrate.

Both the loop antenna and the load circuit are fabricated starting with a laminate (Microthin, Oak Mitsui Inc.) that contains a double stack of copper foil (5 μm and 17.5 μm in thickness) . Spin casting defines a film of polyimide (1 μm in thickness) on the side with the thin copper. The cured polyimide can be peeled, with the thin copper layer attached, from the thick copper layer and the releasing layer, for subsequent attachment onto a layer of PDMS spin-cast on a glass slide. The exposed thin copper layer is coated with a bilayer of 5/25 nm Ti/Au. Photolithography followed by metal etching defines the patterns of the loop antenna or the loop circuit. Another spin-casting process defines a layer of PI on the resulting patterns. Photolithography and RIE to define the overall patterns of the antenna and the load circuit. Removal of the photoresist mask completes the fabrication of these two structures. Retrieval onto the surface of a piece water soluble tape allows for further assembly and integration.

The impedance matching circuit uses the same type of copper laminate and methods similar to those described above for the loop antenna and the load circuit to define the bottom electrodes of the parallel plate capacitors and the coil. A layer of parylene (1 m) deposited on the circuit layer serves as a dielectric layer. Patterned RIE defines openings that can define electrical vias through the deposition and patterning of a bilayer of Cr/Au (5 nm/300 nm). The entire matching circuit is then covered with additional PI layer that is patterned to complete the device.

Assembly of the components to build working systems occurs on a thin (20 μm) layer of PDMS spin cast on a water soluble tape on a glass substrate. All components are coated with a bilayer of Ti/$SiO_2$ (5/40 nm). Exposure to UV induced ozone creates hydroxyl groups for permanent covalent –Si-O-O-Si- bonding at the contacting interfaces. Transfer printing of individual

components onto the PDMS occurs in order, starting with the antenna, voltage doubler, impedance matching circuit and load. Rinsing the resulting device with water allows the removal of water soluble tapes on the device. Transfer of the complete device to another water soluble tape on glass slide and seal the edges with scotch tape, followed by removal of the first tape, prepares the system for integration on the skin.

## 5.12 References


1. Pantelopoulos A, Bourbakis NG. A Survey on Wearable Sensor-Based Systems for Health Monitoring and Prognosis. *Systems, Man, and Cybernetics, Part C: Applications and Reviews, IEEE Transactions on* **40**, 1-12 (2010).

2. Paradiso R, Loriga G, Taccini N. A wearable health care system based on knitted integrated sensors. *Information Technology in Biomedicine, IEEE Transactions on* **9**, 337-344 (2005).

3. Korhonen I, Parkka J, van Gils M. Health monitoring in the home of the future. *Engineering in Medicine and Biology Magazine, IEEE* **22**, 66-73 (2003).

4. Yao J, Schmitz R, Warren S. A wearable point-of-care system for home use that incorporates plug-and-play and wireless standards. *Information Technology in Biomedicine, IEEE Transactions on* **9**, 363-371 (2005).

5. Jacko JA. *Human Computer Interaction Handbook: Fundamentals, Evolving Technologies, and Emerging Applications*. CRC press (2012).

6. Kawamoto H. *Cybernics - Wearable Robot Technology*. Springer Japan (2014).

7. Rodriguez-Villegas E, Chen G, Radcliffe J, Duncan J. A pilot study of a wearable apnoea detection device. *BMJ Open* **4**, (2014).

8. Kim J, *et al.* The Tongue Enables Computer and Wheelchair Control for People with Spinal Cord Injury. *Sci Transl Med* **5**, 213ra166 (2013).

9. Pentland A. Healthwear: medical technology becomes wearable. *Stud Health Technol Inform* **118**, 55-65 (2005).

10. Lymberis A. Smart wearable systems for personalised health management: current R&D and future challenges. In: *Engineering in Medicine and Biology Society, 2003. Proceedings of the 25th Annual International Conference of the IEEE* (ed^(eds) (2003).

11. Patel S, Park H, Bonato P, Chan L, Rodgers M. A review of wearable sensors and systems

with application in rehabilitation. *J Neuroeng Rehabil* **9**, 21 (2012).

12. Pang C, Lee C, Suh K-Y. Recent advances in flexible sensors for wearable and implantable devices. *J Appl Polym Sci* **130**, 1429-1441 (2013).

13. Rogers JA. Electronics for the human body. *J American Med Asso* **313**, 561-562 (2015).

14. Fan JA, *et al.* Fractal design concepts for stretchable electronics. *Nat Commun* **5**, (2014).

15. Jeong J-W, *et al.* Materials and Optimized Designs for Human-Machine Interfaces Via Epidermal Electronics. *Advanced Materials* **25**, 6839-6846 (2013).

16. Kim D-H, *et al.* Epidermal Electronics. *Science* **333**, 838-843 (2011).

17. Yeo W-H, *et al.* Multifunctional Epidermal Electronics Printed Directly Onto the Skin. *Adv Mater* **25**, 2773-2778 (2013).

18. Huang X, Yeo W-H, Liu Y, Rogers JA. Epidermal Differential Impedance Sensor for Conformal Skin Hydration Monitoring. *Biointerphases* **7**, - (2012).

19. Xian H, *et al.* Epidermal Impedance Sensing Sheets for Precision Hydration Assessment and Spatial Mapping. *Biomedical Engineering, IEEE Transactions on* **60**, 2848-2857 (2013).

20. Ming Y, *et al.* Silicon nanomembranes for fingertip electronics. *Nanotechnology* **23**, 344004 (2012).

21. Lee Y-H, *et al.* Wearable Textile Battery Rechargeable by Solar Energy. *Nano Lett* **13**, 5753-5761 (2013).

22. Huang X, Yeo W-H, Liu Y, Rogers JA. Epidermal Differential Impedance Sensor for Conformal Skin Hydration Monitoring. *Biointerphases* **7**, 52 (2012).

23. Huang X, *et al.* Epidermal Impedance Sensing Sheets for Precision Hydration Assessment and Spatial Mapping. *Biomedical Engineering, IEEE Transactions on* **60**, 2848-2857 (2013).

24. Xu S, *et al.* Stretchable batteries with self-similar serpentine interconnects and integrated wireless recharging systems. *Nat Commun* **4**, 1543 (2013).

25. Harb A. Energy harvesting: State-of-the-art. *Renewable Energy* **36**, 2641-2654 (2011).

26. Paradiso JA, Starner T. Energy scavenging for mobile and wireless electronics. *Pervasive Computing, IEEE* **4**, 18-27 (2005).

27. Mitcheson PD, Yeatman EM, Rao GK, Holmes AS, Green TC. Energy Harvesting From

Human and Machine Motion for Wireless Electronic Devices. *Proc IEEE* **96**, 1457-1486 (2008).

28. Priya S, Inman DJ. *Energy harvesting technologies*. Springer (2009).

29. Hudak NS, Amatucci GG. Small-scale energy harvesting through thermoelectric, vibration, and radiofrequency power conversion. *J Appl Phys* **103**, (2008).

30. Kim J, *et al.* Miniaturized Flexible Electronic Systems with Wireless Power and Near-Field Communication Capabilities. *Adv Funct Mater* **25**, 4761-4767 (2015).

31. Kurs A, Karalis A, Moffatt R, Joannopoulos JD, Fisher P, Solja?i M. Wireless Power Transfer via Strongly Coupled Magnetic Resonances. *Science* **317**, 83-86 (2007).

32. Ho JS, *et al.* Wireless power transfer to deep-tissue microimplants. *Proceedings of the National Academy of Sciences* **111**, 7974-7979 (2014).

33. Le T, Mayaram K, Fiez T. Efficient Far-Field Radio Frequency Energy Harvesting for Passively Powered Sensor Networks. *Solid-State Circuits, IEEE Journal of* **43**, 1287-1302 (2008).

34. Sung Il P, *et al.* Ultraminiaturized photovoltaic and radio frequency powered optoelectronic systems for wireless optogenetics. *Journal of Neural Engineering* **12**, 056002 (2015).

35. Jabbar H, Song YS, Jeong TT. RF energy harvesting system and circuits for charging of mobile devices. *Consumer Electronics, IEEE Transactions on* **56**, 247-253 (2010).

36. Nishimoto H, Kawahara Y, Asami T. Prototype implementation of ambient RF energy harvesting wireless sensor networks. In: *Sensors, 2010 IEEE* (ed^(eds) (2010).

37. Pinuela M, Mitcheson PD, Lucyszyn S. Ambient RF Energy Harvesting in Urban and Semi-Urban Environments. *Microwave Theory and Techniques, IEEE Transactions on* **61**, 2715-2726 (2013).

38. Loo Y-L, *et al.* Soft, conformable electrical contacts for organic semiconductors: High-resolution plastic circuits by lamination. *Proceedings of the National Academy of Sciences* **99**, 10252-10256 (2002).

39. Jacobs HO, Whitesides GM. Submicrometer Patterning of Charge in Thin-Film Electrets. *Science* **291**, 1763-1766 (2001).

40. Zaumseil J, Baldwin KW, Rogers JA. Contact resistance in organic transistors that use source and drain electrodes formed by soft contact lamination. *J Appl Phys* **93**, 6117-6124 (2003).

41. Wang S, *et al.* Mechanics of Epidermal Electronics. *Journal of Applied Mechanics* **79**, 031022-031022 (2012).

42. Webb RC, *et al.* Ultrathin conformal devices for precise and continuous thermal characterization of human skin. *Nat Mater* **12**, 938-944 (2013).

43. Agilent.Technologies. Advanced Design System, Nonlinear devices. (2008).

44. Std FCC. Supplement C. *OET Bulletin* **65**, 97-01.

45. Simulia D. Abaqus Analysis-User's Manual V6. 10. *vol III*, (2010).

46. Ahn S, Oh TI, Jun SC, Seo JK, Woo EJ. Validation of weighted frequency-difference EIT using a three-dimensional hemisphere model and phantom. *Physiol Meas* **32**, 1663 (2011).

47. Powers RA. Batteries for low power electronics. *Proc IEEE* **83**, 687-693 (1995).

48. Kim JB, *et al.* Reversible Soft-Contact Lamination and Delamination for Non-Invasive Fabrication and Characterization of Bulk-Heterojunction and Bilayer Organic Solar Cells. *Chem Mater* **22**, 4931-4938 (2010).

49. Lee S, *et al.* LEGO-like assembly of peelable, deformable components for integrated devices. *NPG Asia Mater* **5**, e66 (2013).

50. Huang J, Li G, Yang Y. A Semi-transparent Plastic Solar Cell Fabricated by a Lamination Process. *Adv Mater* **20**, 415-419 (2008).

51. Hu L, Wu H, La Mantia F, Yang Y, Cui Y. Thin, Flexible Secondary Li-Ion Paper Batteries. *ACS Nano* **4**, 5843-5848 (2010).

52. Granstrom M, Petritsch K, Arias AC, Lux A, Andersson MR, Friend RH. Laminated fabrication of polymeric photovoltaic diodes. *Nature* **395**, 257-260 (1998).

53. Chabinyc ML, *et al.* Lamination Method for the Study of Interfaces in Polymeric Thin Film Transistors. *J Am Chem Soc* **126**, 13928-13929 (2004).

54. Ferguson G, Sigal G, Whitesides G, Chaudhury M. Contact adhesion of thin gold films on elastomeric supports- Cold welding under ambient conditions. *Science* **253**, 776-778 (1991).

55. Lu Y, Huang JY, Wang C, Sun S, Lou J. Cold welding of ultrathin gold nanowires. *Nature nanotechnology* **5**, 218-224 (2010).

56. Liu C, Li Y-J, Sun S-G, Yeung ES. Room-temperature cold-welding of gold nanoparticles for enhancing the electrooxidation of carbon monoxide. *Chemical Communications* **47**, 4481-4483 (2011).

57. Carlson A, Bowen AM, Huang Y, Nuzzo RG, Rogers JA. Transfer Printing Techniques for Materials Assembly and Micro/Nanodevice Fabrication. *Advanced Materials* **24**, 5284-5318 (2012).

58. Kim C, Burrows PE, Forrest SR. Micropatterning of Organic Electronic Devices by Cold-Welding. *Science* **288**, 831-833 (2000).

59. Pereira ZS, da Silva EZ. Cold Welding of Gold and Silver Nanowires: A Molecular Dynamics Study. *The Journal of Physical Chemistry C* **115**, 22870-22876 (2011).

60. Akande WO, Cao Y, Yao N, Soboyejo W. Adhesion and the cold welding of gold-silver thin films. *Journal of Applied Physics* **107**, - (2010).

## 5.13 Figures

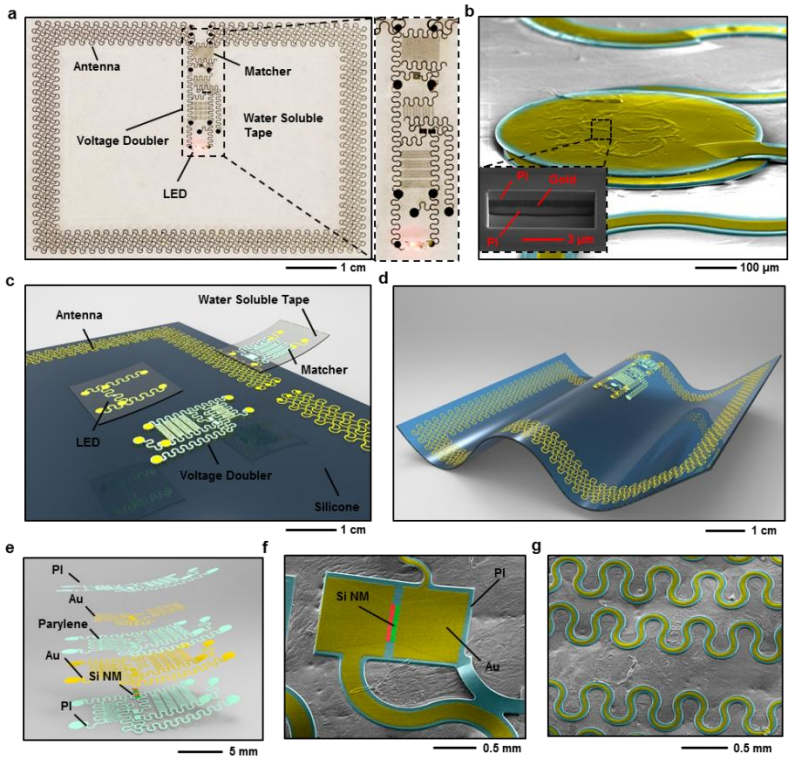


**Figure 5.1 Schematic illustration and implementation of a modularized epidermal RF system for wireless power transfer.** (a) Image of device while operating an integrated LED via power delivered by a remote RF source (15 W, 1.5 m). The loop antenna, formed with serpentine conductive traces in a square layout, spans the perimeter. The inset on the right highlights the collection of active components. (b) Top view SEM image of aligned gold pads whose electrical contact joins separate, laminated components. The inset provides a cross sectional view of the interface. (c) Diagram that illustrates the modularization approach to device assembly, where sequential lamination of separately fabricated, thin film components yields an integrated, functional system (d) Diagram of a completed system on a thin silicone substrate. (e) Exploded view illustration of a voltage doubler. (f) Colorized SEM image of a silicon nanomembrane (SiNM) RF diode, integrated as part of a voltage doubler resting on a skin replica. (g) Colored SEM image of parallel plate capacitors in serpentine geometries on a skin replica.

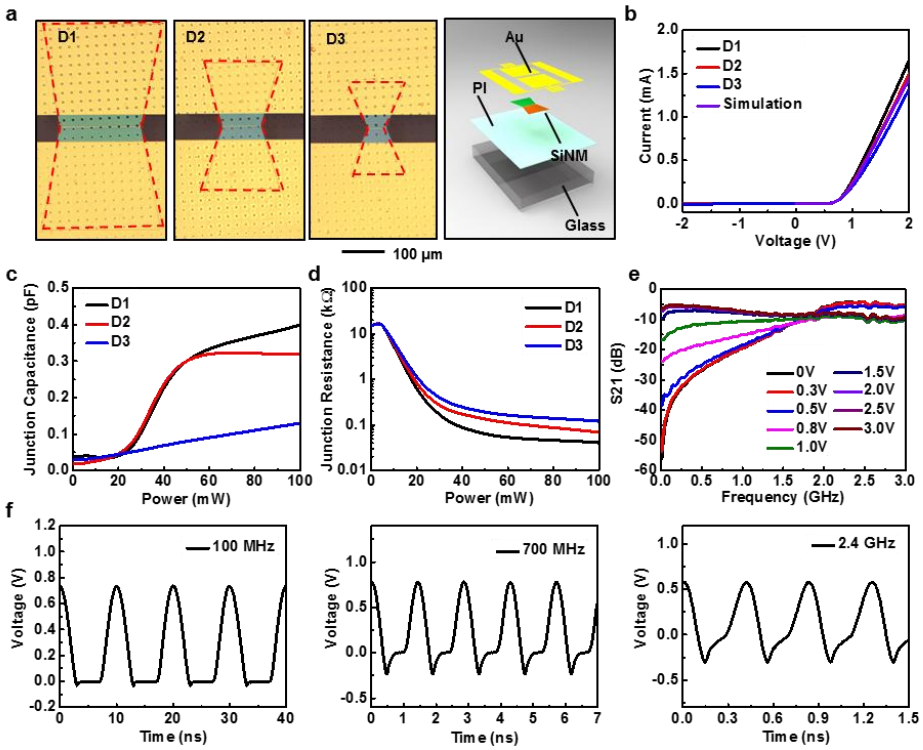


**Figure 5.2 Electrical characterization of SiNM PIN diodes.** (a) Optical images of PIN diodes that use SiNMs in wedge shapes with different geometries (D1, D2, D3). The frame on the left provides a schematic exploded view illustration. (b) Experimentally measured and simulated current-voltage curves associated with the diodes. The (c) junction capacitance, (d) junction resistance and (e) S21 parameters of the diodes. (f) Rectified voltages from the diodes at frequencies of 100 MHz (left), 700 MHz (middle) and 2.4 GHz (right).

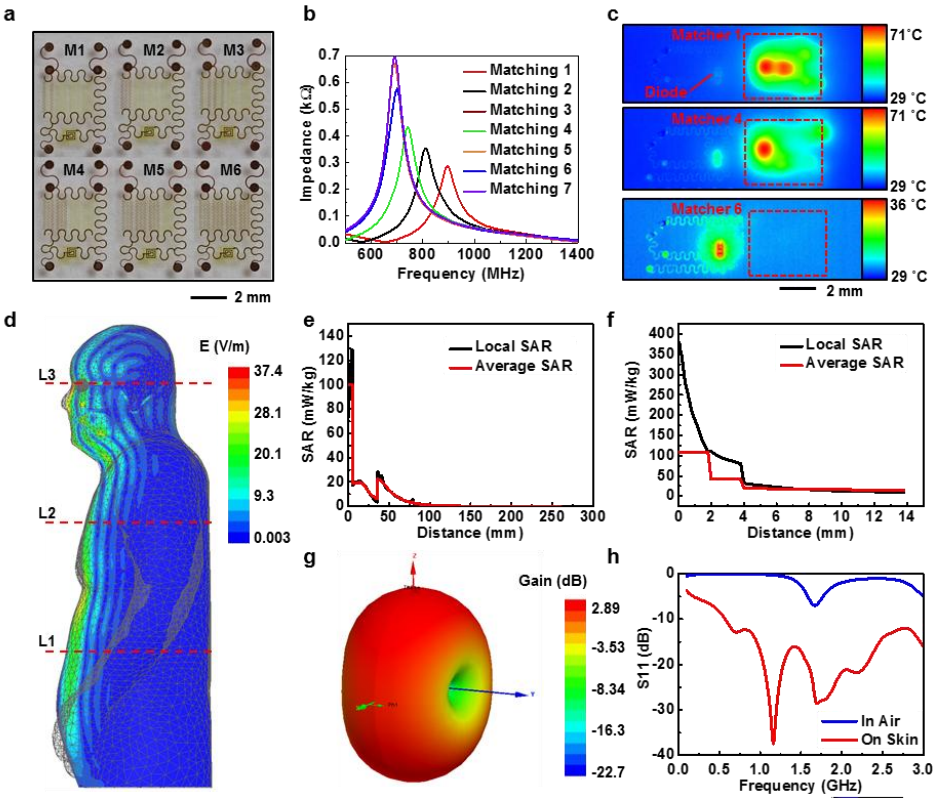


**Figure 5.3 RF properties of modularized system components and results of SAR simulations.** (a) Images of matching components with different capacitors, labeled from 1 to 6. (b) Resonance frequencies of these matching components. (c) Thermal analysis of the performance of matching components (1, 4 and 6; red dashed boxes) during RF operation in a voltage doubler. Low coupling efficiency manifests as high temperature during operation. (d) Simulated SAR across a model human body for the case of an RF source (Gain: 11 dBi, 15 W, 1 GHz) 1.5 m away from the human body. (e) Simulated SAR in the human body at L2. Average SAR is an average of local SAR over 1 g of tissue. . (f) Simulated SAR in the skin area underneath an epidermal RF power transfer system with loop antenna mounted at L2. (g) Simulated radiation pattern of a loop antenna in air. (h) Simulated S11 parameter of a loop antenna evaluated in air and on skin.

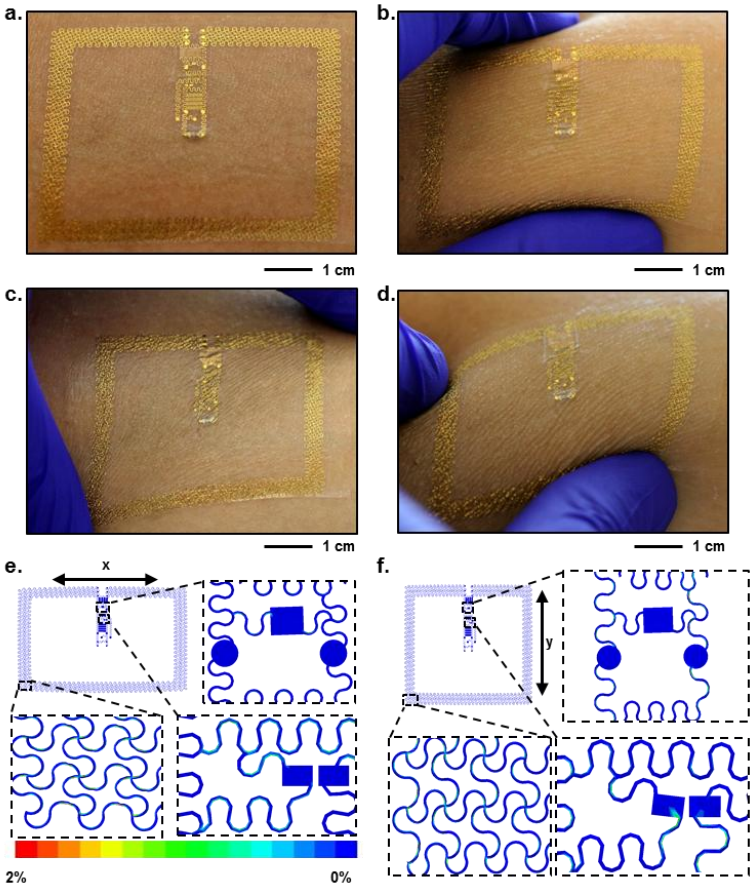


**Figure 5.4 Mechanics of an epidermal RF system.** Pictures of an epidermal RF system integrated on the skin (a) in its native state, (b) during compression by pinching (c) under uniaxial stretch, and (d) while twisted. Finite element simulation of the distributions of strain under 20% uniaxial stretching in the (e) x and (f) y directions.

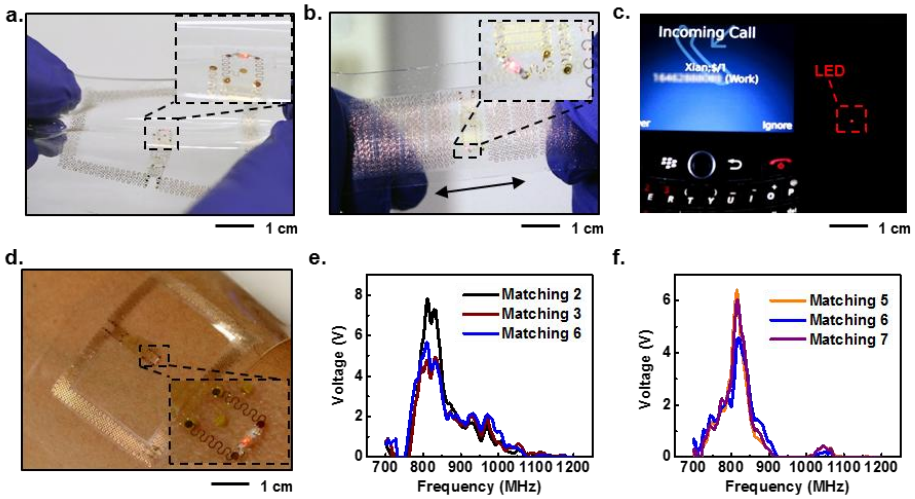


**Figure 5.5 Demonstration of RF wireless power transfer.** Epidermal RF system operating while (a) twisted and (b) repeatedly stretched. (c) Demonstration of the use epidermal RF system to capture RF output from a cell phone to supply power to an LED. (d) Epidermal RF system powering a red LED while on the skin from RF transmitted by a remote RF source (15 W, 1.5 m, 700 MHz – 1.5 GHz). Open circuit voltage output (e) in air and (f) on skin when implemented with different matching components.

# CHAPTER 6

# CUTANEOUS MULTI-FUNCTIONAL WEARABLE PLATFORM FOR CLINICAL MONITORINGS

## 6.1 Introduction

Peripheral nerve disorders are a common source of disability[1]. The electrophysiology diagnostic tests such as needle electromyography (EMG) are conducted to evaluate patients with these disorders. This kind of invasive EMG studies can be uncomfortable for the patient despite the neurophysiologist's best efforts due to sharp needle penetration into skin tissue[2]. Soft, self-adhesive electrodes that can measure surface EMG signal from the skin are a convenient solution; however, the hydrogel adhesive commonly found in these electrodes degrades as their water content evaporates over the course of hours[3]. Also, the extended and sometimes tangled wires from multiple monitoring sites create complexity and limited space for surgeons to operate[4]. Moreover, during surgery, peripheral nerves are often damaged which can leave patients with significant pain and disability[1]. Intraoperative methods of monitoring nerves are available but currently require both trained personnel and expensive equipment[5]. An ideal clinical monitoring tool should provide 1) thin, soft, conformal interface with the skin surface, 2) wireless communication and powering capabilities, 3) integrated long-lasting electrodes with electronic packages, and 4) simple operation interface with minimal preparation steps before the surgery.

Recent advances[6, 7] in wearable technology and the emerging class of epidermal electronic system (EES) has made it possible to create flexible, skin-mounted electronic patches that contain high-performance integrated chips, wireless functionalities, long-lasting Ag/AgCl electrodes, an user-friendly software interface to monitor muscle electrical activity at a remote distance. We have used such a device, called the BioStamp Research Connect™ (MC10 Inc.), to

monitor nerve-muscle function during peripheral nerve, spine, and cranial surgery and compared its performance to standard needle EMG techniques.

In this study, patients diagnosed with peripheral nerve disorder and scheduled to undergo needle EMG at Northwestern Memorial Hospital will have skin patch sensors placed over several individual muscles that will also be monitored using needle EMG techniques per standard of care. Recordings taken from the skin patch sensors and needle electrodes in muscles will then be compared to determine the performance characteristics of the skin patches relative to the current gold standard of needle EMG recordings. We hypothesize that skin patch sensors have comparable sensitivity, specificity, and reliability in detecting muscle movement to direct nerve stimulation as do EMG needle recordings.

## 6.2 Biostamp Research Connect

Epidermal electronic system (EES) is currently limited to electrophysiology electrodes and platforms with simple circuit design due to the complexity of fabricating thin-film, high-performing integrated circuits[6]. This limitation hinges the commercial development and widespread of a practical products. Inspired by the hard-soft integration techniques published by Xu *et al.* in Science (2014) that integrates commercial-off-the-shelve chips on stretchable copper interconnects[7], MC10 develop a commercial-grade medical electronic device that is soft, flexible, and wearable[8, 9] (figure 6.1). It features state-of-the-art body-worn sensors that can be placed on numerous body locations for targeted data collection (figure 6.1e), a wireless platform with online portal to view and download data (figure 6.1b), and light-weight, small form factor[8]. The Biostamp RC has a thin layer of integrated chip sets encapsulated by silicone rubber, the circuit includes a small lithium polymer rechargeable battery at 15 mAh, wireless recharging component at 13.56 MHz, bluetooth module, 32 MB flash memory, 3-axis accelerometer and gyroscope, and

analog-front end connected to 3 Ag/AgCl electrodes[9]. The battery can be recharged wireless in less than two hours. The memory can support 2-16 hours of continuous monitoring. The accelerometer has adjustable sampling rate, sensitivity and resolution, but the optimal condition is set at 50 Hz, ± 4g, and 10 mg. For gyroscope, the optimal setting is 100 Hz, ± 2000 ◦/s, and 0.2 ◦/s. Before applying the sensor patch to skin, either non-sterilize or sterilize conductive gel could be apply to the electrode surface to decrease skin-electrode interface impedance and improve signal-to-noise ratio (figure 6.1c). Disposable adhesives are used to couple the sensor patch to skin, one side of the adhesive goes to the bottom of Biostamp, the other side, after peeling the backing layer, can be mounted on any body locations (figure 6.1d). After usage, the adhesive textile can be disposed and Biostamp could be reused after cleaning with alcohol wipes or disinfecting agents.

## 6.3 Peripheral Nerve Surgery Monitoring

The clinical study is conducted at Northwestern Memorial Hospital with Dr. Michel Kliot, Mathew Cotton, Dr. Nader Dahdaleh, and Dr. Tyler Koski. Potential subjects will initially present in the outpatient clinical practice of the principal investigator (PI). The PI will discuss the study with potential subjects and answer any questions they have about participation. With proper consent, the study will happen during the surgery with researcher presented. The Biostamp skin patch sensors will be placed prior to the patient's surgery and be worn by the patient for the duration of his/her surgery. Once the surgery is complete, the skin patches will be removed. For peripheral nerve monitoring, the operated nerve is usually the sciatic mean nerve on the lower leg, which innervates gastrocnemius muscle. The EMG electrodes will be placed on the gastrocnemius muscle to detect stimulation-evoked potential from the sciatic nerve (figure 6.2a).

During surgery, the surgeon will open the body tissue until the operated nerve is exposed; a decompression was usually done, with exceptions of some other more complicated procedures like tumor dissection or nerve grafting. The study is performed before the actual surgery takes place, with duration of 10-15 minutes. The surgeon will bring the stimulation electrode close to the nerve, and the researcher will record the EMG spectral and the stimulation threshold. Figure 6.2b shows a picture of the experimental setup. Figures 6.2c and 6.2d shows the monitoring interface of commercial clinical software Cadwell Cascade and the Biostamp results, the EMG signal shown is collected from one stimulation pulse.

## 6.4 Comparison of Electromyogram Electrodes

Three types of EMG electrodes were placed on one subject patient for the comparison of EMG sensing functionality (figure 6.2a). Needle type metal electrode made of stainless steel is the golden standard for the medical community, and is the most widely used monitoring electrodes during surgery[10]. Surface hydrogel electrode is usually disposable and low cost, made of electrically conductive hydrogel adhesive that provides conformal contact with skin. Biostamp uses bare Ag/AgCl electrodes with additional conductive gel and textile adhesive to improve the skin-electrode contact. These electrodes are placed close to each other on both anode and cathode location for optimal comparison. The stimulation pulse used in this study is monophasic waveform at 2.6 Hz, 200 us pulse width, and adjustable current levels. Figures 6.3a to 6.3c show the measured EMG spectral with stimulation current from 1.3 to 1.7 mA. EMG spectral intensity increases with stimulation current density as expected, but only surface hydrogel electrode shows distinguish gradual increase, while the other two electrodes show a sudden jump from 1.4 mA to 1.5 mA. The signal duration differences are due to sampling rate variation. EMG signal appears at 1.4 mA in Biostamp, but 1.3mA in the other two types of electrodes, indicating a lower

threshold current.

As a baseline measurement, the stimulation needle was placed on three locations to test the EMG response of Biostamp electrode. During nerve stimulation at 1 mA, a clear EMG response can be captured, while no EMG signal can be seen during tissue and no stimulation condition.

## 6.5 Stimulation Current Threshold

Stimulation current threshold provides vital information to investigate the physiological status of the patient's nerve, the stimulation technique also serves as a monitoring tool for surgeon to distinguish between actual nervous tissues, and other surrounding tissues. If the stimulation current threshold between Biostamp and commercial system is the same, it has the potential to replace the commercial system. During current stimulation, the electrode depolarizes the nerve cell membrane, causing exchanges in intracellular and extracellular sodium and potassium ions[11]. The impulse is then propagated along the nerve to its innervated muscle and induces motor response; the evoked muscle potential is then captured by the electrodes penetrating through the muscle fiber or placed on the surface.

The results collected from 5 patients (figure 6.4a) show that stimulation current threshold varied by patients, by nerve location, and by tissue impedance, therefore only the comparisons between electrodes are meaningful. Biostamp shows higher current threshold than needle electrodes on abnormal nerves with slower nerve conduction velocity, otherwise, the values are similar to each other, with Biostamp having a slightly higher current threshold than needle electrodes. Figure 6.4b shows the comparison of three types of electrodes, with a trend of higher current threshold from Biostamp to needle to surface electrode. The data also shows statistically significant differences to 0.05 mA ($P < 0.05$) between Biostamp and two other electrodes

## 6.6 Conclusions

Biostamp offers surgeons an easy, reliable and cost-effective way to monitor, protect, and preserve nerve function during surgery. Clinical study shows that Biostamp can distinguish stimulation on nerve and surrounding tissues, indicating no severe stimulation artifacts. The stimulation current threshold of Biostamp is very similar to both needle type metal electrode and surface hydrogel electrode, showing its comparable capabilities to be used as a clinical monitoring tool. It is hoped that using this device will allow surgeons to improve patient outcome when performing operations where nerves are at risk of being injured.

## 6.7 References


1. Dyck PJ. *Peripheral neuropathy*. Elsevier Inc. (2005).

2. Jankovic J. Needle EMG guidance is rarely required. *Muscle & nerve* **24**, 1568-1570 (2001).

3. Plessis Jd, Stefaniak A, Eloff F, *et al.* International guidelines for the in vivo assessment of skin properties in non-clinical settings: Part 2. transepidermal water loss and skin hydration. *Skin Research and Technology* **19**, 265-278 (2013).

4. Cypher D, Chevrollier N, Montavont N, *et al.* Prevailing over wires in healthcare environments: benefits and challenges. *IEEE Communications Magazine* **44**, 56-63 (2006).

5. Hermann M, Hellebart C, Freissmuth M. Neuromonitoring in thyroid surgery: prospective evaluation of intraoperative electrophysiological responses for the prediction of recurrent laryngeal nerve injury. *Annals of surgery* **240**, 9-17 (2004).

6. Kim D-H, Lu N, Ma R, *et al.* Epidermal electronics. *science* **333**, 838-843 (2011).

7. Xu S, Zhang Y, Jia L, *et al.* Soft microfluidic assemblies of sensors, circuits, and radios for the skin. *science* **344**, 70-74 (2014).

8. MC10. Biostamp RC Overview. (2016).

9. MC10. Biostamp User Manual. (2016).

10. Merletti R, Knaflitz M, De Luca CJ. Electrically evoked myoelectric signals. *Crit Rev*

*Biomed Eng* **19**, 293-340 (1992).

11. Keyl C, Held T, Albiez G, *et al.* Increased electrical nerve stimulation threshold of the sciatic nerve in patients with diabetic foot gangrene: a prospective parallel cohort study. *European Journal of Anaesthesiology (EJA)* **30**, 435-440 (2013).

## 6.8 Figures

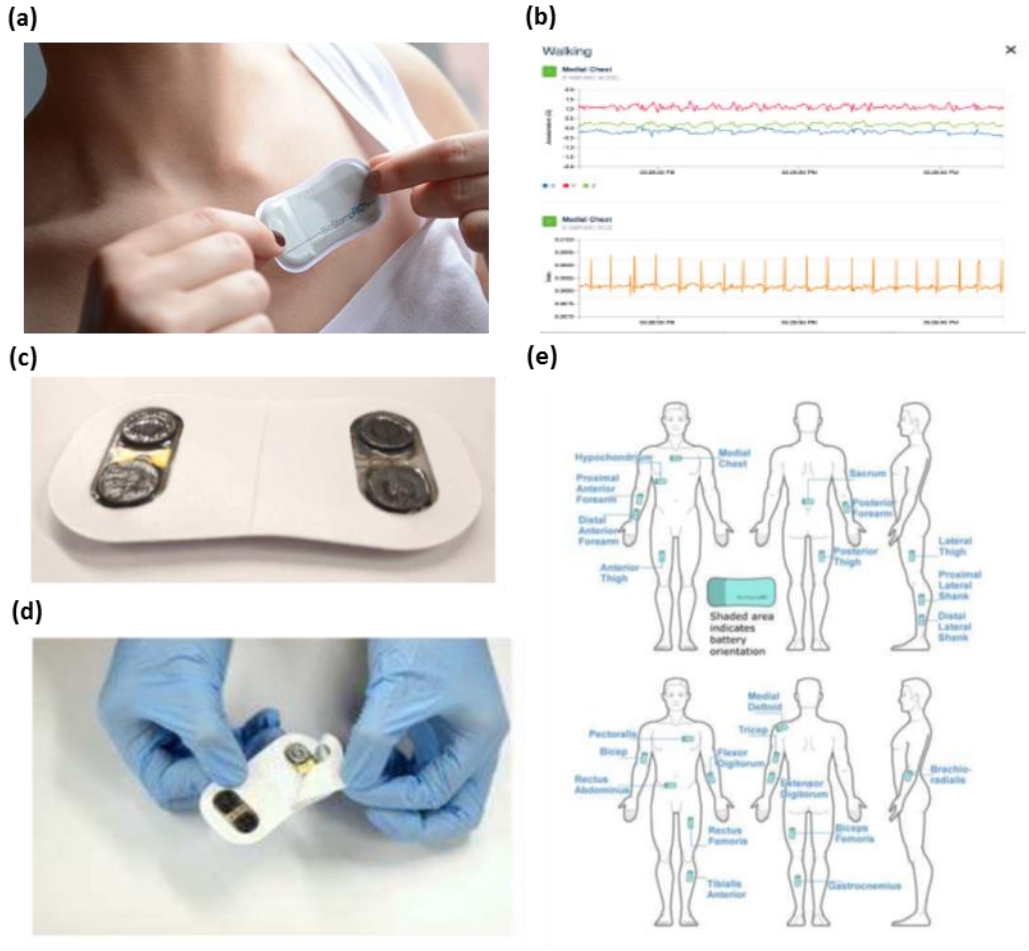


**Figure 6.1 Biostamp Research Connect Product Overview.** (a) Demonstration of wearability of Biostamp on skin. (b) User-friendly software interface with real-time monitoring. (c) Back side of Biostamp with electrodes after applying conductive gel. (d) The process of peeling off adhesive back for skin mounting preparation. (e) Examples of body mounting locations for Biostamp. Reproduced from references 8, 9.

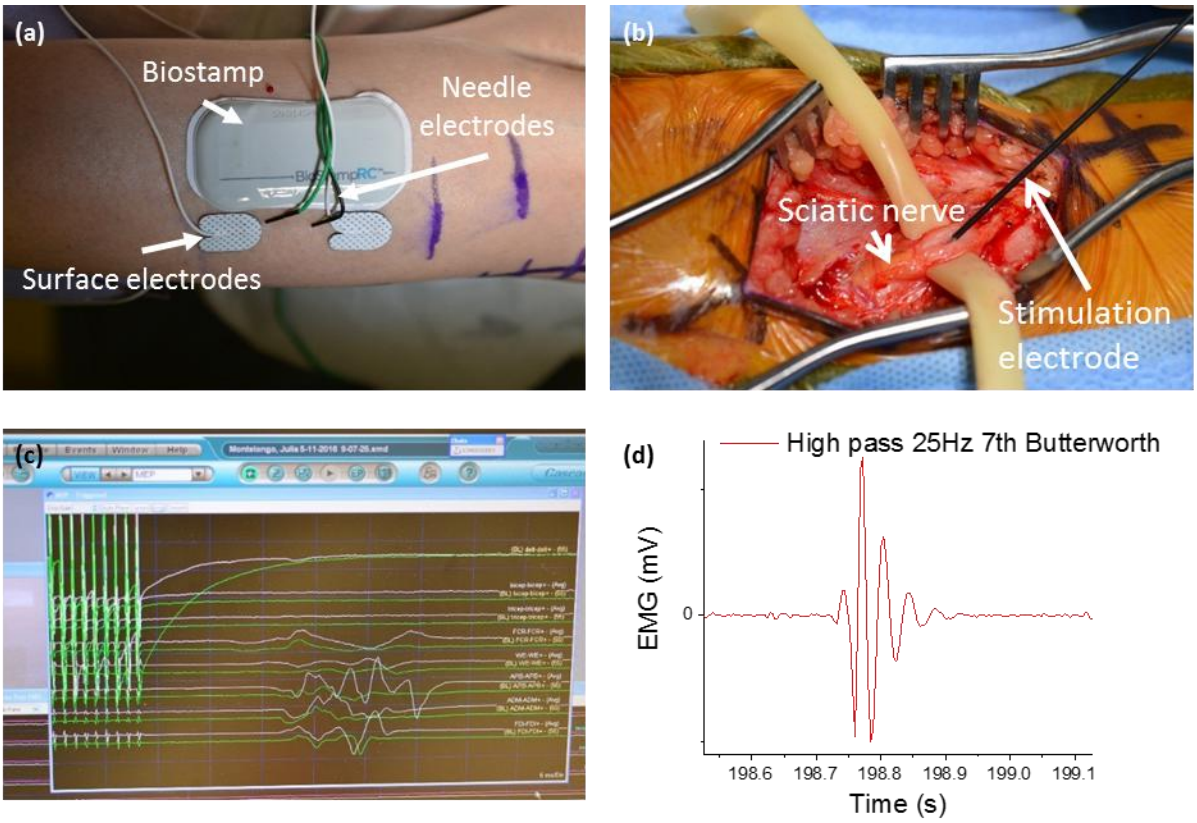


**Figure 6.2 Peripheral Nerve Surgery Monitoring.** (a) Application of three types of EMG electrodes. (b) Clinical study setup during Sciatic nerve decompression surgery. (c) Monitoring interface of commercial clinical monitoring software, Cadwell Cascade. (d) Example of a stimulation-evoked EMG signal collected by Biostamp after digital filtering.

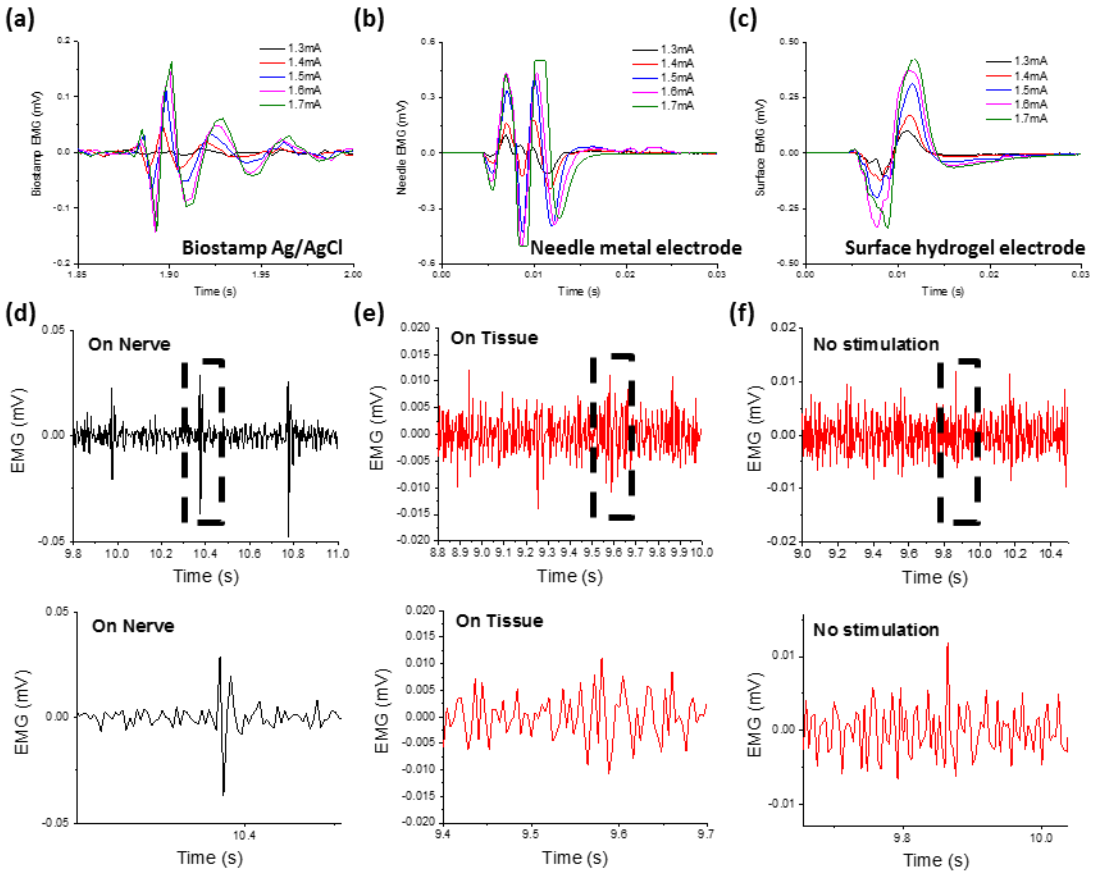


**Figure 6.3 Comparative study of electromyogram electrodes.** EMG measurement at various evoke stimulation current using (a) Biostamp, (b) Needle metal electrodes, and (c) surface hydrogel electrodes. Clinical EMG measurement on Biostamp when the stimulation electrode is placed on (d) nerve, (e) tissue, and (f) with no stimulation.

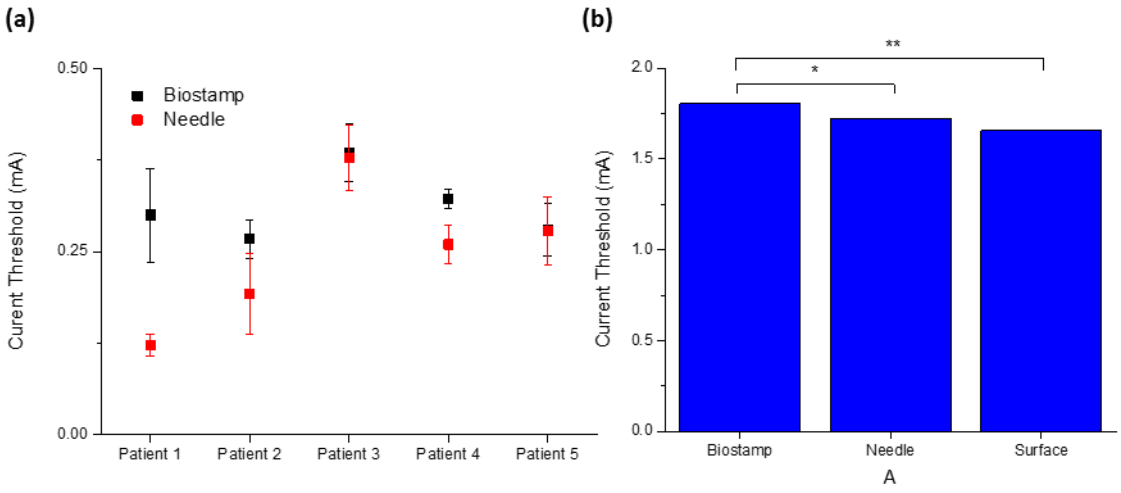


**Figure 6.4 Stimulation Current Threshold Study.** (a) Mean values of stimulation current threshold of 5 different patients. (b) Statistical significance test of mean threshold current recorded using three types of electrodes.

# CHAPTER 7

# CONCLUSIONS AND OUTLOOK

## 7.1 Summary

As mentioned throughout the dissertation, I believe that the future of electronics should be flexible, stretchable, and wearable. In my doctoral research, I am very fortunate to work on the development of epidermal electronic system (EES), including the differential impedance hydration sensor, 2-dimensional hydration mapping arrays, wireless hydration system, sweat sensor with wireless and colorimetric capabilities, capacitive electrophysiology sensing, multi-functional electrophysiology and stimulation platform, mechano-acoustic sensing platform, radio-frequency power transfer modules, and Biostamp research connect system. In addition to these EES, I have also worked on *in-vivo* Electrocorticogram neural sensor; physically transient, biodegradable printed circuit board that could dissolve in water or biofluids; animal studies using implantable 3-dimensional multi-functional cardiac sensing and stimulation system; assembly of micro/nanomaterials into complex, 3-dimensional architectures by compress buckling to probe the extreme of mechanics on single-crystalline materials; and wireless optogenetic system for *in-vivo* drug delivery. I have developed new sensors and sensing mechanisms via novel materials strategies and circuit design; I have processed bio-signals for human-machine interface control and feedback on robotics and prosthesis; I have designed and conducted animal and clinical studies to validate the EESs. All of the aforementioned work allows me to complete my doctoral study while experiencing the full cycle from fundamental science studies to research development to commercialization and product validation.

## 7.2 Future of Skin-mounted Electronics

The future direction of skin-mounted, body-worn, epidermal electronics should focus on

either the development of disposable, low-cost epidermal electronic tattoo or reusable, flexible patch with complex functionalities. For the former direction, a simple electronic tattoo with near-field communication (NFC) antenna and unpackaged microcontroller integrated chips could provide simple operation modes for healthcare monitoring. Wirings and cables in the research-level prototypes need to be eliminated for practical applications. Bluetooth technologies consume too much power, and there are no thin-film batteries with high enough energy density to sustain the wireless operation on such epidermal devices. RF technologies are not feasible to skin tattoos due to complicated dielectric environments at the skin-device interface. For the latter direction, it is more practical for commercialization, but a complete engineering solution is needed for the following areas: 1) Develop a high-performance, stable wireless solution with long-lasting operation time, remote powering, and real-time monitoring, 2) Develop thin-film batteries with high energy density or methods for recharging at a remote distance, 3) Develop efficient integrated circuits and encapsulation schemes for ultrathin form factor and flexibility, 4) Develop and characterize novel materials for extremely low modulus or impedance materials for skin applications. In either case, the fundamental science between the skin-device interfaces requires more systematic studies. Possible topics include the skin-electrode impedance, adhesion mechanism, electromagnetic skin effect, and materials biocompatibility. Overall, the works reported here represent a promising launch and proof-of-concept prototypes for the future development of wearable, flexible, and stretchable electronics.